Transport of Aqueous and Organic Fluids through Micro- and Nanoporous Media

by

Md Minhajul Islam

A thesis submitted in partial fulfillment of the requirements for the degree of

Doctor of Philosophy

Department of Chemistry
University of Alberta

Abstract

In predicting oil and gas recovery, researchers develop models primarily focusing on macro- or milli-scale flows by applying Navier-Stokes types solutions and no-slip boundary conditions. They compare or cross-check their models to known experimental results available in the literature for larger pore scales. In contrast, much less experimental data is available to use in modelling nanoscale flows, which is very important in oil and gas recovery applications. Moreover, porous media flow in smaller scales is also important in other fields of science, for example, in chromatography (with smaller packing particles), nanofluidic diode, fuel cells and other devices. Few theoretical and experimental studies are found in the literature on fluid flow in nanofluidic structures. However, a wide range of flow enhancement results with up to several orders of magnitude discrepancies is present between theoretical and experimental works. Therefore, realizing the need for more experimental data in the case of smaller-scale flows, we focused on studying the flow behaviour of aqueous and organic viscous liquids through silica-based micro and nanoporous structures with the fundamental concern of whether the no-slip boundary condition, a macroscale assumption, can correctly describe the micro and nanoscale flow properties for various combinations of fluid-solid surface interaction. The effect of pore sizes in porous media and the surface interaction between a viscous liquid and porous bed material on micro- and nanofluidic flow phenomena is reported here. We develop micro and nanoporous media by packing nonporous silica microspheres (300-2000 nm particle diameter) inside fused silica microcapillary tubes. The interconnected pores among the silica particles form the micro- or nanofluidic channels for fluid flow. A time-of-flight, photobleaching velocity

measurement technique is employed to determine the linear flow velocity of a viscous liquid flowing through a porous media. Throughout the applied pressure range (100-6000 psi), the Newtonian fluids, irrespective of their wetting property, exhibit a laminar flow pattern (R_e <<1), which validates the applicability of porous media flow equations (Darcy and Kozeny-Carman equations) for our porous systems (39.5 to 340 nm pore radius). The pressure-driven flow experiments for a non-wetting liquid (n-octane) through silica micro- or nano-porous media confirm the existence of slip flow. The more viscous 1-octanol, which has both wetting (polar hydroxyl group) and non-wetting (non-polar octyl group) parts in its structure, also experiences slip flow in the silica micro- and nanoporous beds. However, the extent of slip flow with 1-octanol is less pronounced than n-octane, though both molecules have the same length of hydrophobic alkyl chain in their structures. For both liquids, the flow enhancement is more noticeable in the nanoporous beds than the microporous ones. Slip length increases with the decreasing pore diameter of the porous media. The silica porous bed with the smallest pore radius gives the maximum flow rate enhancement, where the slip lengths for the n-octane and 1-octanol are 18.1 ± 1.0 and 7.4 ± 0.3 nm, respectively. This research fills a large gap in the literature involved for the flow of organic fluids through hydrophilic nanoporous media, and it will be useful for the future refinement of theoretical models of micro and nanoscale porous media flow.

Preface

This thesis presents the original work done by Md Minhajul Islam, who was responsible for all works (e.g., literature search, instrumentation, preparation of columns and solutions, data collection and analysis, and manuscript composition) presented in this thesis. Parts of Chapter 2, 3 and 4 of this thesis have been published as "Slip and No-Slip Flow in Micro-and Nano-Porous Media", Md Minhajul Islam and D. Jed Harrison, Bulletin of the American Physical Society (2018, Volume 63), 71st Annual Meeting of the APS Division of Fluid Dynamics (APS-DFD 2018); November 18–20, Atlanta, USA. In addition, parts of Chapter 2, 3 and 5 of this thesis have been published as "Effect of Pore Size on Slip Flow in Micro- and Nano-Porous Media", Md Minhajul Islam and D. Jed Harrison, 23rd International Conference on Miniaturized Systems for Chemistry and Life Sciences (MicroTAS 2019); October 27-31, Basel, Switzerland; pages 1032-1033. Furthermore, parts of Chapter 2, 3 and 6 of this thesis have been published as "Transport of Viscous Fluid through Micro- and Nano-Porous Media", Md Minhajul Islam and D. Jed Harrison, 24th International Conference on Miniaturized Systems for Chemistry and Life Sciences (MicroTAS 2020); October 4-9, Online; pages 200-201. Professor D. Jed Harrison was the supervisory investigator involved with research problem establishment, instrument design ideas and manuscript composition.

Acknowledgements

First and foremost, I would like to express my sincere gratitude to my supervisor Professor D. Jed Harrison, for his guidance and continuous support throughout my PhD journey. He gave me the opportunity to grow as an independent researcher. The training I received from him helped boost my confidence that I would be able to solve any new problem in a systematic and logical process, even though I was not familiar with it beforehand. Furthermore, he continuously provided me with enormous mental support to cope in the new culture and environment and manage the academic stress. It would not be possible for me to finish this thesis without his invaluable suggestions, patience and support. I sincerely thank him for providing me with a rich and rewarding academic experience.

Besides my supervisor, I am also grateful to my supervisory committee members, Professor Jillian M. Buriak and Professor Mark T. McDermott, for their valuable suggestions during my research. I would like to thank Professor Yunjie Xu and Professor Steven H. Bergens for attending my candidacy exam and providing valuable suggestions. Special thanks to Dirk Kelm and Deiter from the Machine shop; Kim and Andrew from the Electronic shop for helping me to build my instrumental setup; Dave Fortin from the Physics department for writing the Labview program for me; other support staffs from the Chemistry department, without which my doctoral research would not have been completed smoothly. I am grateful to my group members, Dr. Mohammad Alaul Azim, Dr. Narges Shabani, Dr. Hamid Ramezani, Dr. Yufeng

Zhao, Dr. Jing Ji, Dr. Yuting Hou, Nisat Zahan and Rambukkana Maggonage Sureka Perera, for their supports.

Special thanks to my friends Dr. Md Amran Howlader, Farzana Yasmin, Mahmud Reshedul Amin, Sharifunnesa Chowdhuri, Nafis Razzak, Mahzabin Akhand and many more that I have met over the years who supported my family and me in difficult times and made my life colorful and enjoyable here.

I am out of words to fully express my gratefulness and appreciation to my parents, my elder brother and sister, and other family members for their love and support throughout my life. Finally, I want to express my special thanks and gratitude to my beloved wife, Nisat Zahan, for her unconditional love and support. Not only as a wife, but she was also always with me in this journey as a labmate, classmate, TA colleague too. Lastly, special thanks to my beloved son, Niham Mustahsan Islam, whose innocent smile relieved my stresses during this thesis writing.

Table of Contents

List of Tables

List of Figures

List of Symbols

A	Cross-sectional area
C	Mass transfer term in the van Deemter equation
C4	Butyl side chain
C_{ave}	Cross-sectional average of dye solution concentration
C_o	Original dye concentration
D	Hydrodynamic diameter of column
$D_{diffusion}$	Molecular diffusion coefficient
D_{eff}	Effective diffusion coefficient
$d_{particle}$	Diameter of the particle
d_{pore}	Pore diameter
E	Flow enhancement factor
ΔE	Standard deviation in flow enhancement factor
E_L	Entrance length
g_x, g_y and g_z	Acceleration of gravity vectors in the x, y and z directions, respectively
h	Dye plug width
I_{max}	Maximum fluorescence signal intensity
I_{min}	Minimum fluorescence signal intensity
I_{peak}	Fluorescence signal intensity at the peak of the highest derivative
k	Permeability
L	Length

L_e	Effective travel distance
L_s	Slip length
ΔL_s	Standard deviation in slip length
P	Pressure
P_e	Peclet number
ΔP	Applied pressure
$\Delta P/L$	Pressure gradient
Q	Volumetric flow rate
Q_P	Volumetric flow rate through a pore
Q_T	Total volumetric flow rate
R	Radius of the tube
r	Radial distance from the of the tube's centre
Δr_{pore}	Error in pore radius
r_h	Hydraulic radius
R_e	Reynolds number
r_{pore}	Radius of a pore
t	Time
v_{pore}	Interstitial velocity
v_{ave}	Empty tower or average flow velocity
v_{wall}	Slip-wall velocity
$v_z(r)$	Velocity of the liquid in the z-direction
u, v and w	Velocity vectors in the x, y and z directions, respectively

Greek Symbols

ρ	Density
$\lambda_{emission}$	Emission wavelength
$\Delta\varepsilon$	Error in porosity
$\lambda_{excitation}$	Excitation wavelength
ξ	Plug along the axial direction
ε	Porosity
τ	Tortuosity factor
η	Viscosity of the medium

Chapter 1: Introduction

A porous media having interconnected pores within its three-dimensional structure corresponds to a network of fluidic channels [1, 2]. Depending on the pore size, the dimension of these fluidic channels varies from milli- to nanometer scale [3]. Therefore, the study of fluid flow through micro and nanoporous structures falls into the categories of microfluidics and nanofluidics, respectively [4].

Nanoscale forces, such as hydrophobic interactions, van der Waals forces, electrostatic interactions between charged entities, are overlooked in macroscale fluid flows [5]. However, these forces significantly impact smaller scale fluid flows, especially in the case of micro and nanoporous media flows depending on the fluid-solid surface interaction [6]. In this work, we focus on understanding the flow behaviour of viscous fluids through micro and nanoporous media. The fundamental questions we are concerned about are – at which size scale do macroscale assumptions for fluid flow break down? How does the interaction of the fluid with solid surfaces change these assumptions within micro and nanoscale fluidic channels?

1.1. Importance of the study of micro and nanoporous media flow

Fluid transport through micro and nanoporous media has significant relevance for high-pressure liquid chromatography with 1 micron or less particle size. Figure 1.1 represents the flow patterns in liquid chromatography columns packed with large or smaller packing particles. The

flow path through a packed column with smaller particles is relatively more uniform, thus lowering the eddy diffusion or multiple path effect. Moreover, the small interparticle space reduces the distance for solute diffusion in mobile and stationary phases, decreasing the mass transfer term (C, in the van Deemter equation). Due to lower mass transfer and eddy diffusion effects, the smaller packing particles reduce the plate height and thus improve the separation efficiency. Therefore, a better separation resolution is obtained in a chromatographic column packed with smaller nonporous particles [7-9].

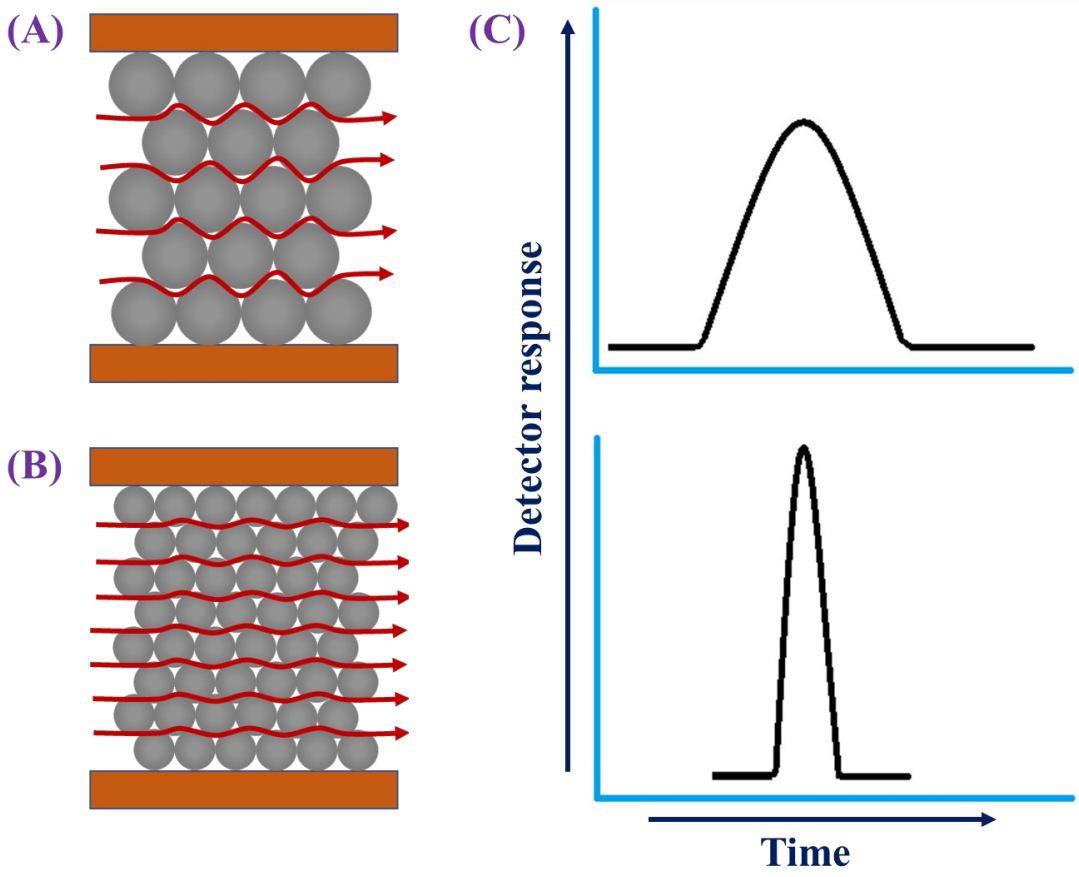

Figure 1.1: Flow pattern in a packed chromatography column with large (A) or small (B) stationary phase packing spheres. This figure was reproduced from the literature with permission [7].

Another benefit of using smaller packing particles in liquid chromatography columns is that solutes have to diffuse through smaller interparticle distances, resulting in a faster optimal flow rate for achieving the minimum plate height. Thus, improved separation efficiency can be achieved in less separation time (as shown in Figure 1.2) [8, 9].

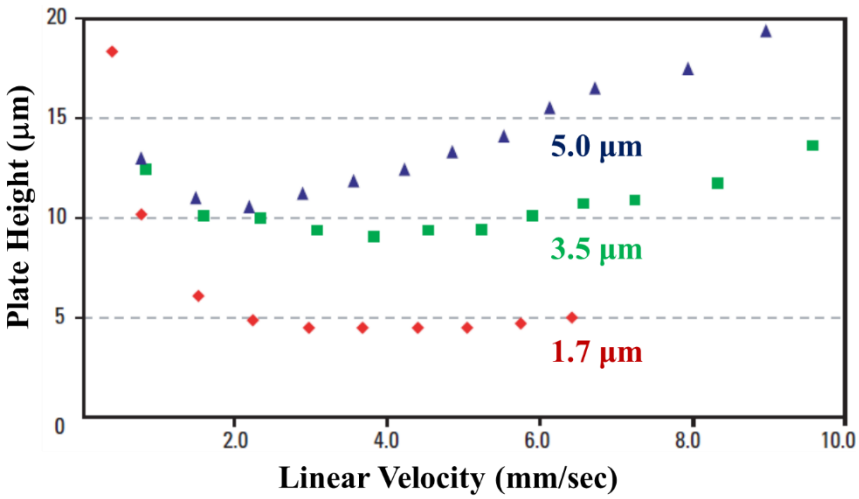

Figure 1.2: Van Deemter curves showing the variation of plate height as a function of linear flow velocity with packing particle diameters of 5, 3.5, and 1.7 microns. The graph was reprinted from the literature with permission [9].

The shortcoming of using smaller packing particles is that the column backpressure increases a lot, since the pressure required to drive the mobile phase through an HPLC column is inversely proportional to the square of particle size [8]. Before the 21st century, larger particles (>3.5 µm) were usually utilized in packing HPLC columns, since the capability of pumps for generating high pressure was limited [10, 11]. Then, through development of very high pressure pumps (more than 14,500 psi) and development of sub-2 µm particle beds, ultra-high-performance liquid chromatography (UHPLC) emerged in the early 2000s [12, 13]. Later, the Wirth group demonstrated that the column backpressure could be reduced (5-20 times) by lowering the surface interaction between mobile phase solvent and stationary phase in a packed column of very small particles (less than 1 µm) [14, 15]. The above discussion clarifies that

particle size is one of the crucial factors in fabricating nanoporous HPLC columns to attain high separation efficiency.

Flow in porous media flow is also related to groundwater hydrology. Water flows through the interconnected pores of porous geological materials, e.g., soils, sands, gravels, fractured rock, etc., and thus is stored underground (as shown in Figure 1.3) [16].

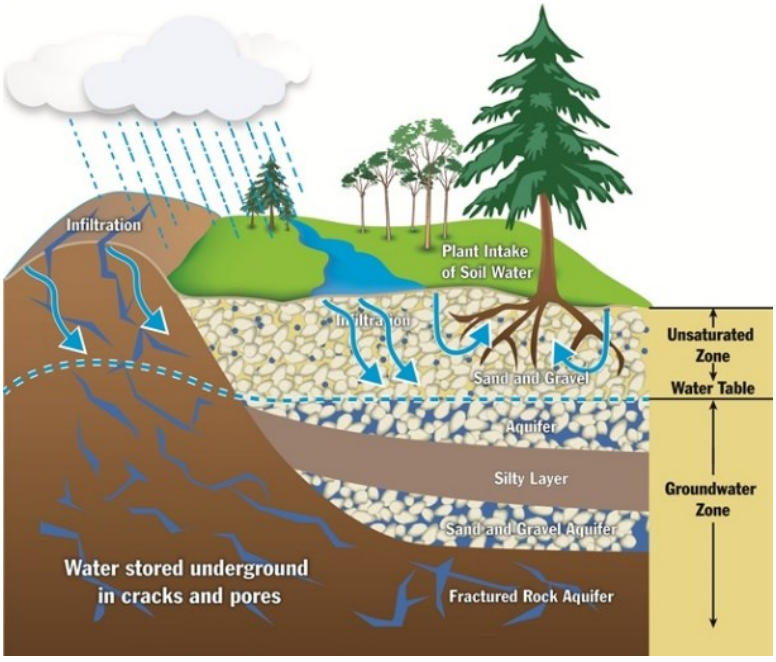

Figure 1.3: Water is stored underground in cracks and pores. This figure is reprinted from the website of the Government of Newfoundland and Labrador with permission. (https://www.gov.nl.ca/ecc/waterres/cycle/groundwater/)

Nanofluidic devices, e.g. nanofluidic "diodes" and various fuel cell designs, are developed utilizing nanoporous media whose performance depends upon the relevant flow principles. Figure 1.4 (A) illustrates a nanofluidic diode developed from silica nanoparticle

crystals. Silica nanoparticles were modified with hydroxyl and amino groups and then packed separately in two segments in a single micropore. In neutral pH, hydroxyl and amino group modified silica nanoparticles become negatively and positively charged, respectively. In de-ionized water, the intrinsic ion concentration is very low, and the electrical double layers of surfaces will overlap when the distance between surfaces is low enough. Under that circumstance, the charged nanoparticles packed in separate segments act like p-type and n-type semiconductors, but this characteristic is only observed in nano-pores. With the application of positive and negative voltages on the p-type and n-type segments, the diode generates forward and reverse ionic current, respectively [17]. Micro and nanoporous fluidic transport mechanisms also play a significant role in energy production using fuel cells [18, 19]. Figures (B) and (C) illustrate representations of nanofluidic fuel cells where the liquid fuel, oxidant and by-product flow and diffuse through the nanoporous electrodes and catalyst layers.

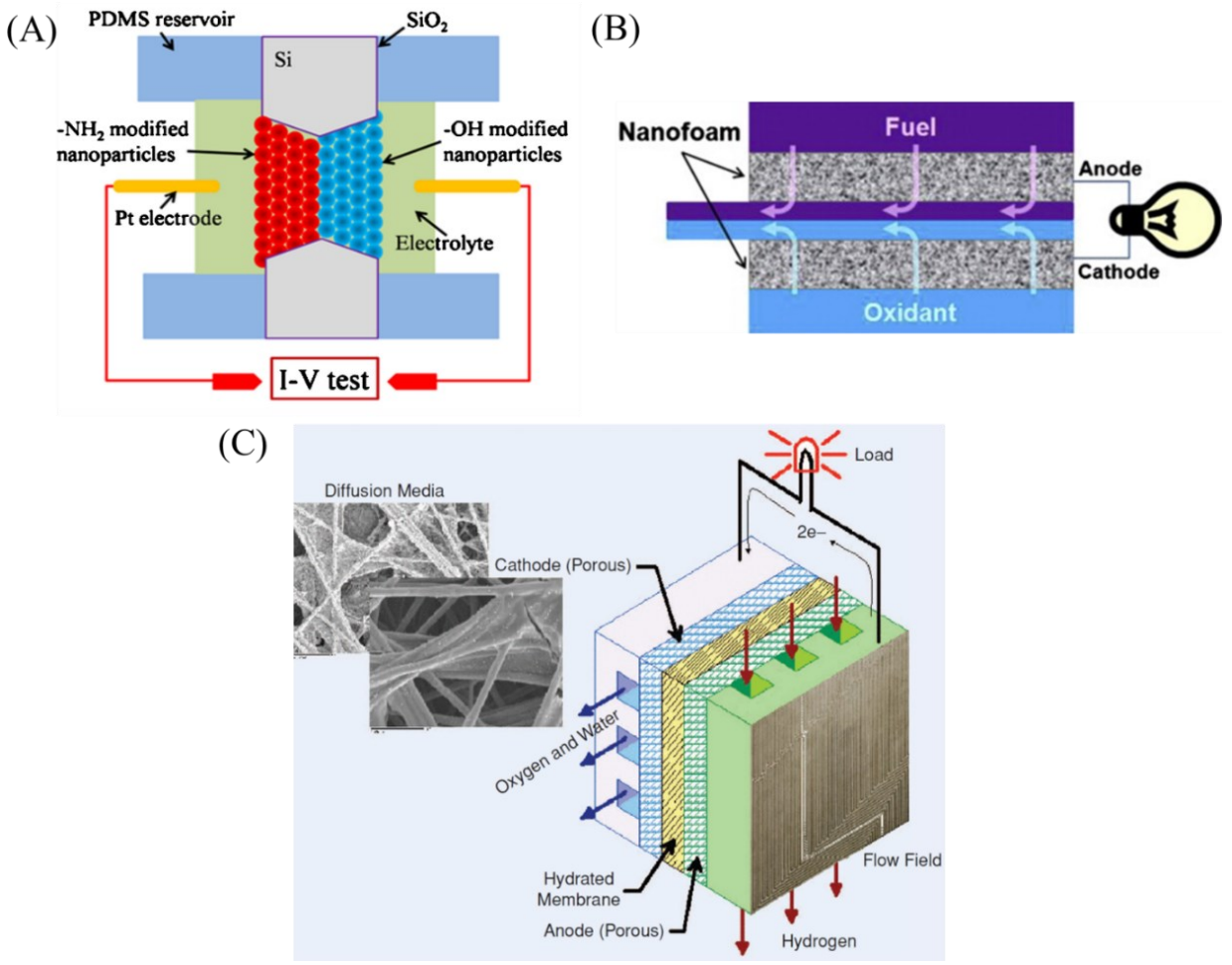

Figure 1.4: Nanofluidic diode developed from silica nanoparticle crystals (A) [17]. Nanofluidic fuel cells where the liquid fuel, oxidant and reaction by-product flow and diffuse through the nanoporous electrodes (B) and (C) [18, 19]. These figures are reprinted from literature with permissions [17-19].

Most importantly, nanoporous media flow is very important in oil and gas recovery applications. The conventional oil and gas reservoirs usually have higher permeability from 0.1 to 100 millidarcy units. In comparison, the permeability of unconventional reservoirs is very low,

often less than 0.1 millidarcy since the pore spaces between the mineral grains are poorly interconnected. Specifically, the permeability of the shale layer is extremely low (as shown in Figure 1.5). The pores in the shale layer range in size from micrometres to nanometers (2–100 nm) [20].

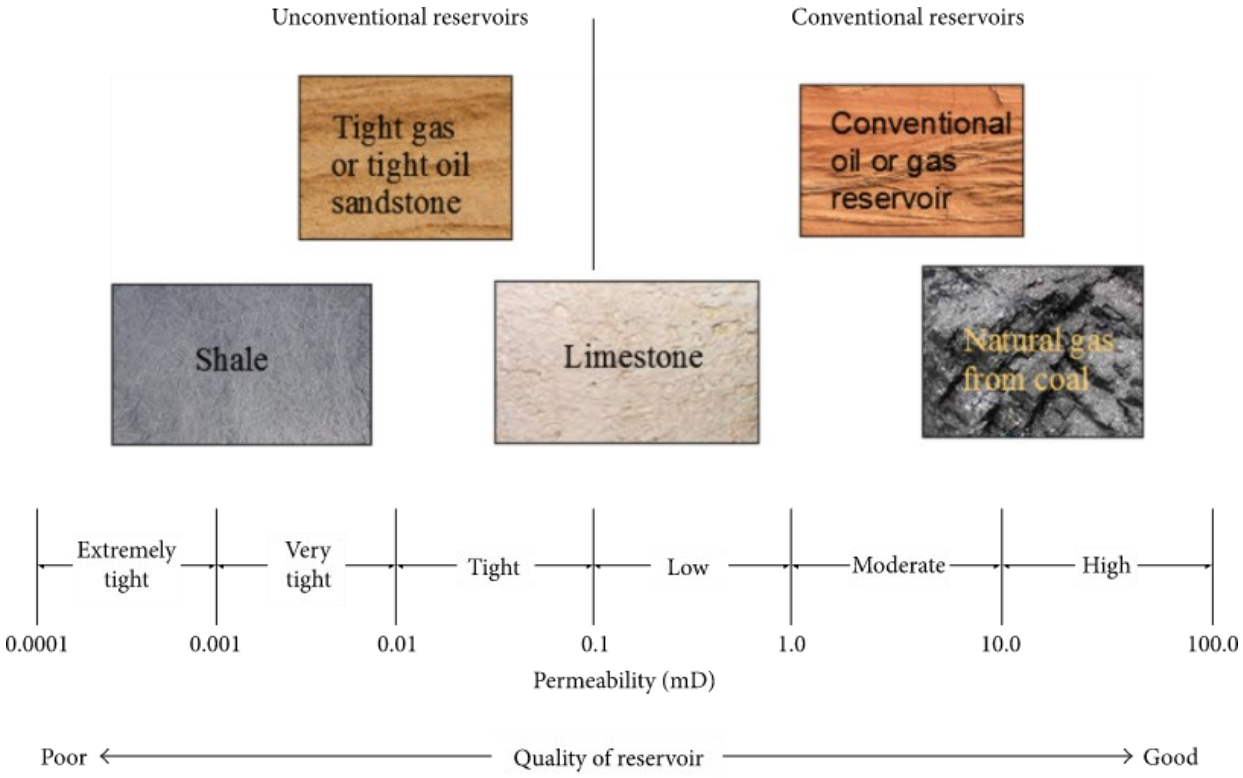

Figure 1.5: Variation of permeability in the conventional and unconventional oil and gas reservoirs. The figure was reprinted from the literature with permission [21].

Increasing energy demand worldwide has shifted the oil and gas industry's focus towards unconventional energy resources. Recent technological advancement in hydraulic fracturing (fracking) has drastically improved oil and gas production from challenging unconventional

resources, especially in North America. In conventional oil and gas reservoirs like in Middle East oil fields, the pores, i.e., the spaces between the mineral grains of rock, are large and well connected. Hence, the oil and gas recovery from these sources is very efficient and highly productive in yield. However, in unconventional oil and gas reservoirs, pores are much smaller (less than 100 nm) and very poorly connected, making oil and gas recovery difficult. Therefore, only 50-60% of the original oil and gas in place in most oil reservoirs can be recovered by existing oil and gas recovery techniques. The rest of 40-50% of resources remain unrecoverable due to the low permeability of the reservoirs. In addition, there are variations in the types of rocks and properties of oil and gas in different sources, and the same fluid interacts differently with different kinds of rocks [22, 23]. Hence, to get a much-needed insight into improving the oil and gas recovery from unconventional sources, it is necessary to understand how fluid flow behaviour changes in micro- and nano-channels found in reservoir conditions [24].

One of the well-established concepts in classical fluid mechanics is the no-slip boundary condition, which assumes that the fluid layer next to the solid surface has zero velocity relative to the surface [25]. The no-slip boundary condition has been successfully used to predict fluid flow in macroscale fluidic channels. However, when the fluidic channels get smaller, the no-slip boundary condition loses accuracy in predicting the micro and nanoscale fluid flows [26, 27]. There are many pieces of evidence that slip flow occurs mainly at nanoscale ranges. For example, an average velocity for different fluids flowing through 7 nm pores in an aligned sealed array of multiwalled carbon nanotubes (MWCNT) was more than 4000 times greater than the predicted flow velocity using no-slip boundary condition [28]. A recent study by Zhong et al. [27] found

that water flow resistance increased in hydrophilic silica nanochannels whereas dropped in hydrophobic graphene nanochannels. In addition, Rogers et al. reported that water experiences slip flow through hydrophobic butyl chain coated silica porous bed, and the extent of flow enhancement increases in smaller scale porous structures [26]. Literature covers a detailed history of the slip flow observations in the last two centuries [29]. Lauga et al. reported an extensive summary of slip lengths, a measure of flow enhancement, determined by various experimental and theoretical methods for different fluid-surface systems [30].

In the case of predicting oil and gas production, researchers develop models primarily focusing on macro- or milliscale flows. First, they apply Navier-Stokes types solutions and no-slip boundary conditions essentially [31]. Then they compare or cross-check their models to known experimental results available in the literature for larger pore scales. In contrast, there is much less experimental data available to use in modelling nanoscale flows, which are important scales in oil recovery from shale layers using the fracking process.

There are few theoretical and experimental studies found in literature on fluid flow in nanofluidic structures. However, a wide range of slip length and flow enhancement with several orders of magnitude discrepancies is present among the available theoretical and experimental results, as shown in Table 1.1. Furthermore, most of these systems represent micro- or nanofluidic channel systems but not true porous media.

Table 1.1: Comparison of the extent of slip flows for various fluid-surface systems.

Substrate	**Fluid type**	**Pore size (nm)**	**Slip length**	**Flow enhancement**	**Method**
Carbon membrane	C_6H_{14}	7	9.5 μm	~1×10^4	Experimental [28]
	$C_{10}H_{22}$		3.4 μm	~4×10^3	
	C_2H_5OH		28 μm	~3.2×10^4	
Amorphous carbon nanopipes	$C_{10}H_{22}$	44	41 nm	~45	Experimental [32]
	C_2H_5OH		29 nm	~25	
Glass + photoresist	$C_{16}H_{34}$	40–200	25–30 nm	-	Experimental [25]
	$C_{10}H_{22}$		~14 nm	-	
	C_6H_{14}		~9 nm	-	
	Water		-	No-slip	
C_4H_9-coated silica porous bed	H_2O	20-220	63 ± 3 nm	2-20	Experimental [26]
	Toluene		-	No-slip	
Carbon nanotube	$C_{10}H_{22}$	3	100.7 nm	~200	Molecular Dynamics Calculation [33]
Graphene slit	C_8H_{18}	2-11	90-185 nm	70-600	Molecular Dynamics Calculation [34]
Quartz slit	C_8H_{18}	2-11	< 1 nm	-	Molecular Dynamics Calculation [20]

Therefore, it is essential to study the pore-scale transport phenomena of viscous fluid in a well-structured micro- and nanoporous media with a proper experimental setup, which will mimic the reservoir conditions. That is why we aimed to develop silica micro and nanoporous media, which would allow us to study flow properties at high pressure in varying sizes of micro- and nanofluidic channels. Moreover, we used both hydrophilic and hydrophobic types of viscous liquids to study the effect of surface interaction on micro- and nanofluidic flow phenomena, which will help theorists to model for micro- and nanoporous media fluid flow.

1.2. Fundamentals of fluid mechanics

In classical fluid mechanics, the Navier- Stokes equations describe the velocity of viscous fluids in relation to pressure, temperature, and fluid density [35]. The following partial differential equations represent the simpler forms of Navier-Stokes equations derived for Newtonian and incompressible fluid [36]:

Continuity equation:

$$\frac{\partial u}{\partial x}+\frac{\partial v}{\partial y}+\frac{\partial w}{\partial z}=0 \quad \text{.....(1.1)}$$

In x-direction:

$$\rho\left(\frac{\partial u}{\partial t}+u\frac{\partial u}{\partial x}+v\frac{\partial u}{\partial y}+w\frac{\partial u}{\partial z}\right)=-\frac{\partial P}{\partial x}+\mu\left(\frac{\partial^2 u}{\partial x^2}+\frac{\partial^2 u}{\partial y^2}+\frac{\partial^2 u}{\partial z^2}\right)+\rho g_x \quad \text{.....(1.2 a)}$$

In y-direction:

$$\rho\left(\frac{\partial v}{\partial t}+u\frac{\partial v}{\partial x}+v\frac{\partial v}{\partial y}+w\frac{\partial v}{\partial z}\right)=-\frac{\partial P}{\partial y}+\mu\left(\frac{\partial^2 v}{\partial x^2}+\frac{\partial^2 v}{\partial y^2}+\frac{\partial^2 v}{\partial z^2}\right)+\rho g_y \quad \text{.....(1.2 b)}$$

In z-direction:

$$\rho\left(\frac{\partial w}{\partial t}+u\frac{\partial w}{\partial x}+v\frac{\partial w}{\partial y}+w\frac{\partial w}{\partial z}\right)=-\frac{\partial P}{\partial z}+\mu\left(\frac{\partial^2 w}{\partial x^2}+\frac{\partial^2 w}{\partial y^2}+\frac{\partial^2 w}{\partial z^2}\right)+\rho g_z \quad \text{.....(1.2 c)}$$

A Newtonian fluid has a constant viscosity, and an incompressible fluid is one for which the density of the fluid is constant [37]. The first equation (1.1), a time-dependent continuity equation, was derived from the basic principles of the conservation of mass. The 2nd set of equations (1.2 a-c) was derived from the conservation of momentum, which is newton's 2nd law of motion. The time (t) and spatial coordinates (x, y, and z) are independent variables. Pressure (P), density (ρ), acceleration of gravity vectors (g_x, g_y and g_z in the x, y and z directions, respectively), and velocity vectors (u, v and w in the x, y and z directions, respectively) are dependent variables as a function of independent variables (time and spatial coordinates). The essential assumptions made for formulating the above Navier–Stokes equations were [38, 39]

a) The fluid is a continuous substance rather than discrete particles, i.e., a continuum at the scale of interest.
b) The fields of interest (pressure, flow velocity, density) are differentiable.
c) Viscosity and density of fluid are constant.
d) Laws of mass and momentum conservation are followed.

A liquid flowing through a cylindrical tube attains a parabolic velocity profile (as shown in Figure 1.6), which can be derived directly from Navier-Stokes equations by considering the following assumptions [40]:

a) the fluid is incompressible and Newtonian;

b) the flow is steady-state as well as laminar through a cylindrical tube where the tube length is significantly longer than its cross-sectional diameter;

c) the acceleration of fluid in the tube is zero.

d) The velocity, $v_z(r)$, varies along with the radial distance of the tube. It is maximum at the centre (r = 0) of the tube and disappears at the tube wall (r = R), i.e., the fluid layer in contact with the solid wall does not have any velocity in relation to the solid boundary wall.

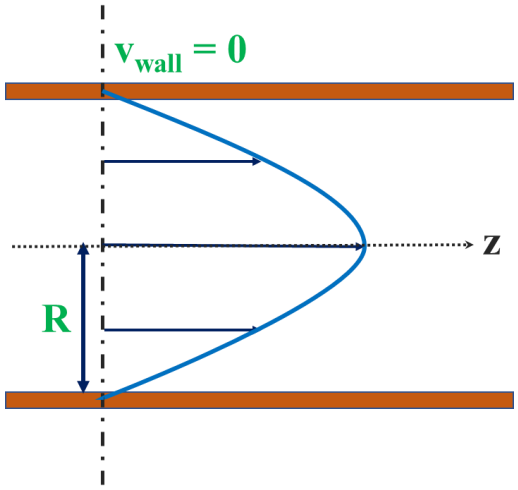

Figure 1.6: Velocity profile at no-slip boundary condition.

Therefore, in the no-slip boundary condition, the velocity of a liquid flowing in a cylindrical tube of radius R is expressed as [41]:

$$v_z(r) = \frac{\Delta P}{4\eta L}(R^2 - r^2) \quad \text{.....(1.3)}$$

where,

$v_z(r)$ is the velocity of the liquid in the z-direction

ΔP is the applied pressure,

η is the dynamic viscosity of the liquid,

L is the length of the tube,

R is the radius of the tube,

r is the radial distance from the of the tube's centre.

Then, considering the whole cross-sectional area of the tube, integration of the above equation yields the following equation (1.4) of volumetric flow rate through the tube –

$$\Delta P = \frac{8Q\eta L}{\pi R^4} \quad \text{(1.4)}$$

According to the above equation (known as the Hagen-Poiseuille equation), the volumetric flow rate (Q) for a laminar flow through a long cylindrical pipe of a constant cross-section at no-slip boundary condition is directly proportional to the pressure gradient and inversely proportional to the fluid's viscosity [42].

Darcy's law describes the fluid flow through porous media, which was formulated based on the experimentally obtained water flow results through sand beds [31]. The Darcy equation (1.5) is used to determine the permeability (k) of the porous bed [43]:

$$\frac{Q}{A} = v = \frac{-k\Delta P}{\eta L} \quad \text{(1.5)}$$

where,

Q is the flow rate through the porous bed,

A is the cross-sectional area of the porous bed,

v is the average linear flow velocity through the packed bed,

k the permeability of a porous bed,

η is the dynamic viscosity of the fluid,

ΔP is the applied pressure for fluid flow, and

L is the length of the porous bed.

The negative sign in the Darcy equation indicates that fluid flows from a higher pressure zone to a lower pressure zone, which is the opposite direction of the increasing pressure gradient. Darcy's equation can be derived from the Navier–Stokes equations using the assumption of no-slip boundary conditions [44]. Similar to the Hagen-Poiseuille equation, the volumetric flow rate is directly proportional to the pressure gradient and inversely proportional to the fluid's viscosity. Darcy's law is only valid in the laminar flow regime. A similar form of Darcy's equation is the Kozeny-Carman equation (1.6), which gives the measure of the porosity of a bed packed with spherical particles [45, 46]. In this case, the permeability (k) is expressed in terms of the bed porosity (ε) and particle diameter (d_p) of the porous bed [47, 48].

$$\frac{Q}{A} = \frac{d_{particle}{}^2 \varepsilon^3 \Delta P}{180\eta(1-\varepsilon)^2 L} \quad \text{.....(1.6)}$$

1.3. Porous media

A porous media is a solid structure containing interconnected pores or void spaces that transports fluids under pressure gradients [2, 31, 49]. In the literature, one finds mention of different types of porous media, with varying pore sizes and size distributions. Several different types of porous media of relevance to separation science and hydrology are mentioned briefly below.

Porous polymer gel matrices are used as porous media in gel electrophoresis for the size-based separation of proteins [50, 51]. An SEM image of a polyacrylamide gel structure is shown in Figure 1.7. However, a wide distribution of pore sizes can be present in the polymer gel porous structures, producing eddy diffusion like random paths [52]. Therefore, the fluidic channels generated from the interconnected pores lack uniform diameter throughout their length. More rigid polymer structures were used by Mei et al. for protein separation by electrophoresis [53], utilizing porous polymer monolithic beds. In that work, the pores formed within these monolithic beds were micron-sized (0.4 to 3.2 μm), and the porous structures were stable for low pressure (less than 200 kPa) flow measurements, with good flow stability and reproducibility [53, 54]. The pressure-flow velocity measurement technique used in those latter studies was employed in this thesis work as well, with some specific modifications.

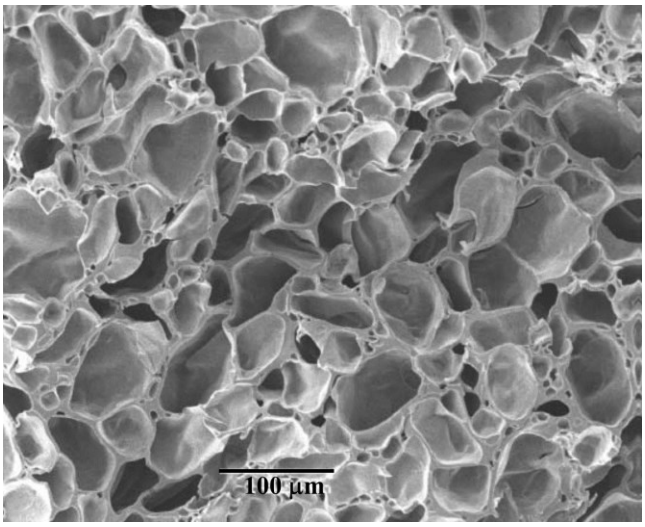

Figure 1.7: An SEM image of polyacrylamide gel. The figure was reprinted from the literature with permission [52].

On smaller scales, there have been reports of flow measurements through membranes of aligned carbon nanotubes (as shown in Figure 1.8) having diameters of 7 nm [28] and less than 2 nanometers [55]. However, these straight flow channels may not accurately predict the flow properties in the tortuous path existent in many porous media. Moreover, the fabrication of these nanostructures is an added challenge.

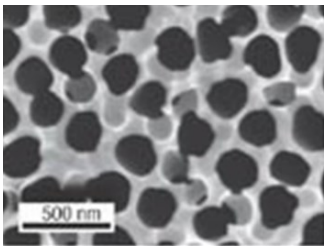

Figure 1.8: SEM image of the carbon membrane surface. The figure was reprinted from the literature with permission [56].

Sinton's group developed different porous structures for various applications. For example, Berejnov et al. [2] used a microfluidic network structure (PDMS chip) containing ~5000 channels (10-80 μm width and ~25 μm depth) as the porous media for demonstrating a multiphase flow study in porous media. Hasham et al. [57] employed a glass based microfluidic chip having nanopore networks (175 nm depth) to study the pore-scale fluid displacement of fracturing fluids (deionized water, slick water and KCl solution) during hydraulic fracturing. Song et al. [58] fabricated a porous structure (having squares separated by 300 μm wide channels) by etching calcite-based natural rock for visualizing the dissolution effects of fluids on the rock material. Moreover, porous micromodel structures (as shown in Figure 1.9) were used in various oil recovery [59, 60] and mineralogy [61] applications.

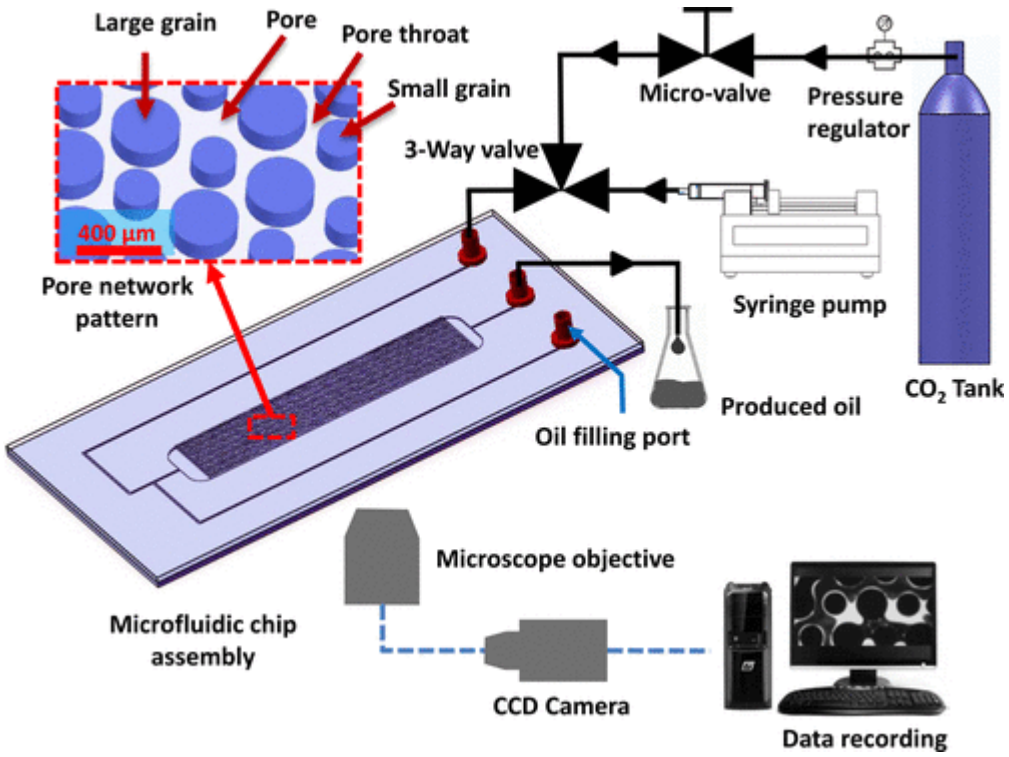

Figure 1.9: Experimental setup used in oil recovery application includes a porous micromodel structure which consists of regularly spaced circular posts to create ~120−200 µm diameter pores and ~70 µm diameter pore throats. The figure was reprinted from the literature with permission [59].

Packed beds of solid particles having spherical or irregular shapes have been used in studying the porous media flow properties. For example, in recent times, Datta et al. utilized packed bed of spherical glass beads for visualizing the spatial fluctuations of flow velocities [24, 62]. However, these micron-sized (32 ± 2 µm) glass beads produced a macroporous media having larger pores (> 1 µm), which does not represent a nanoporous media present in part in an oil and gas reservoir or a UHPLC packed column. In contrast, there are several earlier reports of using

colloidal self-assembly (CSA) of nanoparticles as a sieve structure in separation science. The three-dimensional structure of the pore network created in the interstitial spaces of assembled nanoparticles makes colloidal self-assembly (CSA) of nanoparticles an attractive choice as a micro- and nanoporous media (as shown in Figure 1.10).

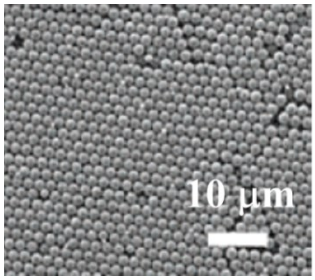

Figure 1.10: An SEM image of CSA of 2-µm polystyrene particles packed within a microchannel. The figure was reprinted from the literature with permission [63].

CSA of nanoparticles was utilized to form a nano-porous stationary phase as a separation matrix in a microfluidic channel, especially for separations of proteins [63-65] and DNA [63]. Wirth et al. packed C4 alkyl chain coated silica particles of different sizes into the capillary column, studied the flow velocities variation for different pore sizes at various high-pressure settings (up to ~10,000 psi) [26].

To mimic the condition of low permeable oil and gas reservoirs and normal phase high-pressure liquid chromatography, we have developed porous media by packing silica nanoparticles inside the fused silica microcapillary tube. This type of porous media is easy to fabricate and mechanically robust, allowing tests of fluid flow rates from low to very high pressure.

1.4. Outline of this thesis

Chapter 2 focuses on the instrumentation utilized to accurately measure linear flow velocity at constant pressure for characterizing the porous media and its flow properties. The details about how the fluidic setup, constant pressure pump and optical detection unit were built are described. The method of determining linear flow velocity using the time of flight photobleaching velocity measurement technique is also discussed.

To study fluid dynamics in micro and nano scale, building a micro- and nanofluidic channel system structure is essential. Chapter 3 discusses the fabrication of porous media and its characterization. To mimic the condition of low permeable oil and gas reservoirs and normal phase high-pressure liquid chromatography, we develop micro- and nano-porous media suitable to test fluid flow from low to very high pressure. The variation in packing quality with respect to fabrication conditions is discussed. The relationship between porosity and permeability of the porous beds is explored and compared with theory.

In Chapter 4, we have explored the pore-scale transport phenomena of non-wetting (n-octane) and wetting (water) fluids in a silica porous media. Experimental velocity is compared with the theoretical velocity to determine the existence of slip or no-slip flow phenomenon. The flow properties within pores are also discussed. The effective and absolute permeabilities were compared in the presence of a wetting fluid layer.

In Chapter 5, we have discussed the effect of pore size on the variation of flow rate enhancement for a non-wetting fluid (n-octane) through silica micro and nanoporous media. The obtained results are compared with the theoretical observations found in the literature and discussed.

In Chapter 6, we report how the flow characteristics of 1-octanol, which has both wetting (hydroxyl group) and non-wetting (octyl group) parts for silica surface, change with the varying pore sizes in silica micro- and nanoporous media. 1-octanol is about 14 times more viscous than n-octane, although 1-octanol has the same length of straight alkyl chain (C_8H_{17}-) in its structure as n-octane. Hence, a comparison between the flow behaviours of 1-octanol and n-octane in silica micro and nanoporous media is made and discussed.

Finally, Chapter 7 summarizes the findings of this thesis, together with some future views and potential research directions.

Chapter 2: Instrumentation

2.1. Introduction

Linear flow velocity is the imperative parameter to describe porous media flow properties properly. Moreover, the pressure-velocity relationship is useful for measuring the porous bed's permeability and porosity, according to the Darcy and Kozeny-Carman equations, respectively. Therefore, an accurate measurement of linear flow velocity at constant pressure is needed to characterize the porous media itself.

Hot-wire anemometry, Venturi- and Pitot tube methods are the classical techniques for measuring flow velocity, but they are not suitable in micro- and nanofluidic systems, because flow could be disturbed during measurement, or the fluidic channel is too small for the experimental setup [66]. On the other hand, particle-based techniques, e.g. micro laser doppler velocimetry (μ-LDV) and micro particle imaging velocimetry (μ-PIV), have been utilized in microchannels with dimensions > 10 μm [67-69]. The typical size of the tracer particles used for these techniques varies from 200 nm to 2 μm [68, 70], which is relatively large compared to the pore diameter of the micro- and nanoporous beds that are the subject of our interest. The tracer particle can block the pores in a micro- or nano-porous bed, disrupting the flow. Therefore, particle-based velocimetry techniques are also not suitable for measuring flow velocity in micro- and nanoporous systems.

Here we have used a time of flight, photobleaching velocity measurement technique. A fluorescent dye stream flowing at constant pressure is photobleached to create a zone of reduced dye concentration, and its time of travel is monitored by laser-induced fluorescence detection. This technique was previously applied in Harrison's group by Bao [71], and later on by Mei [54], to evaluate the fluid dynamics of aqueous solution in micron-sized flow restrictors and porous monoliths photopatterned within microfluidic channels, respectively, at very low pressure (< 30 psi). We have adopted this method to investigate the flow properties for both aqueous and nonaqueous phases through micro- and nanoporous bed at much higher pressures of 150-5500 psi. The instrumentation developed is described in this chapter.

2.2. Experimental

2.2.1 Dye solution

Fluorescein disodium salt (Sigma, St. Louis, MO) was used as a fluorescence tracing dye, using ultrapure water as the solvent. Distilled water was deionized by a Milli-Q UV Plus Ultra-Pure water system (Millipore, Milford, MA). Deionized water (18.2 MΩ) was then degassed by ultrasonication several times to remove tiny suspended gas bubbles or dissolved gas from the liquid. Degassed water was stored in a capped centrifuge tube with no included air volume.

A portion of the degassed ultrapure water was sparged with O_2 gas (Praxair, Mississauga, ON, Canada) for 2 hours to give oxygen-saturated water. A tube connected with the gas regulator

was submerged into the water, and then oxygen was delivered at a moderate flow rate (10 psi gas delivery pressure) for sparging.

The dye solution (38 μM) was prepared by dissolving fluorescein disodium salt dye into a portion (250 mL) of the degassed ultrapure water. This concentrated dye solution was then filtered through a 0.22 pm pore size filter (Millipore, Bedford, MA) to remove any undissolved dye particulates. For flow experiments, a dilute (190 nM) fluorescein solution was prepared by mixing the required amount of concentrated solution (38 μM), fully degassed water and fully oxygen-saturated water, where the volume of the oxygen-saturated water was kept at 50% of the total volume of the final solution. A fluorimeter was used to record the excitation and fluorescence emission spectra of the fluorescein dye solution.

2.2.2 Fluidic setup

Figure 2.1 illustrates the complete fluidic system for the flow experiments. A constant pressure pump system was utilized for the fluid flow. At first, the O_2 sparged dye solution was pipetted into an aluminum foil-wrapped glass vial (1 mL) (to avoid photo reactions) to fill ~90% of its volume. Then, the glass vial (dye reservoir) was placed on a removable plug and was inserted within a gas chamber by attaching the removable plug at the bottom of the gas chamber (as shown in Figure 2.2). A stainless-steel outlet tube (O.D. 1/16", I.D. 0.030") was submerged into the dye solution through another plug above the glass vial. The gas chamber was made of a thick and hollow stainless steel tube, which was mechanically robust, so as to withstand high gas pressure (more than 6000 psi). The fittings associated with this gas chamber were also stainless

steel, giving better leak-free performances than brass-made materials. After the gas chamber was sealed, a pressurized gas (helium or nitrogen gas) was delivered from a gas cylinder (>99.998% purity, Praxair Canada Inc., Mississauga) connected to a high-pressure regulator to pressurize the liquid.

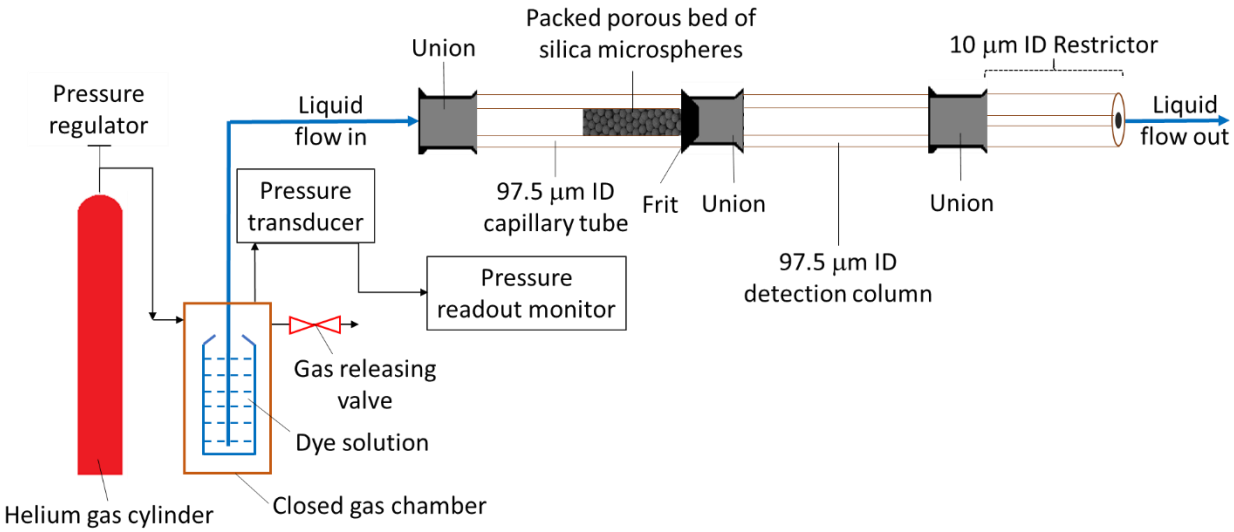

Figure 2.1: Diagram of the fluidic setup having constant pressure pumping unit connected to porous packed bed and velocity detection column.

The pressure regulator (PRS 40925901-677; Praxair Canada Inc., Mississauga) used for helium gas flow was configured with 0-6000 psi outlet pressure, 1/4" FNPT and CGA 677 connections. On the other hand, the nitrogen gas pressure regulator (SEQ3040CGA; Matheson Tri-Gas Inc., Montgomeryville, PA) was configured with 100-2500 psi outlet pressure, 1/4" NPTM and CGA 580 connections. Then, the liquid under the selected gas pressure flowed from the dye reservoir through the tube (L × O.D. × I.D.: 30 cm × 1/16" × 0.030") located deep within the liquid in the dye reservoir (as shown in Figure 2.2) to the rest of the fluidic channels.

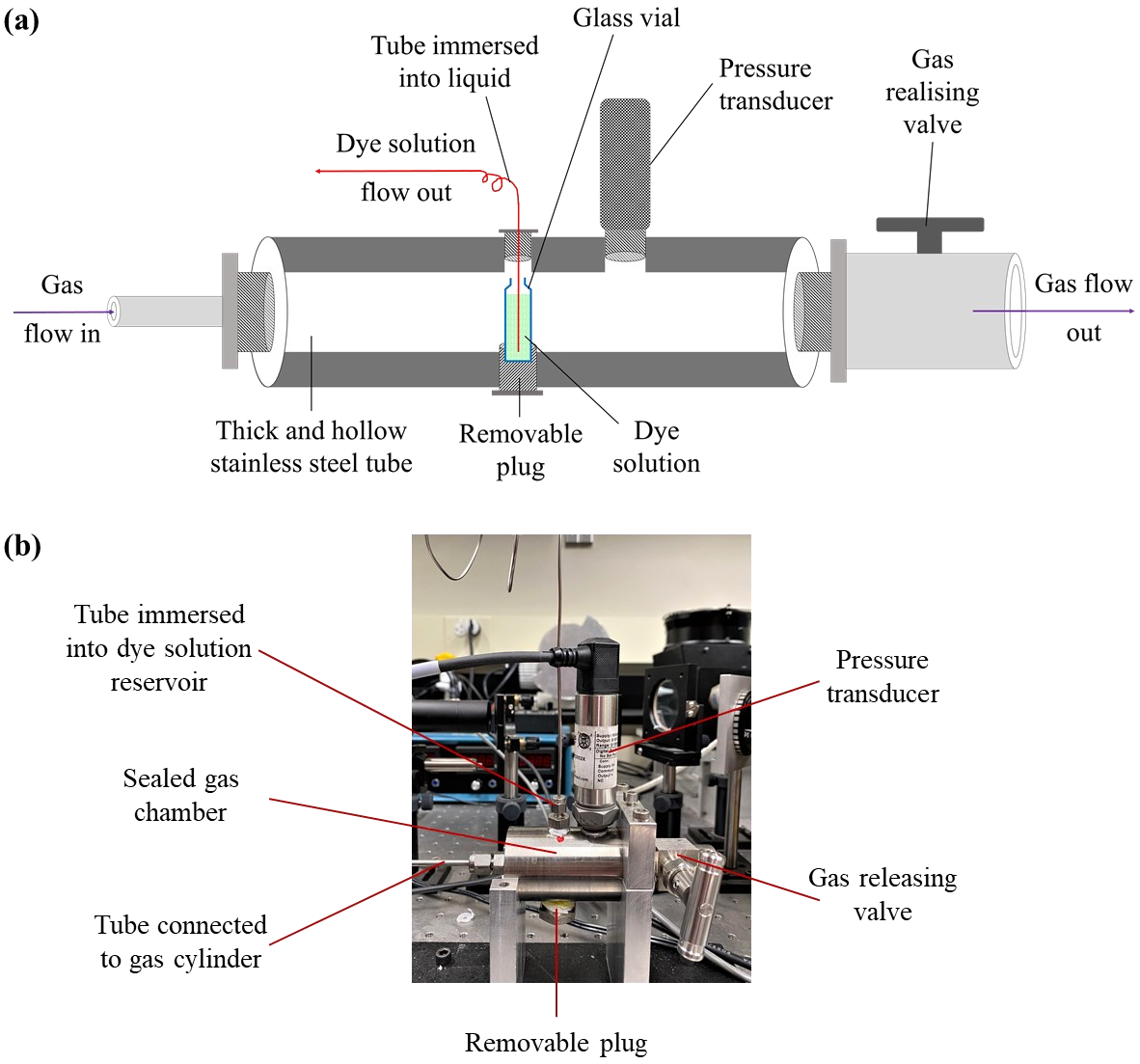

Figure 2.2: A schematic diagram (a) and an image (b) of the closed gas chamber.

A fluidic connection was made between the tube immersed into the liquid and the packed column through a VHP stainless steel union assembly (UH-402, Idex), a 360-micron O.D. fused silica capillary tube (TSP100375, Polymicro Technologies, Molex) and a micro tight union assembly (P-772, Idex). A frit (M-120, Idex) with 0.5-micron pore size was used at the end of

the packed column to keep the porous bed stable inside the capillary against the high backpressure. Then the packed column was coupled with the detection column by an inline micro filter assembly (M-520, Idex).

For the detection column, an empty fused silica capillary tube having the same inner and outer diameter as the packed column was used. An empty capillary (4.5-15 cm long) with a smaller internal diameter (10 μm) was connected with a micro tight union assembly at the end of the detection column. It acted as a restrictor to give some column backpressure, avoiding bubble formation within the liquid stream in the higher pressure regions of the flow system.

A pressure transducer was mounted on the closed gas chamber through a 1/4" NPT Male connection to monitor the actual pressure (range: 0-6000 psi) working on the liquid container, relative to atmospheric pressure. A pressure readout monitor was calibrated within the transducer's output voltage (0-10 volt DC) and connected with the transducer through a 4-pin M12 connector and cable. Any leak in the fluidic system was checked carefully at each connection point with a soapy solution by monitoring any bubble formation. If any leak was detected, the fluidic connection was appropriately tightened. Once a stable flow rate was observed through a consistent fluorescence signal, the pressure value was recorded. Minimal pressure drop (< 0.15%) was observed during the high pressure (>2000 psi) flow experiments throughout the measurement. No significant pressure drop was observed for low or mid-pressure flow experiments (<2000 psi pressure). After flow measurements were completed, the pressure was reduced very slowly by using a gas-releasing valve. Room temperature was recorded over

the course of the flow measurements by a thermometer (0.0IK, VWR) to select viscosity values for the liquids of interest.

2.2.3 Optical setup for linear flow velocity measurements

Figure 2.3 illustrates an optical setup for the linear velocity measurement. The time of flight of a photobleached plug of dye solution was measured to determine the velocity. A 488 nm Ar ion laser (Uniphase-Cyonics, San Jose, CA) operated at 2.5-12 mW was used at high intensity to photobleach the dye. The intense laser beam was focused by a 25/0.35 NPL Fluotar objective (Leitz Wetzlar) to about 150 μm diameter, to photobleach the dye solution flowing at constant pressure through 97.5 μm ID detection column. As the cylindrical-shaped capillary column can act as a lens, the spot size of the incident bleaching beam was kept bigger (~150 μm diameter) than the column's internal diameter (97.5 μm) to eliminate possible mixing of bleached and unbleached solutions. In studies that used a 73.5 or 75 μm internal diameter column, the bleaching spot was focused to 90 μm. The laser beam intensity was increased with respect to the increasing flow rates by raising the laser power to ensure proper photobleaching.

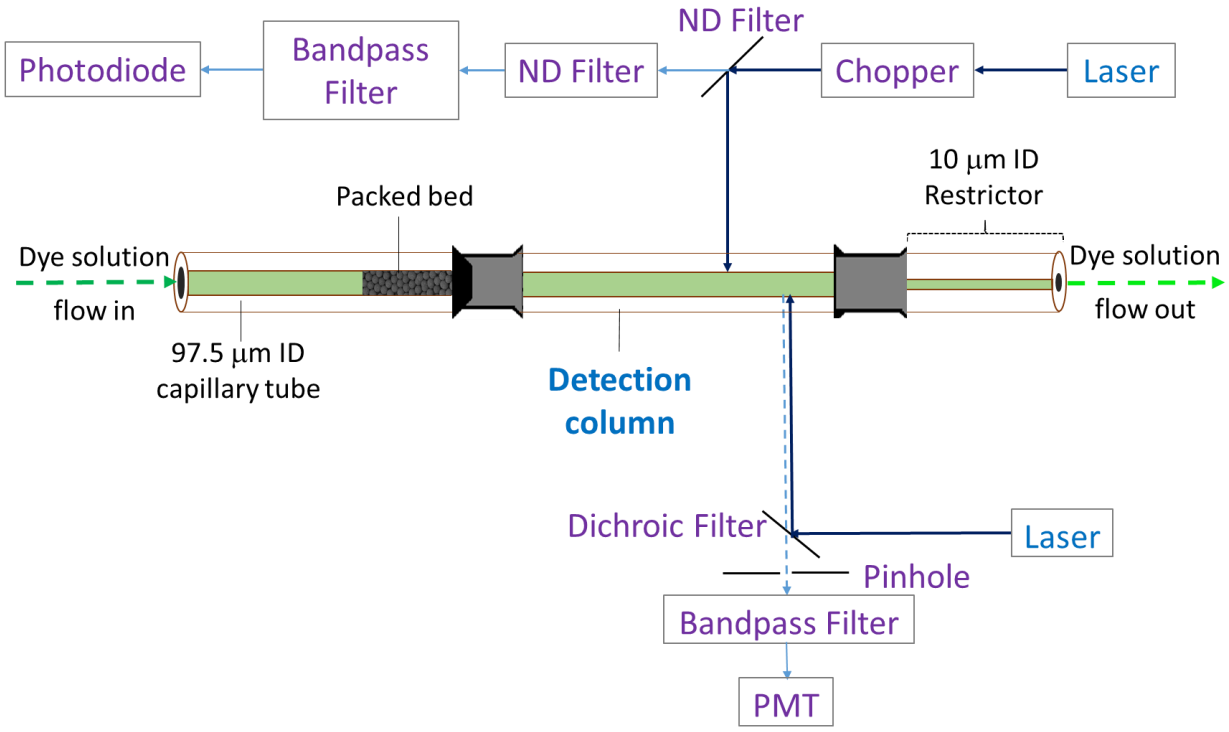

Figure 2.3: An optical setup used for the time of flight, photobleaching velocity measurement. Two lasers, a variety of lenses and filters were used for photobleaching and fluorescence detection.

An optical chopper was operated at a particular frequency to generate a square wave dye concentration variation. When the chopper blocked the laser beam, no photobleaching happened. The unblocked laser beam was directed towards a neutral density filter (ND 3.0, optical density 3) which reflected 99.9% of light to the detection column and transmitted 0.1% light to a photodiode (3 mm, Silicon Detector Corp., Newbury Park, CA). Another neutral density filter (ND 2.0, optical density 2) was used in front of the photodiode to protect it from damage due to

the power of the transmitted laser beam, reducing power of the transmitted laser beam by 99%. A laser line bandpass filter (CWL = 488 ± 0.2 nm) was also utilized to remove room light noise.

A second 488 nm Ar ion laser (Uniphase-Cyonics, San Jose, CA) operated at 2.5 mW was used for laser-induced fluorescence detection. A custom-built inverted, confocal epifluorescence microscope was utilized for this fluorescence detection [72]. The 488 nm laser beam reflected by a 505 dichroic mirror (505DRLP02, Omega) was focused on the detection column by a 10X objective (5709, New Focus, Santa Clara, CA) to excite the dye molecule in the liquid stream. The laser spot diameter in the detection zone was kept smaller (~20 μm) to reduce spatial band broadening. The collected fluorescence light ($\lambda_{\text{emission}} = 514$ nm) was transmitted through the dichroic mirror, a 20 cm f.l. tube lens (Achromat, Newport, PAC064), a 200 μm pinhole (Newport, Irvine, CA), and a 530 ± 30 nm bandpass filter to a photomultiplier tube (PMT; R1477, Hamamatsu) detector.

A detection window (~2.5 cm) was made for the fluorescence measurement by removing a part of the capillary tube's polyimide coating with a burning flame followed by polishing with a wet Kimwipe. The detection column was kept horizontal and vibration-free during the flow measurements on a thick plexiglass column holder by tightening micro-tight nuts (F-125, Idex) from two sides (Figure 2.4).

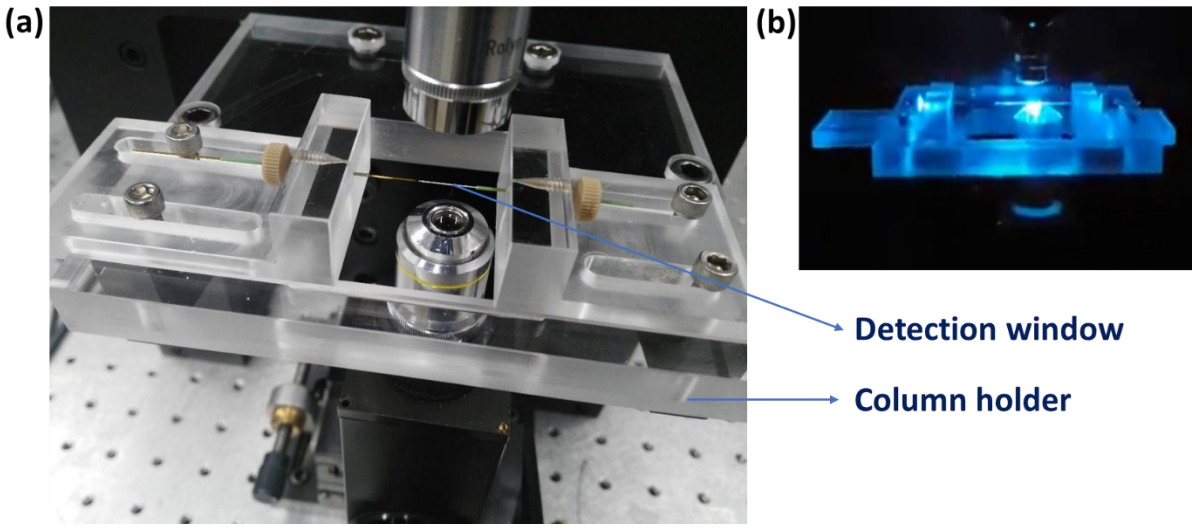

Figure 2.4: (a) A detection column mounted on the column holder, (b) Image showing the incident laser beam on the detection window during fluorescence measurement.

The PMT and photodiode voltage output responses were stored in an Intel Core i5-2500 3.30 GHz 8GB RAM computer through an equipped National Instruments PC+ board by an installed Labview 2016 program (25 kHz acquisition rate, an average of 250 points, 100 Hz net acquisition rate). Then, the data was processed with Origin Pro 2016 software. A Savitzky–Golay differentiation with a 35-point smoothing filter were used to determine the inflection point in the fluorescence curve at the photobleached spot's edges.

The bleaching and detection were done at least 20 cm downstream of the porous bed, instead of measuring upstream, to avoid any possible plugging of the packed bed due to photoproducts. A translation stage (Newport 423, Irvine, CA, USA) equipped with a differential micrometer (Newport DM13) with positioning error < 1 μm was used to set the distance between

the bleaching point and the detection points. The time of flight of the photobleached plug was initially determined at 1 mm away from the bleaching point for about 4-5 pulse periods. Then, the detector spot was moved to 2 mm away from the initial photobleaching point, and the time of flight was again determined for another 4-5 pulse periods. The separation distance between the two measurements was varied over the course of this study, to compensate for the impact of the flow rates between the different columns on the spreading of the edges of the photobleached plug.

2.3. Results and Discussion

2.3.1 Fluorescence signal from the dye solution

Figure 2.5 shows the fluorescence spectra of 2 μM dye solution of fluorescein disodium salt dissolved in ultrapure water. The excitation maximum was found to be 492 nm. Hence, 488 nm Ar ion laser was energetic enough to excite the dye molecules. A 505 nm dichroic mirror was also found suitable to reflect the excitation beam (488nm) and transmit fluorescence signal ($\lambda_{emission}$ = 514 nm). A low concentration of dye solution minimizes the possibility of aggregate formation due to dye-dye interaction during photobleaching [73-75]. However, to get reasonable signal intensity from both photobleached and unbleached plugs of dye solution, the dye solution's concentration needed to be optimized at 190 nM. O_2 used for photobleaching reacts with the excited optical state and competes with dye-dye interactions [71]. However, a high concentration of O_2 can form bubbles in the fluorescent dye solution stream. A 50% saturation of dye solution with O_2 was found optimal for generating a stable square wave fluorescence signal from the photobleaching pulses.

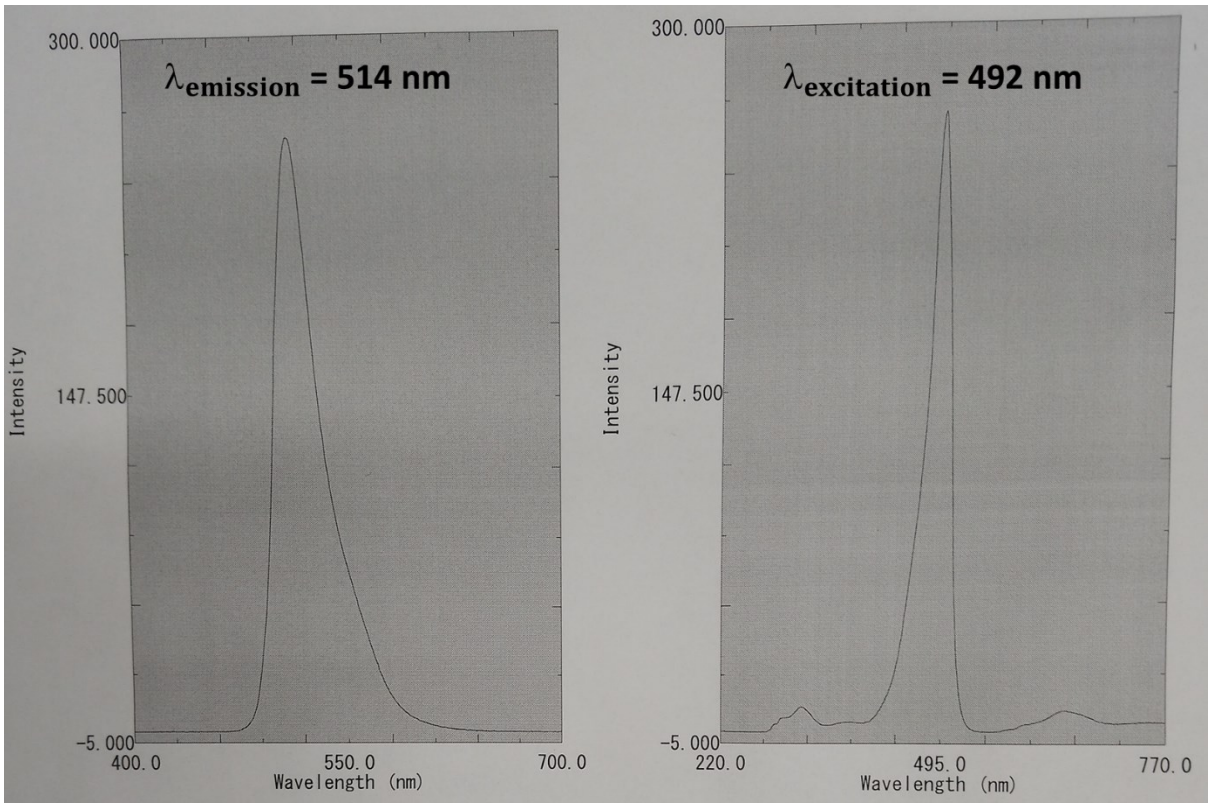

Figure 2.5: Fluorescence spectra of aqueous fluorescein disodium salt dye.

2.3.2 Flow Rate Measurements

A plug of reduced dye concentration was created by photobleaching a zone of fluorescent dye within the flowing solution stream. The time of flight of the bleached plug was determined by measuring laser-induced fluorescence signals at two detection points downstream of the photobleaching spot (Figure 2.6). Then, the linear flow velocity (v) was determined using Equation 2.1.

$$v = \frac{L_2 - L_1}{t_2 - t_1} \quad \text{.....(2.1)}$$

The detection zones (L_1 and L_2) were about 1 and 1.4-3 mm downstream of the bleaching spot, respectively, while t_1 and t_2 correspond to the times required for the bleached zone to reach the first (at L_1) and second (at L_2) detection zones, respectively. Thus, measuring the velocity with two parallel photobleaching tests reduces the error from the size of the laser spots for bleaching and detection and the response time for bleaching.

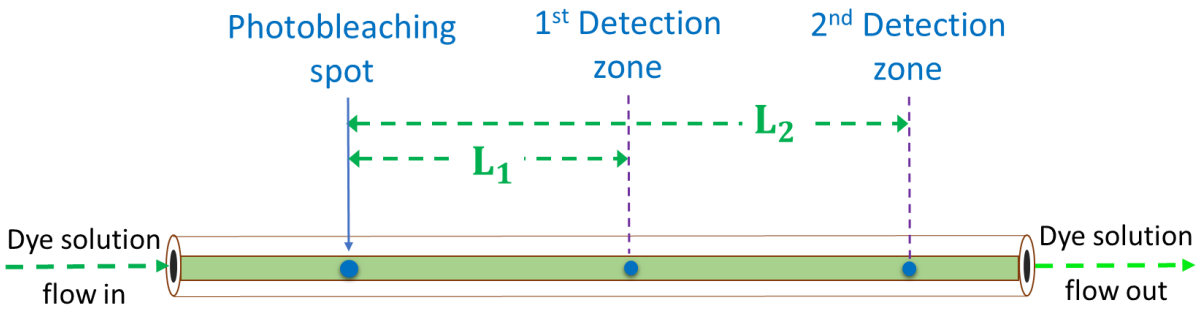

Figure 2.6: An optical detector unit for dual point flow velocity measurement.

Figure 2.7 (a) and (c) illustrate the chopped laser pulses generated for photobleaching and the resulting fluorescence changes observed downstream due to bleaching, respectively. Figure 2.7 (b) and (d) show the differentiated signal peaks used to determine the edges of the bleached zone with improved precision. The first diode rising edge means bleaching has started (at 8.15 sec), and the first falling detector edge means the bleached plug reached the detector (at 10.4 sec). The difference between these two edges gives the first t_1 (=2.25 sec). Similarly, the first falling diode edge means bleaching stopped (at 15.1 sec), and the first rising detector edge means the undamaged dye front has now reached the detector (at 17.45 sec). Thus, the difference between these two edges gives the second t_1 (=2.35 sec). Likewise, several values of t_2 can be determined

after translating the laser detection point 0.4-2 mm away from the first detection spot (at L_1). Then, the differences between the respective t_1 and t_2 values for several cycles are taken to measure the velocity values (v_1, v_2, v_3, …..) at the same pressure, according to Equation 2.1. The average linear velocity with standard deviation is then calculated from the data of 4-5 cycles.

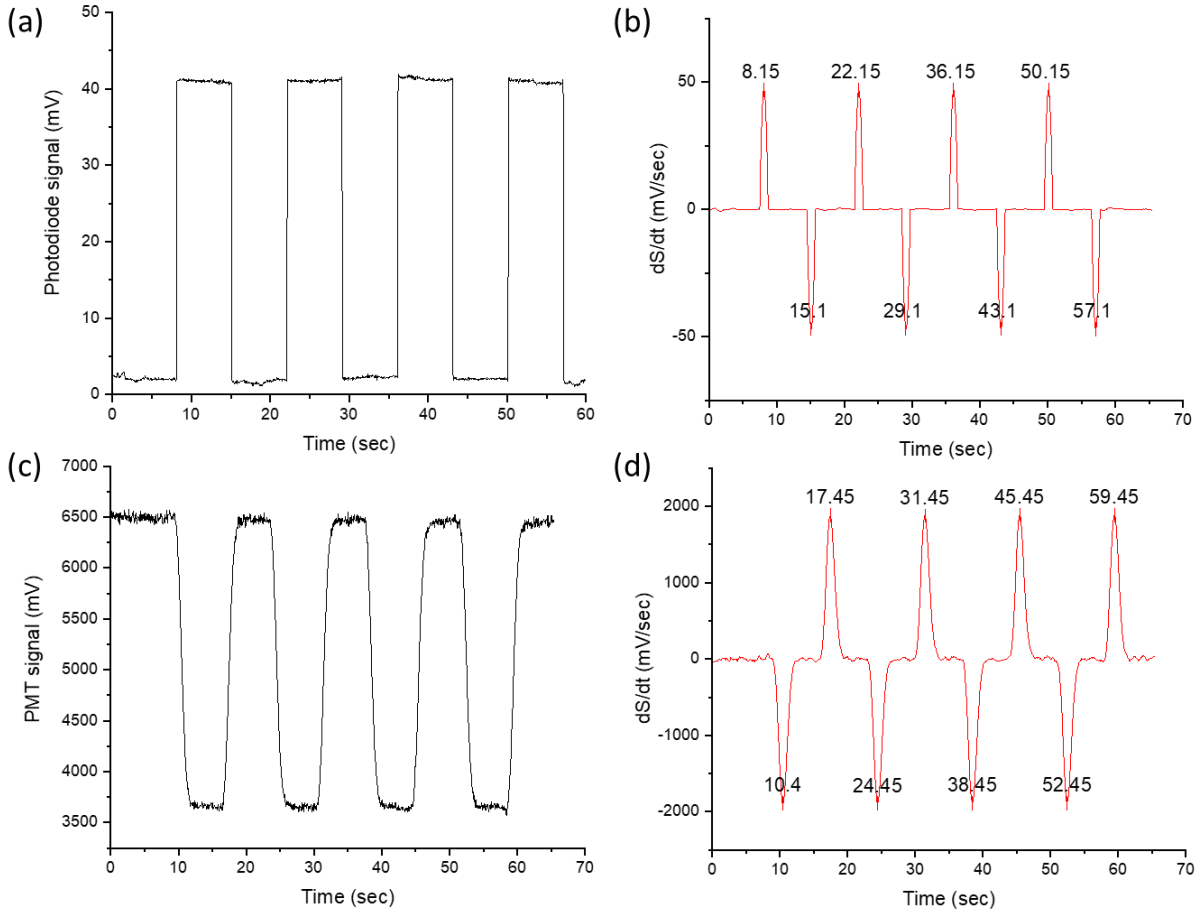

Figure 2.7: Four images illustrating the time of flight measurement of flow velocity: (a) photodiode signal from a high intensity chopped laser beam that was used to photobleach the dye solution (b) differentiated photodiode signal used to highlight the edges of the photobleached spot, (c) fluorescence signal measured at the detection zone by PMT downstream of bleaching

spot, (d) differentiated PMT signal used to highlight edges of the rising and falling fluorescence signals due to the photobleached plugs.

The columns used for velocity measurements in this study are cylindrical shapes. The flow profile is parabolic across the width of the column according to the Hagen–Poiseuille equation, having the velocity maximum at the center [40]. Hence, the laser detection spots were focused (to ~20 μm spot in the x-y plane) within the center of the column (97.5 μm I.D.). Photobleaching cycles were started once the flow velocity reached a steady-state indicated by the stable fluorescence signal. The frequency of the chopper was adjusted during measurements so that there was enough time for both unbleached and bleached plugs of dye signal to establish their stable baseline (Figure 2.8).

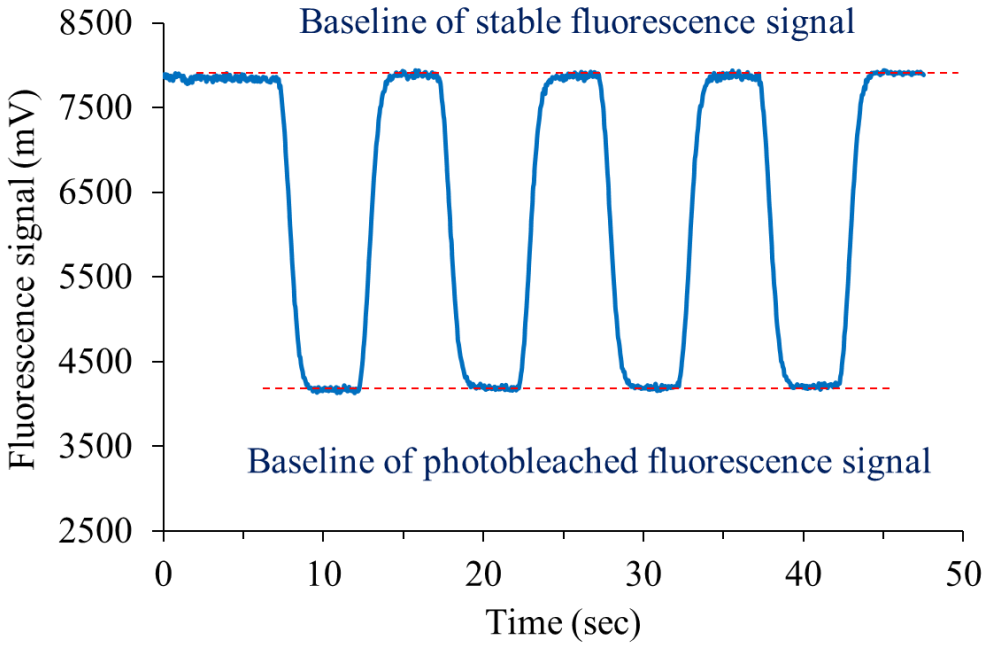

Figure 2.8: Fluorescence signal with stable baselines for both unbleached and bleached plugs.

Initially, we were using nitrogen gas for pressurizing liquid. However, during higher pressure (>2000 psi) measurements with nitrogen, often unstable and false square wave fluorescence signals were observed. Nitrogen gas at higher pressure can become saturated (solubility 0.017 g gas/ kg water at 25°C) in water. When the pressure of liquid drops after leaving the porous bed, dissolved nitrogen gas in water generates bubbles within the liquid dye stream. These bubbles travelling to the detector give rise to a false square wave signal. In contrast, inert helium gas has ~10 times lower solubility in water compared to nitrogen gas (Figure 2.9) [76]. That is why, in place of nitrogen gas, we performed many of our flow experiments using helium gas.

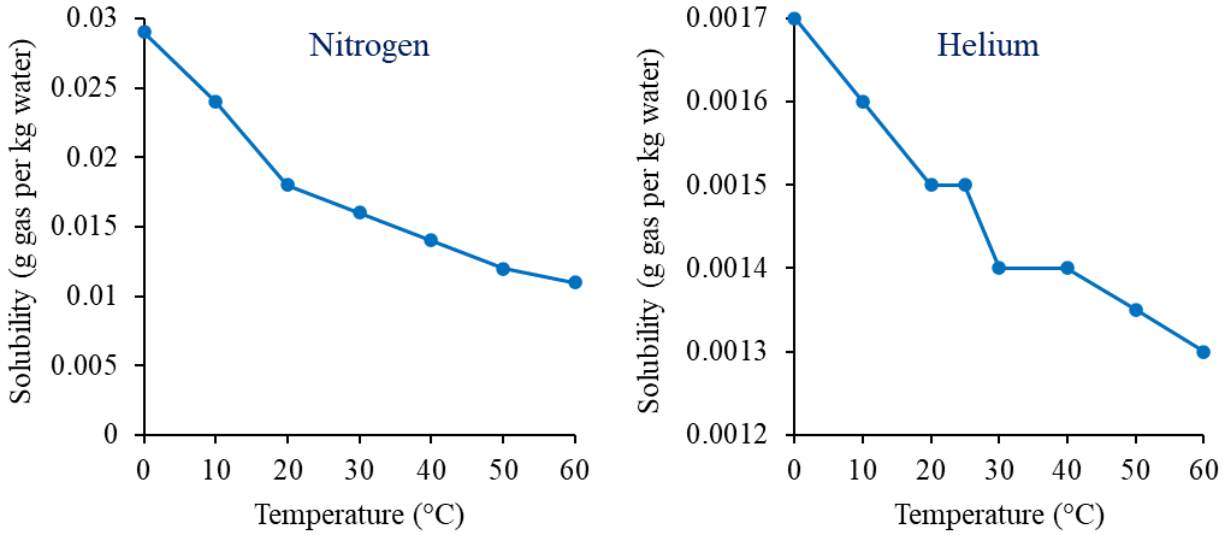

Figure 2.9: Solubility of N_2 and He gases in water [76] (graphs were reproduced from https://www.engineeringtoolbox.com/gases-solubility-water-d_1148.html).

Optimization of the detection point upstream versus downstream of the column and on the packed bed was evaluated to get the optimal signal intensity of edges of the photobleached region to ease velocity calculations. Even though the upstream detection gives very sharp falling and rising fluorescence signals (Figure 2.10), it was not considered for the velocity measurement since bleached photoproducts may block the pores in the porous media, causing variation in actual flow properties.

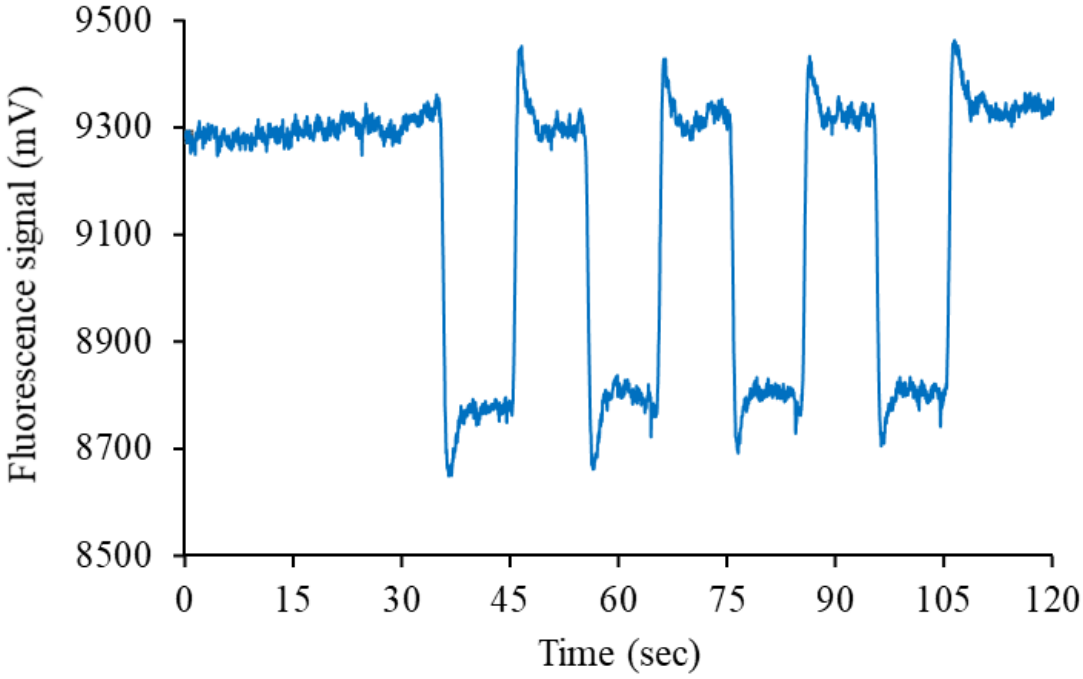

Figure 2.10: Fluorescence signal from the upstream detection of the porous bed.

On the other hand, detection directly on the column created distorted and broad fluorescence signals due to diffusional mixing of bleached and unbleached dye solution plugs and scattering from packed particles (Figure 2.11). Moreover, the base fluorescence signal of dye molecules also reduced after a few photobleaching cycles, which indicates that flow velocity started to drop due to the hindrance from the photoproducts generated within the pores of the column. The laser beam used for the fluorescence detection also bleaches the dye molecules, so as the flow rate decreases, there is more time for bleaching under the detector laser, which thus reduces the base fluorescence signal intensity.

Compared to upstream and on-column detection, downstream detection generates a more stable fluorescence signal (shown in Figure 2.8).

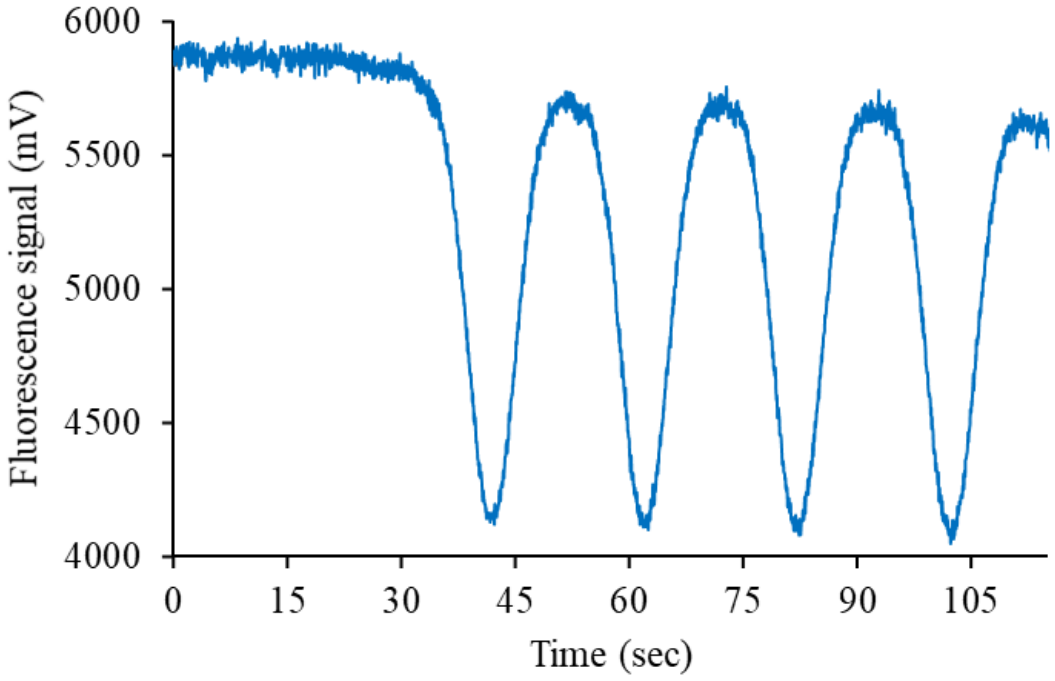

Figure 2.11: Fluorescence signal from the detection spot on the porous bed.

2.3.3 Evaluation of the measured velocity

When the bleaching laser beam is focused on the dye solution stream flowing through the cylindrical fluidic channel, a bleached dye plug is created within the liquid stream. As the bleached plug moves along the channel, it stretches along the axial direction due to advection processes. The coupling of radial and axial dispersion arising from diffusion, and axial dispersion arising from the parabolic flow velocity profile, are known as the Taylor-Aris dispersion process (as shown in Figure 2.12) [77]. Taylor-Aris dispersion arises from molecular diffusion across the

laminae associated with laminar flow, wherein a parabolic flow profile causes a sample plug to travel at different rates depending on the location with the cylinder.

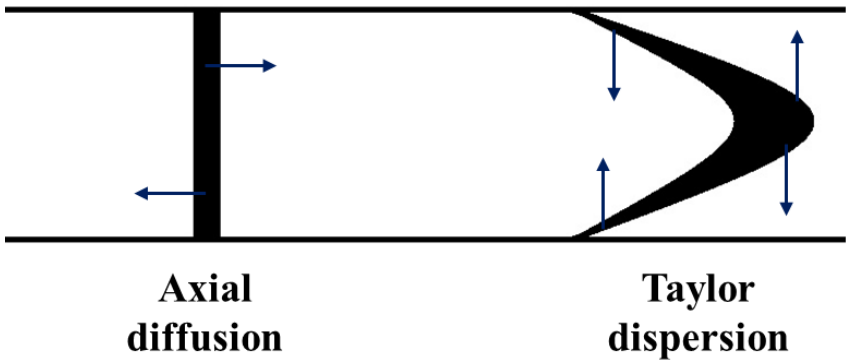

Figure 2.12: Taylor-Aris dispersion in an open capillary column, where arrows indicate the diffusive sample movement.

The question arises as to the meaning of the velocity measured with the time of flight technique employed in this thesis. In the case of liquid flow in a cylindrical tube, the Hagen-Pousielle equation (shown below) estimates the expected volumetric flow rate (Q) as a function of applied pressure drop.

$$Q = \frac{\Delta P \pi R^4}{8 \eta L} \quad \text{(1.4)}$$

where:

ΔP is the pressure difference between the two ends of the tube,

L is the length of the tube,

η is the dynamic viscosity of the liquid of interest,

Q is the volumetric flow rate through the tube,

R is the radius of the tube.

The volumetric flow rate (Q) can be linked to the average flow rate (v_{ave}) by $v_{ave} = Q/\pi R^2$. In the absence of dispersion during flow, the time of flight measurement would return v_{ave}, as determined from the above expression. However, the dispersion may cause an error in the measured velocity and cause it to differ from v_{ave} as defined for the Hagen-Pousielle equation. The discussion below evaluates this potential error.

The Taylor-Aris dispersion in a cylindrical flow leads to an effective diffusion parameter (D_{eff}) that can be much greater than the molecular diffusion coefficient ($D_{diffusion}$). The value of D_{eff} for a laminar flow in a cylindrical tube is given by equation 2.2 [77, 78] –

$$D_{eff} = D_{diffusion}\left(1+\frac{Pe^2}{48}\right) \quad \text{.....(2.2)}$$

where the Peclet number (Pe) is defined as $Pe = Rv_{ave}/D_{diffusion}$ [77]. The diffusion coefficient ($D_{diffusion}$) value of sodium difluorescein salt dye in water [79, 80] is 0.42×10^{-5} cm^2/s, which was used for the calculation of theoretical plug dispersions discussed below.

In the frame of the moving sample plug along the axial direction z, given by $\xi = z - v_{ave}t$, the dispersion of the plug is given by the following classic diffusion expression of the form of Fick's Laws [77, 81]:

$$\frac{\partial c_{ave}}{\partial t} = D_{eff}\frac{\partial^2 c_{ave}}{\partial \xi^2} \quad \text{.....(2.3)}$$

where c_{ave} is the cross-sectional average of dye solution concentration. In the cylindrical tube, starting from a plug of finite width (h) with sharp radial edges, the solution to this dispersion problem is written in the following form [81]:

$$C = \frac{1}{2}C_o\left\{\operatorname{erf}\frac{\frac{h}{2}-z}{2\sqrt{D_{eff}t}} + \operatorname{erf}\frac{\frac{h}{2}+z}{2\sqrt{D_{eff}t}}\right\} \quad \text{.....(2.4)}$$

where:

z is the axial distance in the tube,

C_o is the original dye concentration (before bleaching starts), which is proportionally equal to the difference between maximum (I_{max}) and minimum (I_{min}) fluorescence signal intensities (as shown in Figure 2.13(A)),

C is the new concentration at a distance z and time t,

h is the dye plug width.

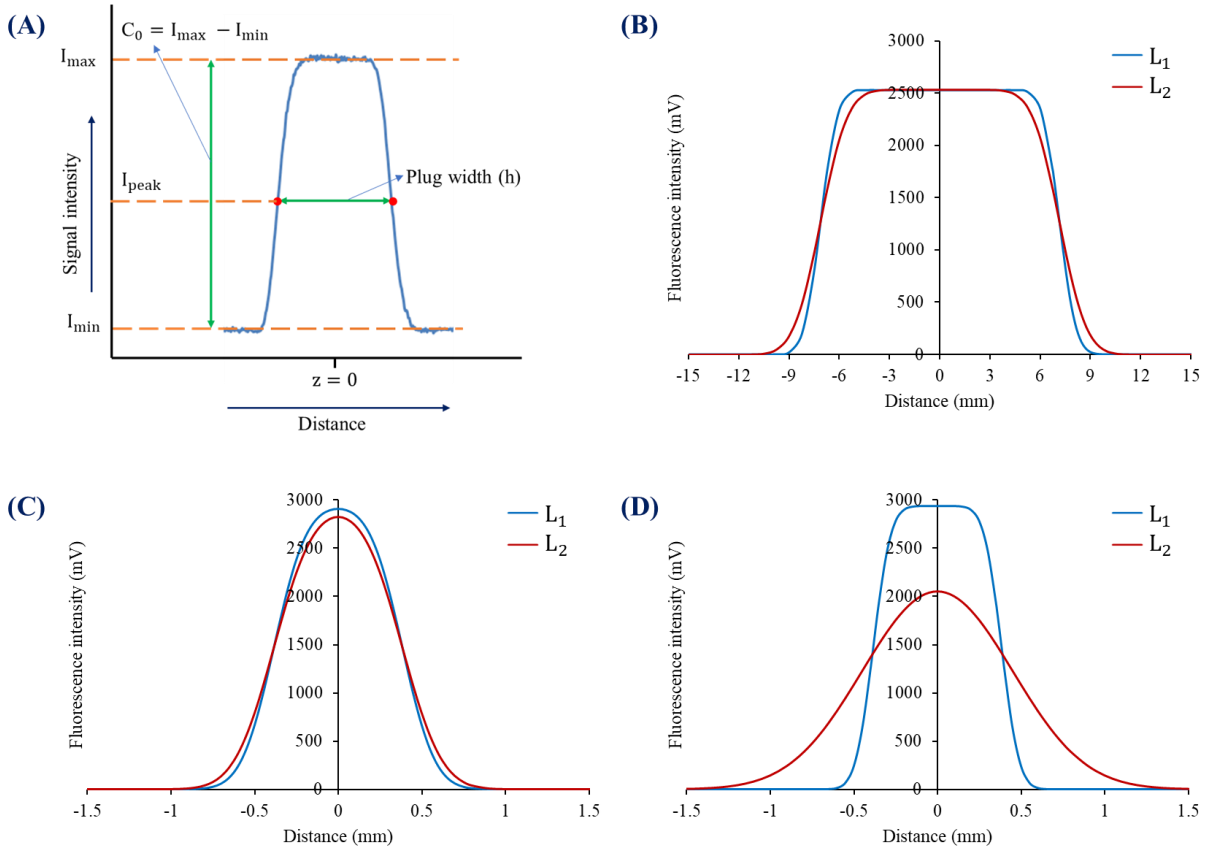

Figure 2.13: A schematic graph of signal change in the frame of a dye plug moving with the average linear velocity, where the signal intensity (or dye concentration) is the maximum at z = 0 distance (A). The theoretical plug dispersions were calculated for one of the fastest porous bed columns having 171.4 mm/min velocity (B). Figures (C) and (D) show the dispersion results calculated for the same bed having 2.9 mm/min velocity, but Figure (D) shows a calculation where L_1 is located much closer to the bleaching zone (5 seconds away) with a much more exaggerated delay time (95 seconds) between point L_1 and L_2.

Analysis of typical data sets for our slowest and fastest porous bed confirms that the peak observed in the derivative trace of the fluorescence signal lies at an average of 50% intensity on

the rising or falling edge curves, within ±2% from peak to peak. Table 2.1 gives some typical values for the position of the derivative peak for data obtained from a slow and a fast porous bed column. The data itself is presented and analyzed in Chapters 3 and 6. The importance of this result is that it shows the observed velocity represents the ratio of distance and transit time between plug cycles. The manner in which the 50 % intensity point varies with dispersion is then critical to interpreting the observed velocity.

Table 2.1: Signal intensity (%) at the peak of highest derivatives relative to the maximum signal intensity at two detection spots (L_1 and L_2) in a slow and a fast porous bed. The relative signal intensity at the peak was calculated according to the equation: Intensity $(\%)= \frac{(I_{max} - I_{peak})}{I_{max} - I_{min}} \times 100\%$; where I_{peak} is the intensity at the peak of the highest derivative.

	A slow column (for 25.2 mm/min velocity)		**A fast column (for 171.4 mm/min velocity)**	
	Peak intensity (%) at L_1	**Peak intensity (%) at L_2**	**Peak intensity (%) at L_1**	**Peak intensity (%) at L_2**
Falling signal	47.43	52.97	47.47	45.13
Rising signal	50.90	46.16	58.83	57.39
Falling signal	48.19	49.15	54.34	45.22
Rising signal	50.73	49.17	46.98	56.40
Falling signal	48.04	50.98	58.90	43.50
Rising signal	51.25	49.05	49.64	53.48

Figure 2.13(B) shows a plot of calculated plug dispersion for conditions appropriate to one of the fastest beds tested. The dispersion trace at the time associated with measuring at L_2 overlays the dispersion trace that would be observed at L_1. For rapid flow, Figure 2.13(B) indicates the 50% fluorescence point is translated downstream and lies at the same distance from the centre of the plug at L_2 as at L_1. Calculations using equation 2.4 for very small increments of distance confirm there is no shift in the relative location of the 50% point. As a result, we can safely conclude that at relatively high flow velocities, and short dispersion times, the velocity obtained experimentally is the average velocity required for the Hagen-Pousielle equation. These conditions apply to the vast majority of data we collected.

Figure 2.13(C) shows the dispersion results calculated for one of the slowest beds evaluated, while Figure 2.13(D) shows the same bed, but calculated for L_1 located much closer to the bleaching zone (5 s away), with a much more exaggerated delay time (95 s) between point L_1 and L_2. (That is, a much slower velocity and greater dispersion.) Figure 2.13(D) makes it clear that at some point, the approximation that the difference between 50% fluorescence intensity points accurately reflects the plug profile in the absence of dispersion is no longer valid. However, Figure 2.13(C) shows that the approximation is still very good even for the slowest packed bed studied. Calculations using equation 2.4 for very small increments of distance confirm that there is a small shift (~2%) in the relative location of the 50% point, leading to at most a 2% overestimate in the velocity. Under the same conditions, the experimental error in velocity measurement is ±1.5% standard deviation. Consequently, even for the slowest packed beds, the velocity observed can be treated as the average velocity predicted by the Hagen-Pousielle

equation. In fact, as a general rule of thumb, so long as the central region of the bleached and unbleached plugs continues to reflect the magnitudes observed in the absence of photobleaching, the approximation that the method measures the average volumetric flow rate and linear velocity is reasonable.

To achieve the greatest accuracy in velocity measurements, the dispersed shape of the dye concentration plug arising from Taylor-Aris dispersion needs to be fully developed and relaxed at both detection spots. Moreover, the uncertainties may arise from variations (e.g. optical distortion by the curved cylinder walls) in the sizes and positions of the bleaching and detection laser spots, the bleaching response time, etc. Therefore, measuring travel time at only one detection spot may not provide us with accurate velocity measurement. The dual-point velocity measurement technique improves accuracy by measuring travel times at two different locations that are precisely defined by the translation stage micrometer, and taking their difference (t_2-t_1). Any systematic error originating from differences in the bleaching and detection laser spot focus, will be the same at both detection spots and will be cancelled out. Thus, dual-point velocity measurement using the equation, $v= \frac{L_2-L_1}{t_2-t_1}$, gives us a greater precision of velocity measurements. We observe that the travel times from both rising and falling edges can show a few tenths of a second difference over the 4-24 second time period of multiple bleached plugs. Averaging the velocities obtained from four bleached plugs, using both leading and tailing edge time differences, improves the reliability and repeatability of the velocity values measured.

2.4. Conclusion

Each cycle of chopped photobleaching laser produces a new data point for the time of fluid travel. Therefore, it is possible to measure several cycles of velocity data for a constant pressure flow and then check the precision of the data. Moreover, two parallel photobleaching experiments at two different spots were used for each velocity measurement to decrease the inaccuracy caused by the size of the bleaching and detection spots and the bleaching reaction time. Thus, the dual-point velocity measurement technique generates reproducible results, which would be helpful to get high-quality data sets for porous media flow.

Chapter 3: Micro and Nano Porous Media

3.1. Introduction

To study fluid dynamics in micro and nano scale, building a micro- and nanofluidic channel system structure is essential. There have been reports of flow measurements through micron-sized flow restrictors within microfluidic flow networks [71] and membranes of aligned carbon nanotubes having diameters of 7 nm [28] and less than 2 nanometers [55]. However, these straight flow channels are not totally well suited to predicting the flow properties in the tortuous path existent in porous media. In addition, a fluid experiences a high amount of friction in porous media flow, requiring a comparatively higher pressure gradient for flow. Hence, the study of porous media flow in micro-and nanofluidic scales requires the fabrication of a robust porous media which could remain mechanically stable in the high flow pressure environment, and chemically inactive to fluids.

The three-dimensional structure of the pore network created in the interstitial spaces of assembled nanoparticles makes colloidal self-assembly (CSA) of nanoparticles an attractive choice as a porous media. In colloidal self-assembly (CSA), monodispersed micron and nanometer-sized particles assemble into three-dimensional, periodic nanostructures [63]. The micron or nano-sized pores formed by the well-organized nanoparticles interconnect together to generate a micro- or nanofluidic porous structure. There are several reports of using CSA as a sieve structure in separation science. CSA of nanoparticles was utilized to form a nano-porous

stationary phase as a separation matrix in a microfluidic channel, especially for separations of proteins [63-65] and DNA [63]. Wirth et al. packed C4 alkyl chain coated silica particles of different sizes into the capillary column, studied the flow velocities variation for different pore sizes [26], and showed its impact on separation efficiency [15, 82]. This research has applied a colloidal self-assembly approach to fabricate porous media in a capillary tube instead of PDMS microfluidic chips.

To mimic the condition of low permeable oil and gas reservoirs and normal phase high-pressure liquid chromatography, we aimed to develop micro- and nano-porous media suitable to test fluid flow from low to very high pressure. The use of fused silica capillary tubes benefits from withstanding the high pressure compared to PDMS microfluidic chip. Therefore, silica particles are packed inside the fused silica microcapillary tube; where the silica bed acts as micro- or nano-porous media, while an empty capillary tube models a microchannel (75 μm). The interconnected pores among the silica particles act as the micro or nanochannels for fluid flow.

3.2. Experimental

3.2.1 Fabrication of porous media

Figure 3.1-3.3 illustrates the process of fabricating a packed bed of porous media in a fused silica capillary tube. An aqueous suspension (10 % w/v) of non-porous silica microsphere particles (690 nm from Poly Sciences Inc. or 1000 nm from Bangs Laboratories Inc.) without any chemical treatment or modification was used for fabricating the packed column. First, the silica

suspension was dispersed by vortex mixing followed by sonication for half an hour to form a uniform colloidal solution of silica microspheres.

An empty fused silica capillary tube of 75 μm internal diameter was cut into the desired length of 10-15 cm and dried by blowing nitrogen gas (10-15 psi) through it. Then, one end of the capillary tube was immersed vertically into the reservoir of silica colloidal solution. By capillary action, the silica colloidal solution wicked into the empty capillary tube. The tube was immediately removed from the silica solution once it was filled about one-third of its length.

(A)

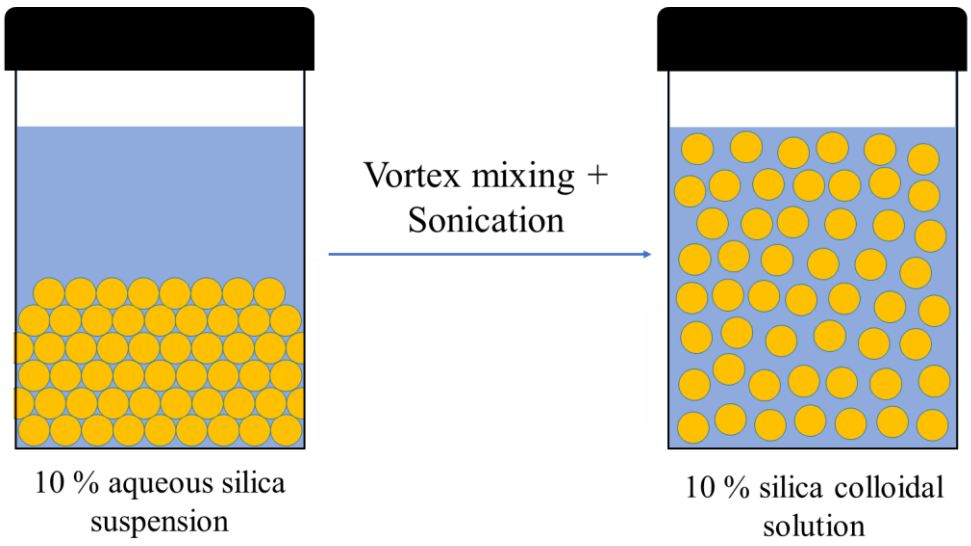

Figure 3.1: The process of fabricating a packed bed of porous media: (A) Dispersion of colloidal solution of silica microspheres by vortex mixing and sonication.

(B)

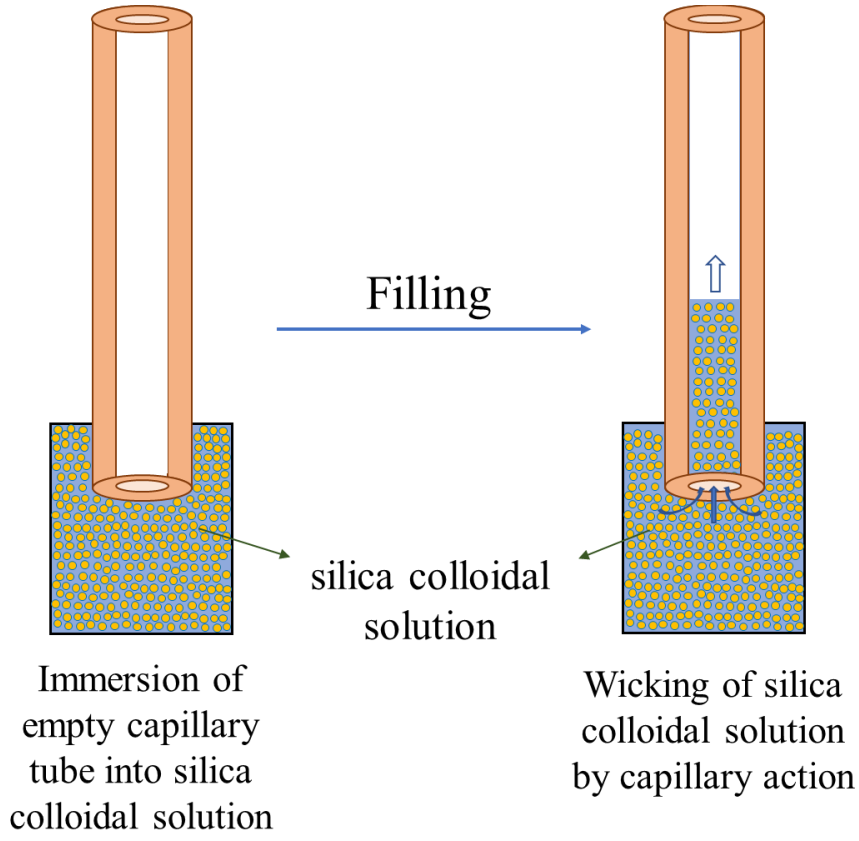

Figure 3.2: The process of fabricating a packed bed of porous media *(continued)*: (B) Capillary filling of colloidal solution into the empty tube.

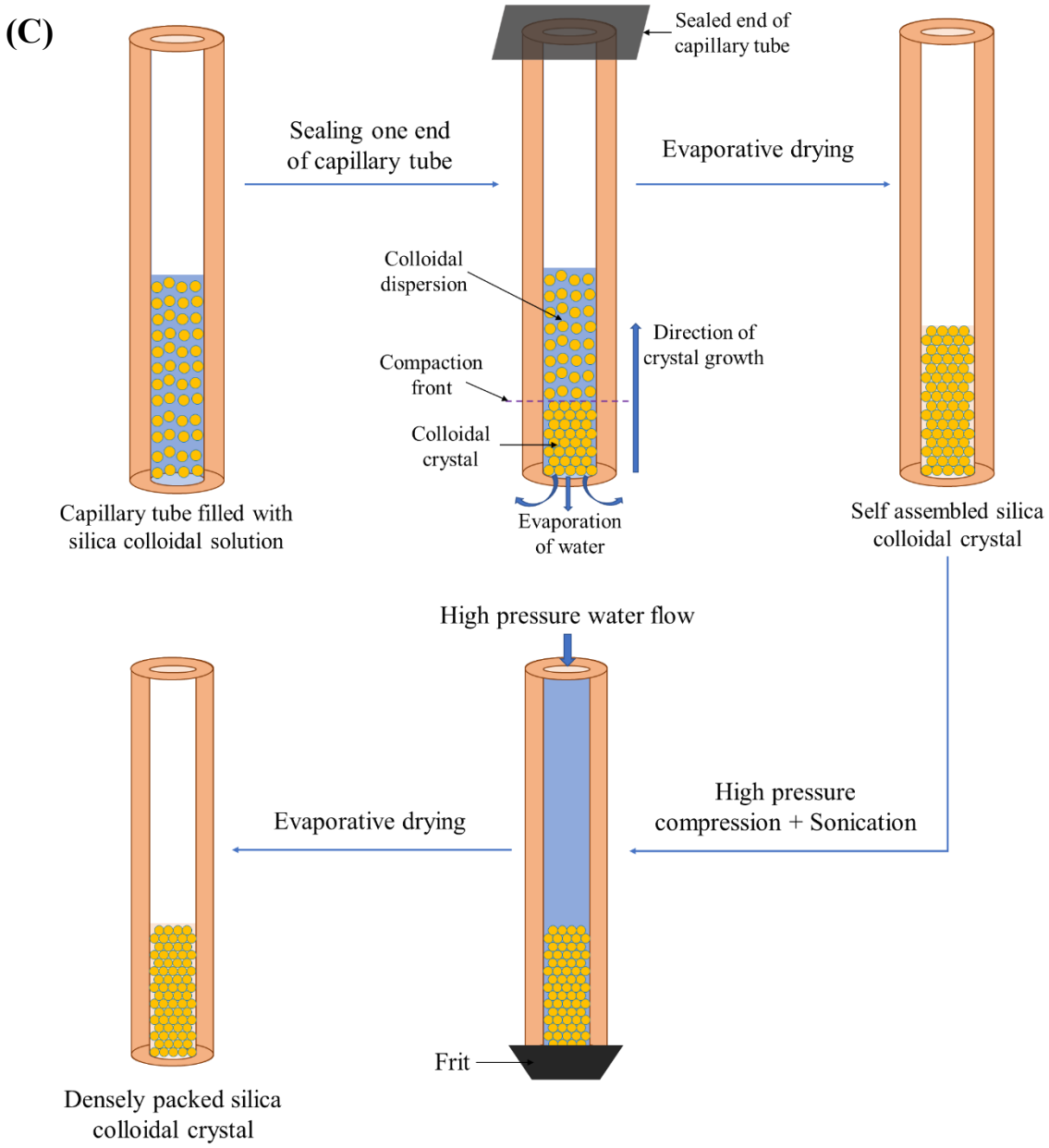

Figure 3.3: The process of fabricating a packed bed of porous media (continued): (C) Formation of self-assembled silica colloidal crystal by evaporative drying. Later, a more densely packed bed is formed by simultaneous sonication and high-pressure flow compression followed by evaporation.

Then, an evaporation-induced colloidal self-assembly mechanism was used for forming a packed bed of silica microspheres. The empty end of the capillary tube was sealed while the silica solution-filled end of the tube was kept open for evaporation. Moreover, this open end of the tube was kept vertically down to allow gravity settling of silica particles along with evaporation.

Once the silica colloidal crystal was formed, the packed end of the capillary tube was coupled with a frit. Then, a nanoflow of water under simultaneous sonication was applied through the packed column. Initially, the flow rate of water was kept low and then gradually increased. Each specific flow rate was maintained for a few minutes, until the column backpressure raised to a stable value. Once the backpressure of the column reached 5000 psi, the flow of water and sonication were stopped. The column was kept connected to the nanoflow pump until the backpressure decreased to less than 50 psi. Then, the packed column was disengaged from the pump. The water-filled end of the column was sealed again to allow evaporation from the packed end. Thus, a densely packed silica colloidal crystal was developed inside the fused silica capillary tube.

3.2.2 Characterization of porous media

Determination of Porosity:

Five separate columns of porous media were prepared by packing nonporous silica microspheres of the same size (1000 nm diameter) inside fused silica capillary tubes. Then, water was flowed through these packed columns at different pressures. The linear flow velocity of water

was determined by following the time of flight photobleaching velocity measurement technique (described in Chapter 2). Here, the capillary tube used as the detection column had an internal diameter of 75 μm (same as the packed column), which was the only modification made to the instrument setup described in Chapter 2. Then, the flow velocity (vη) normalized with fluid viscosity was plotted against the pressure gradient (ΔP/L) applied. This graph was then fitted to the Kozeny-Carman equation (3.1) by linear regression, to calculate the porosity (ε) of the porous silica bed.

$$\frac{Q}{A} = \frac{d_{particle}{}^2 \varepsilon^3 \Delta P}{180\eta(1-\varepsilon)^2 L} \quad \text{.....(1.6)}$$

Or,

$$v\eta = \frac{d_{particle}{}^2 \varepsilon^3}{180(1-\varepsilon)^2}\left(\frac{\Delta P}{L}\right) \quad \text{.....(3.1)}$$

where,

Q is the volumetric flow rate,

A is the cross-sectional area of the packed bed,

v is the average linear flow velocity,

η is the dynamic viscosity of the fluid,

$d_{particle}$ is the diameter of silica microspheres used in a packed bed,

ΔP is the applied pressure for fluid flow, and

L is the length of the porous bed.

Here the slope of the curve obtained from the $v\eta$ versus $\Delta P/L$ is equal to $\frac{d_{particle}{}^2\varepsilon^3}{180(1-\varepsilon)^2}$, which yields a cubic polynomial equation. Instead of solving this equation, we determined the value of porosity (ε) by an iterative solution, selecting values of ε until we obtained the observed value of slope ($\frac{d_{particle}{}^2\varepsilon^3}{180(1-\varepsilon)^2}$). The standard method of error propagation requires a solution to the above equation. Instead, we added and subtracted the slope error to the absolute slope value to obtain the higher and lower extreme values of the slope. Then, we applied the same iterative method to determine ε for these ranges of slope, providing the highest and lowest extreme values of ε. Then, the difference between these two values, divided by two, gives us an estimate of the standard deviation, or error ($\Delta\varepsilon$) in porosity. This approach likely gives a slight overestimate in the error, but will be relatively close to the correct value. This method was also followed in the following Chapters (4, 5 and 6) to calculate the absolute value (ε) of porosity and its error ($\Delta\varepsilon$).

Figure 3.4 illustrates a schematic drawing of a packed bed with the notations of the variables used in the Kozeny-Carman equation. Since water is a wetting fluid to silica, a no-slip boundary condition was assumed here for the water flow through silica porous media.

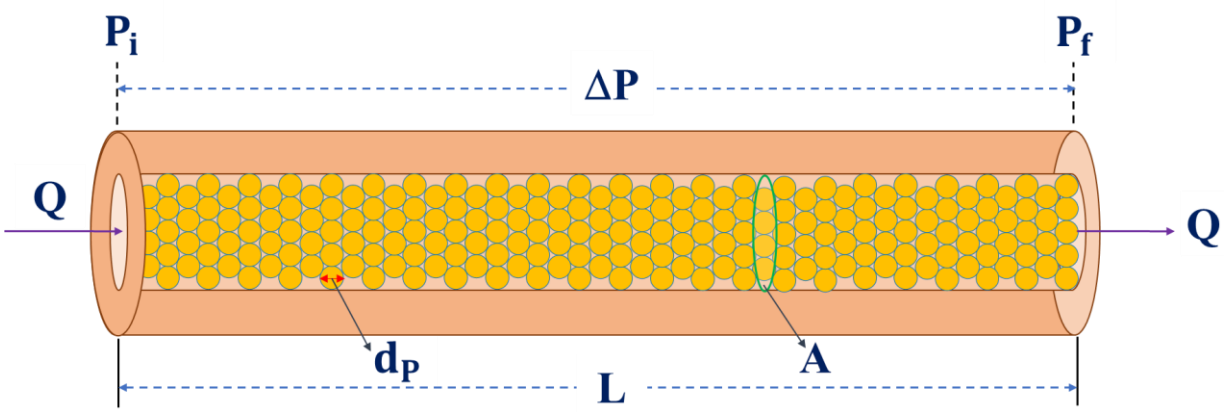

Figure 3.4: A schematic drawing of a packed bed.

Alternative approach of determining bed porosity:

The porosity of the packed bed was also measured by the water evaporation method. First, the packed column was filled and saturated with water by flowing water through it. Then, the weight of the water-saturated column was measured in a weighing balance having 0.01 mg accuracy. Additionally, the temperature of the water during the weight measurements was also recorded. Later, the packed column was air-dried for seven days. Then, it was kept in an oven at 60°C for one hour, followed by a desiccator connected to a vacuum to ensure complete water evaporation. Finally, the weight of the packed column was again measured. Figure 3.5 illustrates the volume dimensions of the dry and water-filled packed column.

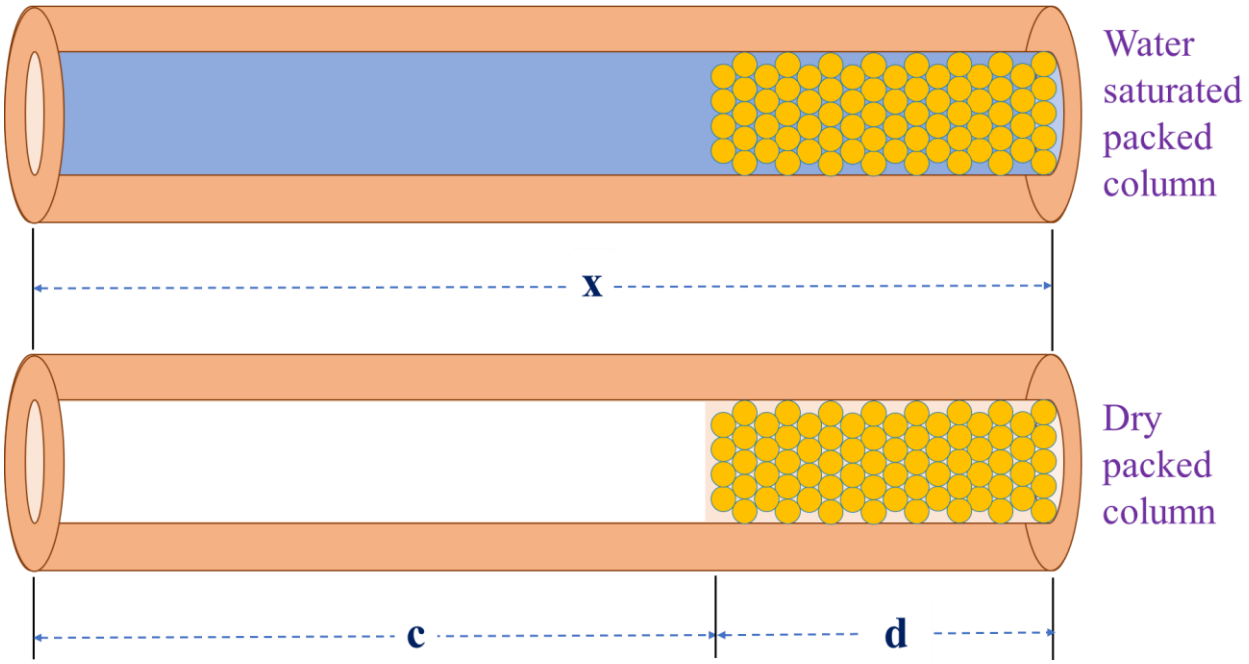

Figure 3.5: Volume dimensions of the dry and water-saturated packed columns.

The volume of water contained in the total length of the capillary tube, i.e., total void space (x) in the tube, was calculated with the following equation (3.2):

$$x = \frac{Wet_{wt} - Dry_{wt}}{\rho_{H_2O}} \quad \text{.....(3.2)}$$

where,

Wet_{wt} is the weight of the packed column filled with water

Dry_{wt} is the weight of the dry-packed bed

ρ_{H_2O} is the density of water.

The length of the packed porous bed and the whole capillary column were also measured by using a micrometer installed on a translational stage equipped with an inverted microscope. Then, the porosity (ε) of the porous bed was calculated according to the following equation (3.3):

$$\varepsilon = \frac{(x-c)}{d} \times 100\% \quad \ldots\ldots\ldots\ldots\ldots\ldots\ldots\ldots\ldots\ldots\ldots\ldots \quad (3.3)$$

where,

c is the volume of water in the empty part of the capillary tube

(x-c) is the volume of water available in the packed bed, i.e., the pore volume

d is the total volume of the packed bed

Determination of Permeability:

The Darcy equation (1.5) was used to determine the permeability (k) of the porous bed:

$$\frac{Q}{A} = v = \frac{-k\Delta P}{\eta L} \ldots\ldots\ldots\ldots\ldots\ldots\ldots\ldots\ldots\ldots\ldots\ldots\ldots (1.5)$$

where,

Q is the volumetric flow rate,

A is the cross-sectional area of the packed bed,

v is the average linear flow velocity through the packed bed,

k the permeability of a porous bed,

η is the dynamic viscosity of the fluid,

ΔP is the applied pressure for fluid flow, and

L is the length of the porous bed.

The same data set obtained from the pressure-driven water flow experiments to determine the porosity of the packed columns was utilized to measure these columns' permeability values. First, the flow velocity ($v\eta$) normalized with fluid viscosity was plotted against the pressure gradient ($\Delta P/L$) applied. Then, the graph was fitted to the Darcy equation (3.4) by linear regression to calculate the permeability (k) of the silica porous bed, considering the no-slip boundary condition for the water flow through silica porous media.

$$v\eta = -k\left(\frac{\Delta P}{L}\right) \quad \text{.....(3.4)}$$

Scanning electron microscopy and imaging:

The packing order of silica microspheres in the packed column was evaluated from the images of the porous bed taken by scanning electron microscopy (SEM). Optically focused images of the packed columns in the presence of light were also captured to identify any trace of crystalline closed packing structure formed in the porous bed resulting in Bragg diffraction.

3.3. Theory

The rationale for using no-slip boundary condition for water flow in silica porous bed:

The packed bed formed with the silica microspheres consists of micro- or nano-sized voids in its structure, creating an interconnected pore network to form a single porous bed. The porosity of the porous bed determines the average diameter of a single pore formed within the network. The theoretical pore diameter (d_{pore}) of a single pore within a porous bed with respect to porosity (ε) and particle diameter ($d_{particle}$) can be calculated using equation 3.5 [83].

$$d_{pore} = \frac{2\varepsilon d_{particle}}{3(1-\varepsilon)} \quad \text{.....(3.5)}$$

For a porous bed formed from equal spheres, the porosity value ranges from 0.26 for the densest packing to 0.36 for a random packing. Table 3.1 shows the single pore size expected within the range of porosity values (0.26-0.36) of a porous bed. Thus, the smallest pore that can be formed within the porous bed of 1000 nm silica microspheres is about 234 nm.

Table 3.1: The variation of pore diameter to porosity values in a porous bed formed with 1000 nm silica microspheres.

Porosity (ε)	**Pore diameter (d_{pore})**
0.26	234
0.28	259
0.30	286
0.32	314
0.34	343
0.36	375

Keliu Wu et al. [84] drew a summary about the dependence of flow enhancement to pore diameter and wettability of fluid in a porous bed, as shown in Figure 3.6. As water is a wetting fluid to the silica surface, the contact angle is expected to be less than 90°. Hence, assuming a

no-slip boundary condition for water flow in a silica porous bed with a pore diameter of more than 200 nm is reasonable.

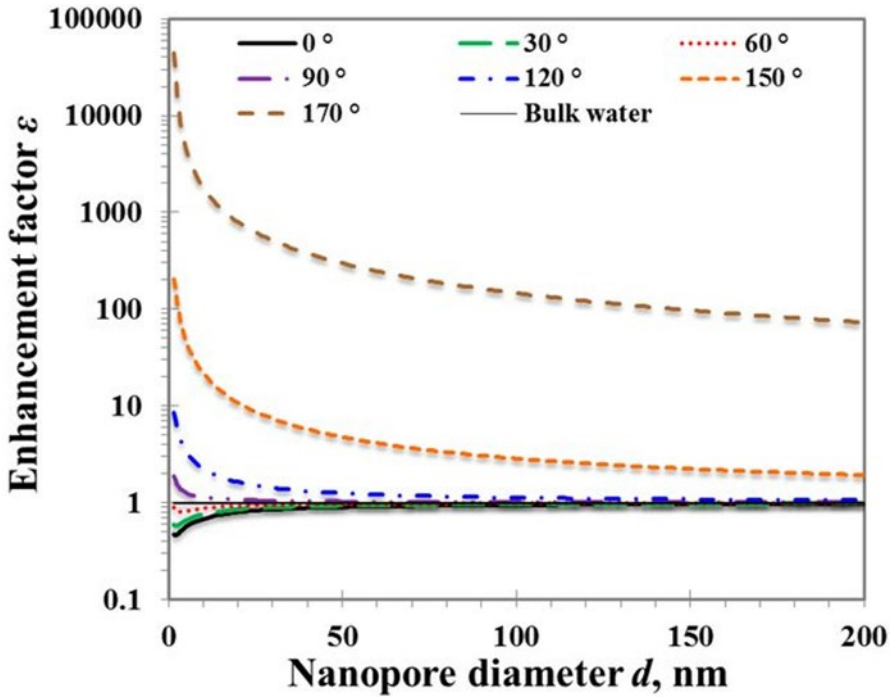

Figure 3.6: The dependence of water flow enhancement factor to pore diameter for various wettability in a porous media*. Reprinted from the literature with permission [85].

*This plot was produced based on the combination of theoretical analysis and experimental and MD simulations data found in the literature, i.e., it does not truly represent experimental data [84, 85]. Keliu Wu et al. [84] stated, “In summary, we have investigated the flow of water confined in nanopores with different wettability and dimensions by the combination of a theoretical analysis and data from MD simulations and experiments in the literature.” .

3.4. Results and discussion

Self-assembled silica colloidal crystal:

The aqueous silica colloidal solution wets the hydrophilic glass surface of the fused silica capillary tube and fills the microchannel, producing a vapour-liquid interface at the end tube. Figure 3.7 illustrates that when the other end of the tube is sealed, evaporation starts at the drying edge interface initiating the nucleation of continuous assembling of silica microspheres in the opposite direction of the column.

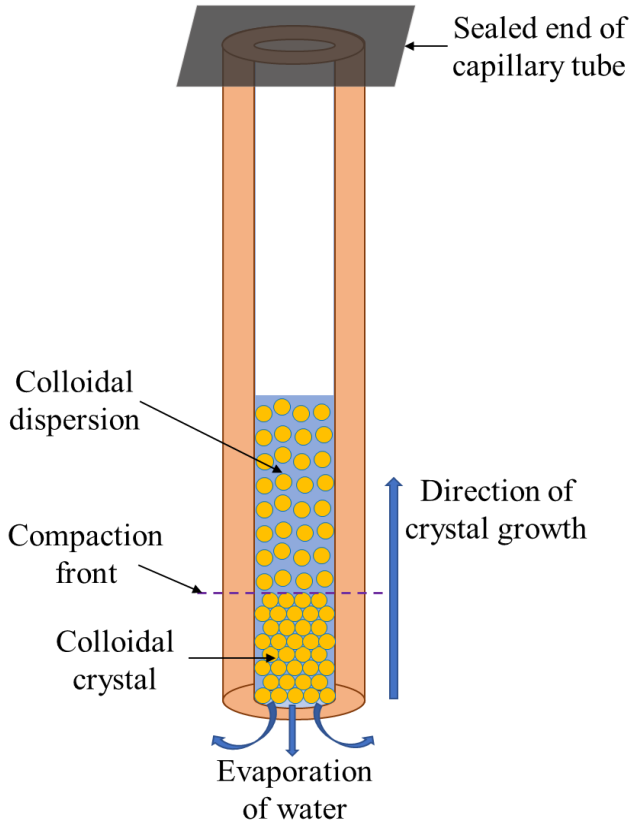

Figure 3.7: A schematic of self-assembled silica colloidal crystal formation inside a microchannel of a capillary tube.

While water evaporates during the assembly process, strong hydrophilic interaction keeps the surface of the particles wet and forms nano-menisci among the microspheres at the column outlet interface. The capillary tension of the nano-menisci draws water through the porous packed zone keeping the particles wet during assembly. Thus, the air-water interface remains fixed at the first packed layer of microspheres, preventing any air invasion during particle assembly. Initially, the fluid flow through the compact region and the evaporation rate at the drying edge remains constant. However, as the packing continues, the hydrodynamic resistance to water flow

increases within the packed region. The low water flow rate can trigger air invasion into the colloidal assembly that can eventually cause stress-induced cracking while the packed porous bed dries [63, 86, 87], so humidity conditions may require control..

During the assembly process, the columns were kept in a humid condition. SEM images of the ambient air-dried, and humidity-managed, dried packed columns are shown in Figure 3.8 and 3.9, comparing the quality of packing with respect to the drying condition. A close-up of the packed beds illustrates that porous beds formed in humid conditions have the closed packed arrangement of the silica microspheres. Figure 3.9 (b) illustrates the long-range order of particles over the three-dimensional structure, with no large cracks when dried in a humid environment. The presence of extra moisture in the vicinity of the packing column during the assembly and drying process slows down the rate of water evaporation and prolongs the drying duration. As a result, particles have sufficient time to rest themselves in a thermodynamically stable position, which prevents the formation of any drying-caused crack in the packed bed. Therefore, in contrast to the air-drying method, the drying under a humid condition was a comparatively better approach to obtaining reproducibly ordered packing structure.

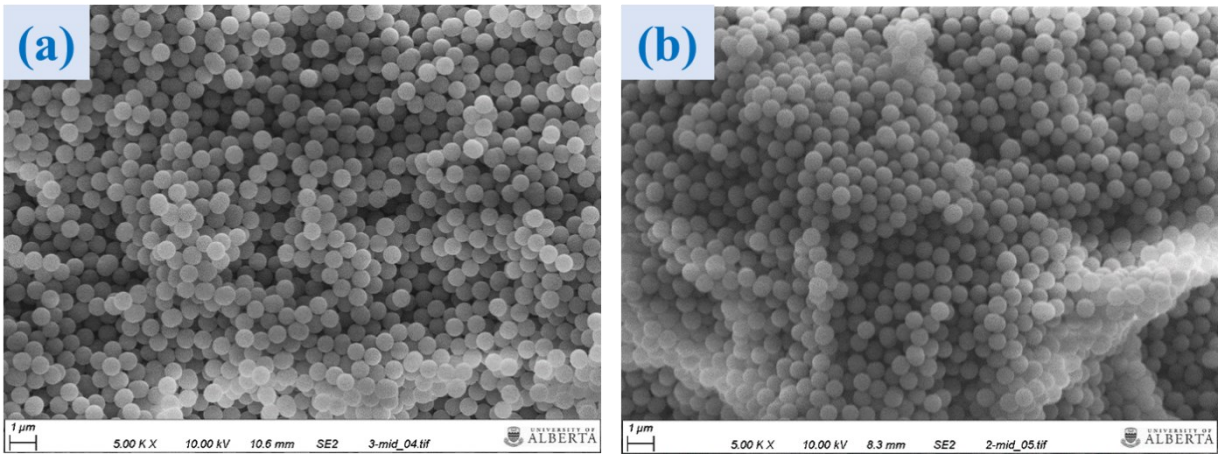

Figure 3.8: Packing morphology in the cross-section of the packed bed column after drying in (a) air and (b) humid conditions.

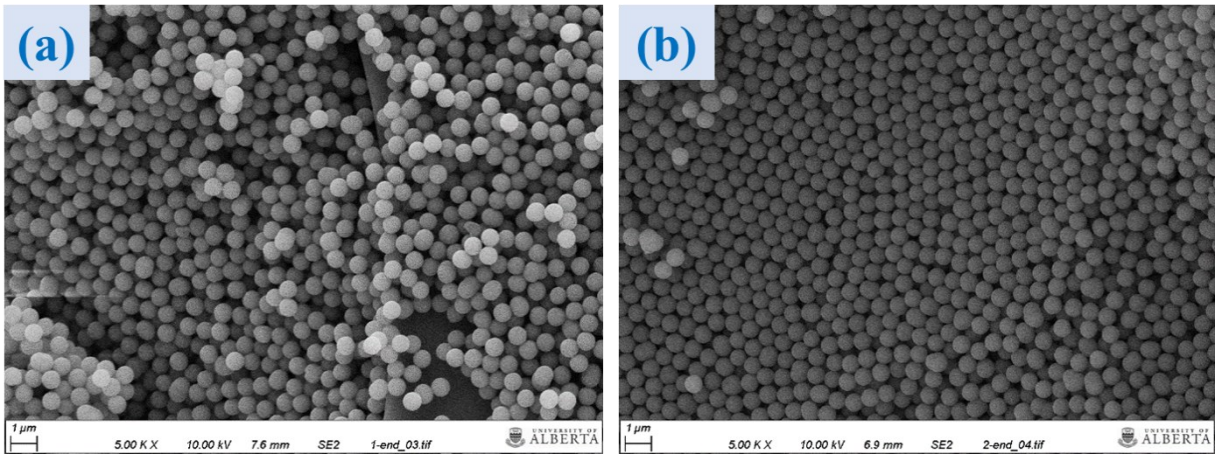

Figure 3.9: Packing morphology at the end of the packed bed column after drying in (a) air and (b) humid conditions.

The quality of packing in the porous bed:

The SEM image taken from the packed bed of 690 nm silica microspheres, shown in Figure 3.10, illustrates the presence of vacancies and interstitial defects in the porous bed structure.

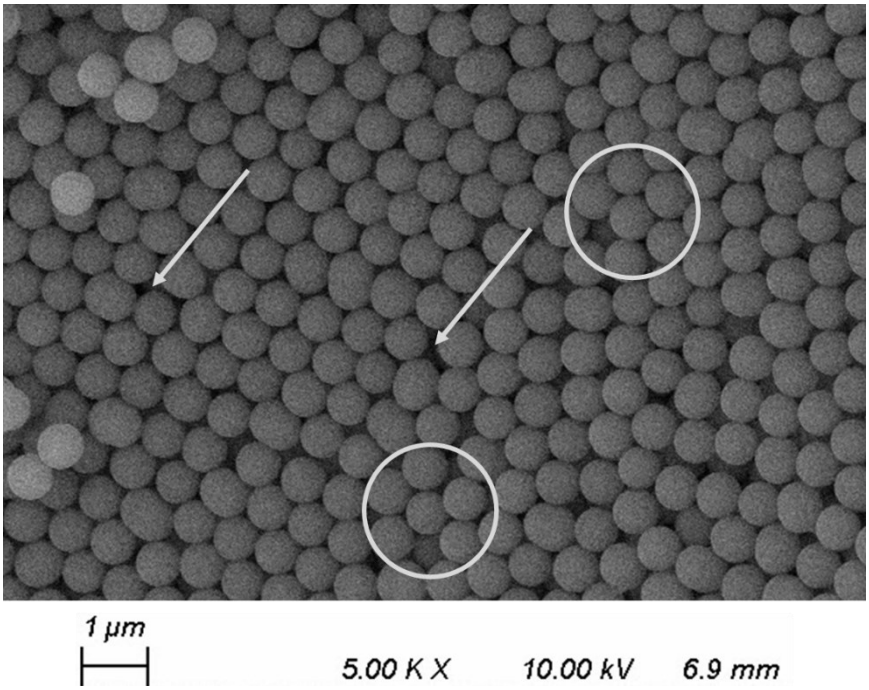

Figure 3.10: SEM image of self-assembled 690 nm silica microspheres. The arrows and circles indicate the presence of interstitial defects and vacancies, respectively.

Figure 3.11 shows that although micro- and macro-scale cracks are present at the tip of the column, no such cracks were found in the packed bed's inner structure. As cracks can generate macro-scale flow, which is unwanted for micro- and nanoflow studies, the formation of cracks was prevented by keeping the columns in a wetted condition.

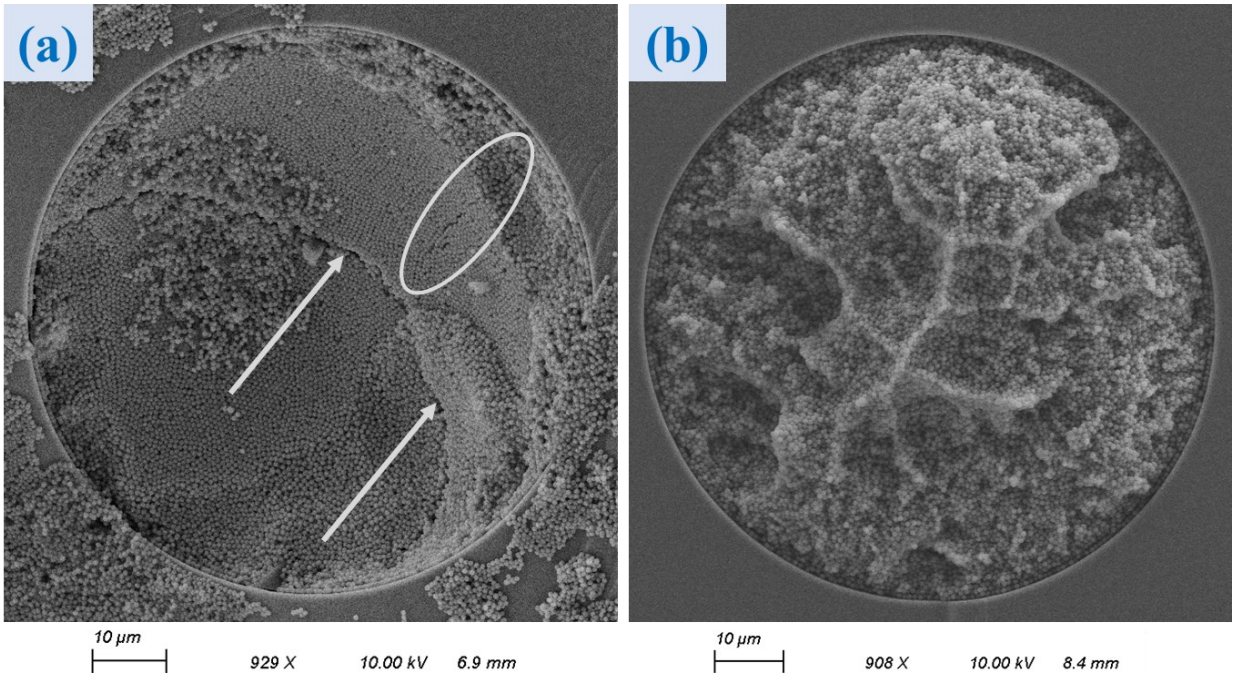

Figure 3.11: SEM image of the packed bed taken from the tip of the column (a) and the cross-section after cutting at the middle of the bed (b). The oval shape and arrows indicate the presence of micro and macro-sized cracks.

The size variation of the silica microspheres, which is noticeable from the SEM image shown in Figure 3.10, causes the formation of a large number of interstitial defects and vacancies in the closed-packed structure of the porous bed. The manufacturer-defined sizes of the commercial particles used for packing are 690 ± 40 nm and 1000 ± 50 nm (obtained from Poly Sciences Inc. and Bangs Laboratories Inc., respectively), with about 13% polydispersity in particle size. However, less than a 2% CV of particle size is necessary to maintain high fidelity long-range order and minimize defect formation [88, 89]. Still, we could produce porous beds of high-quality packing, with only the modest disorder seen in Figures 3.9(b), 3-10 and 3.11(a) by

carefully controlling drying and crystal growth rate. Figure 3.12 shows that when the packed column was illuminated with light, the porous bed showed multicolour due to Bragg diffraction, which is indicative of the presence of high order of packing.

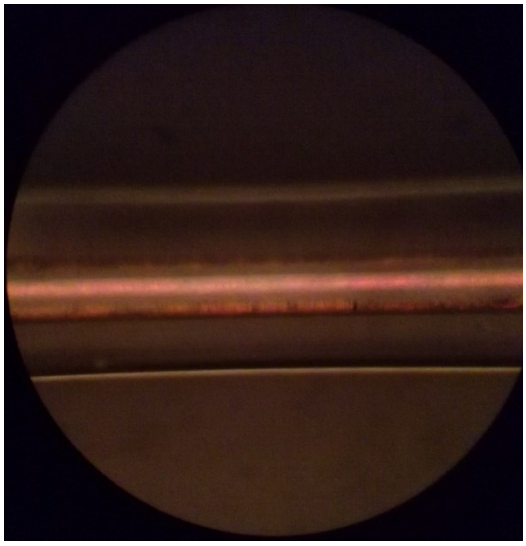

Figure 3.12: Colour because of Bragg diffraction indicates the high order of packing.

Porosity-permeability relationship in the porous bed:

The linear flow velocity of water in five different columns packed with 1000 nm silica microspheres was measured with respect to different amounts of applied pressures. Figure 3.13 shows the dependence of flow velocity on the applied pressure gradient. The Y-axis represents velocity multiplied by the solvent's viscosity at the experimental temperature. The x-axis represents pressure gradient, which means actual applied pressure divided by the total length of the packed bed. The actual pressure drop was calculated by taking the difference between the applied pressure and the cumulative pressure drops from frit, empty capillary, and restrictor columns (the details about the pressure correction have been discussed in Chapters 4 and 5). A

very low standard deviation (less than 1 mm.mPa.sec/min or <3% RSD) of the flow velocity data collected from the three measurement trials was observed at any specific pressure gradient. Furthermore, each packed column showed a linear relationship (R^2 = ~1) between normalized velocity and pressure gradient throughout the applied pressure range (maximum up to ~2100 psi). The above results indicate the reproducibility and accuracy of the velocity measurement technique used in this research and the stability of the packed beds in the applied conditions during measurements.

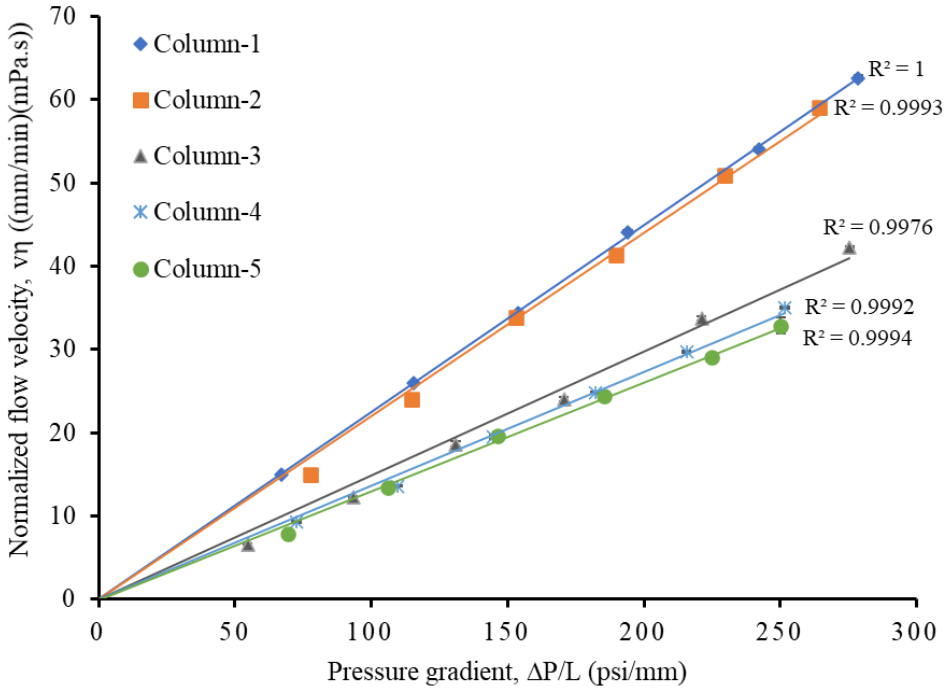

Figure 3.13: The variation of flow velocity with respect to the applied pressure gradient in porous beds packed with 1-micron silica microspheres. Each data point is the average of three measurements, and the bars represent the standard deviation. Note: Here most of the error bars are not visible as they are smaller than the symbols used to express the data.

The porosity and permeability values calculated according to the Kozeny-Carman and Darcy equation, respectively, from the slope of the linear curves, are listed in Table 3.2. Theoretically, the porosity of the body-centred cubic closed packing (BCC) is 32%, and that of the hexagonal (HCP) or face-centred cubic (FCP) closed packing is 26%. Here, columns 3, 4 and 5 show lower porosity, around 31%; i.e., the packing order in these columns resembles mostly body-centred cubic closed packing. Alternatively, it could be a mixture of each structure, having mostly BCC. The porosity values of the porous beds measured using the water evaporation method are a fairly close match (within ±5% error) with the velocity-pressure determined values, as shown in Table 3.2.

Table 3.2: The calculated values of porosity and permeability of the porous beds.

Porous beds	**Porosity (calculated from graph)**	**Porosity (measured by water evaporation method)**	**Permeability (mD)**
Column-5	0.305 ± 0.001	0.313 ± 0.006	0.319 ± 0.006
Column-4	0.306 ± 0.001	0.314 ± 0.002	0.334 ± 0.003
Column-3	0.313 ± 0.001	0.321 ± 0.011	0.365 ± 0.004
Column-2	0.344 ± 0.001	0.327 ± 0.014	0.538 ± 0.005
Column-1	0.345 ± 0.001	0.332 ± 0.009	0.550 ± 0.003

The measured permeability values in the millidarcy (mD) range are very close to that of unconventional oil reservoirs [21, 90]. Furthermore, a power-law relationship between the

respective porosity and permeability values was found, as shown in Figure 3.14, consistent with Archie's power-law model (equation 3.6) [91, 92].

Archie's power-law model: $k = a.\varepsilon^{b}$ …...……...……(3.6)

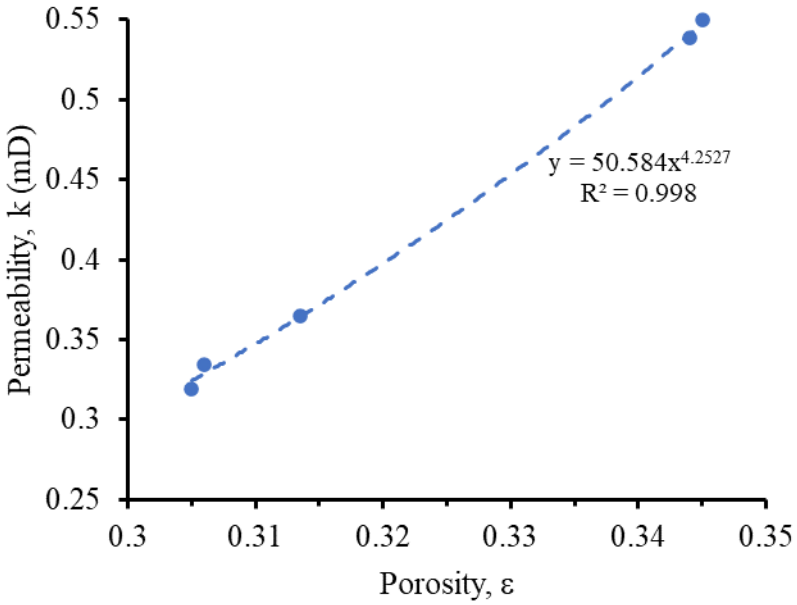

Figure 3.14: The dependence of permeability to porosity.

Berg [93] also developed a power law equation for systematic packing of perfect spheres by plotting the ratio of permeability and square of particle diameter versus the porosity of the packed bed in the range of 30 to 40 percent porosities and derived the following relationship (equation 3.7); Berg's equation for permeability given perfect packing of uniform spheres:

$$\frac{k}{d_p^2} = 5.1 \times 10^{-6}.\varepsilon^{5.1} \text{……...…… (3.7)}$$

where k is expressed in Darcy's, porosity is expressed in percent, and particle diameter is expressed in mm. Berg's equation ($k/d_p^2 = 5.1 \times 10^{-6}.\varepsilon^{5.1}$) was obtained from a curve fit through two theoretically obtained "data" points, based on the tetrahedral ($\varepsilon = 0.3019$) and orthorhombic ($\varepsilon = 0.3954$) packings for uniform spheres.

The porosity values from our columns packed with 1-micron diameter silica particles are within 0.30 to 0.35, which is within the range of Berg's model. We compare the predictions of the Berg model to our observed permeabilities in Table 3.3. The experimentally obtained permeability values are about 1.5-1.7 times higher than Berg's predictions, i.e., there is some disagreement between our experimental observations and Berg's theoretical model.

Table 3.3: Comparison between the experimental and Berg's estimates of k/d_p^2 (darcy/mm^2) with respect to columns' porosity (%).

Porosity (%)	k/d_p^2 (darcy/mm^2) [Experimental measure]	k/d_p^2 (darcy/mm^2) [According to Berg's estimate]	Ratio between experimental and Berg's k/d_p^2 estimates
30.5	319	189	1.68
30.6	334	193	1.73
31.4	365	220	1.66
34.4	538	350	1.54
34.5	550	355	1.55

The discrepancy between our observed data and the theory of Berg may arise from several possibilities. The first is the approximations involved in the Berg model. The model was obtained by fitting only tetrahedral and orthorhombic packing. In Figure 2 of Berg's publication, it can clearly be seen that if cubic packing had been included as well, the slope of the log plot would have been less steep, leading to a smaller exponential factor. Work presented in 2008 at the SPE Eastern Regional/AAPG Eastern Section Joint Meeting (Pittsburgh, Pennsylvania, USA), by Siddiqui et al. [92], and also discussed in the thesis by that author [94], includes theoretical "data" points for the above three packings and for the densest, rhombohedral packing as well (ε = 0.2595). Both the pre-exponential and the exponential factor varied considerably depending on the data points fit, and on if the fit was forced to use Berg's exponential factor of 5.1. The best choice of the pre-exponential and exponential factors in the power law for small pore sizes remains unclear without sufficient experimental data.

Another possible reason for the deviation in our observations relative to Berg's predictions could be that none of the columns prepared in this work have perfect geometric packing, or that defects are present that have an impact. The proximity of the porosity values of packed beds to that of tetrahedral packing indicates that tetrahedral packing is more abundant within any mixture of packing orders. On the other hand, the variation in permeability between several 1 μm diameter bead packed columns, is indicative of multiple different packing structures within the bed, or some defects impacting permeability.

Berg's publication compares the model to experimental data obtained with relatively large grains (0.25 to 2 mm) compared to the work presented here (1000 nm here, and smaller still in later chapters). That work observed reasonable agreement (within ~10 %) with experimental data for large particles. However, the pores in the interstitial space between particles were approximated by rectilinear geometries, which leave the regions near the particle surfaces unaccounted for and lead to lower permeability. At a smaller pore scale, the impact of this approximation will become more prominent and may account for discrepancies between the Berg model and experimental observations of permeability. While the ratio of these regions will not scale with particle size, the extent of communication by diffusion between these regions will increase considerably for smaller pore sizes, as will the impact of surface chemistry.

The Berg model has been extensively referenced over time, but the risk of decreased accuracy in extrapolating a power-law relationship points to the need for experimental data in the small pore size range. Berg [93] mentioned in his own paper, "The theoretical development presented here is approximate, and limited in application. In its present form the derived equation cannot be expected to provide a basis for engineering calculations. It can only be regarded as an initial step toward a deeper insight into the relationship between permeability and the primary properties of reservoir rocks.".

3.5. Conclusion

The five porous bed columns packed with identical particles were prepared at different times following the same method. Still, a slight variation of timing in any fabrication step can

result in the packing of variable porosities that we observed here, although it was not intentionally done. Therefore, to minimize this variability, the packed beds used in the later chapters were developed by the same fabrication process maintaining a uniform condition of fabrication steps. Moreover, we have measured the porosity value of a porous bed assuming no-slip condition for water flow, and then used that observed porosity for evaluating the expected flow behaviour of other liquids, relative to the observed flow rate. In this way, we normalized for any possible defects, because we can expect defects will affect flow behaviour of all the solvents in the same way.

Chapter 4: Slip and No-Slip Flow in Porous Media

4.1. Introduction

Fluids can experience zero or non-zero flow velocity at the wall depending on their wettability with fluidic channel material. It was reported that the flow of polar solvents, e.g., water and acetonitrile, through a reversed-phase liquid chromatographic (RPLC) column, having a non-polar hydrocarbon chain coated porous bed, did not follow the no-slip boundary condition [14, 15]. On the other hand, a non-polar solvent, e.g., toluene, showed no-slip behaviour in the same column. The use of smaller packing particles in an ultra-high performance liquid chromatography (UHPLC) column is a strategy to improve separation efficiency [95]. However, it requires a very high-pressure input. Bingchuan et al. demonstrated that slip flow in the RPLC system facilitates the separation of proteins more efficiently, requiring less pressure input than expected [82].

In normal-phase liquid chromatography (NPLC), silica is usually used as the stationary phase; and non-polar solvents are used as the mobile phase [96]. Therefore, to better improve the separation efficiency in an ultra-high performance normal-phase liquid chromatography column, it is necessary to investigate how fluid dynamics for a non-polar liquid works in a silica micro and nanoporous system. Wang et al. reported a theoretical molecular dynamics study of octane flow through a quartz nanoporous system having 1.7 - 11.2 nm pores [20]. However, the transport of n-octane in a silica nanoporous system is still experimentally unexplored to our knowledge.

Therefore, we aimed to study the pore-scale transport phenomena of non-wetting (n-octane) and wetting (water) fluids in a silica porous media.

4.2. Experimental

4.2.1 Materials

An aqueous suspension (10 % w/v) of non-porous silica microsphere particles (1000 nm, Bangs Laboratories Inc.) was used for fabricating the packed column. A fused silica capillary tube (TSP075375, Polymicro Technologies, Molex) was used to pack silica microspheres inside to prepare a porous bed. Nile red (Millipore Sigma) and fluorescein disodium salt (Sigma, St. Louis, MO) were used as fluorescence tracing dyes. Ultrapure water and n-octane (Millipore Sigma) were used as the solvents for preparing fluorescein disodium salt and nile red dye solutions, respectively. O_2 gas (Praxair, Mississauga, ON, Canada) was used to prepare a photo-bleachable oxygen-saturated dye solution. Helium gas (>99.998% purity, Praxair Canada Inc., Mississauga) was used for pressurizing dye solutions to get a constant pressure liquid flow.

4.2.2 Fabrication of packed porous bed

Figure 4.1(a) illustrates the process of fabricating a packed porous bed (described in detail in Chapter 3). First, a colloidal dispersion (10 % w/v) of non-porous silica microspheres (1000 nm diameter; Bangs Laboratories Inc.) was wicked into an empty fused silica capillary tube (73.5 μm internal diameter, 360 μm outer diameter) by capillary action. Then, an evaporation-induced colloidal self-assembly mechanism was used for forming a packed bed of silica microspheres.

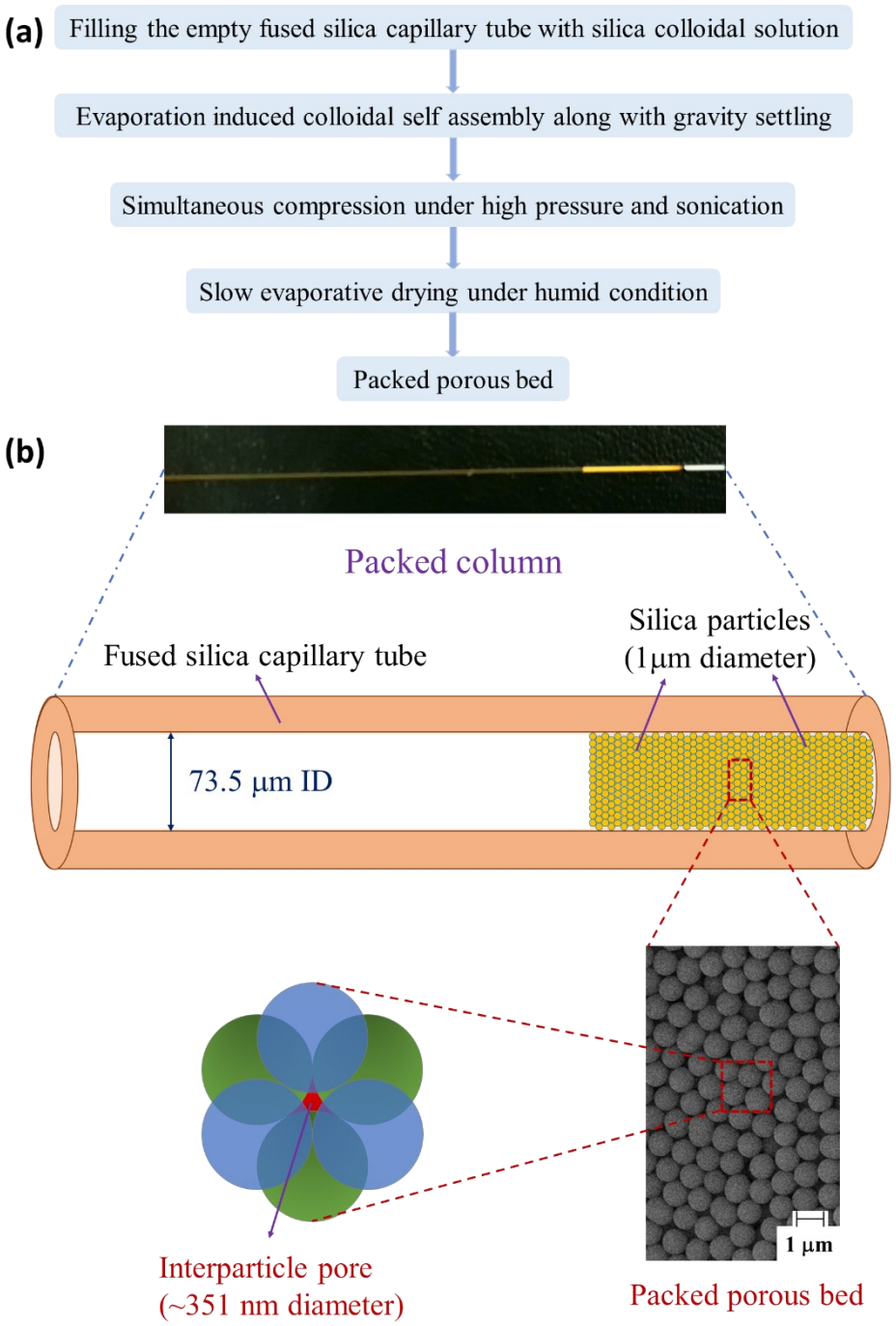

Figure 4.1: (a) The steps of fabricating a packed column of porous media. (b) A photograph of a packed porous bed, including an illustration.

The empty end of the capillary tube was kept sealed, to allow evaporation from the silica solution-filled open-end, facilitating self-assembly of silica microspheres in the opposite direction. In addition, the open end of the tube was also kept vertically down to allow gravity-induced settling of silica particles. Once the silica colloidal crystal is formed inside the capillary tube, sonication and high-pressure water flow were simultaneously applied for more compaction of the bed of silica particles. Then the column was dried with a slow evaporation process, by keeping the column in a water vapour abundant environment, to get a densely packed and crack-free porous media. Figure 4.1(b) shows a photograph of a porous bed with an illustration of an interparticle pore (~351 nm diameter) created through the packing of silica microspheres (1 μm diameter) inside a fused silica capillary (73.5 μm internal diameter) tube.

4.2.3 Instrumentation

Figure 4.2 illustrates the complete instrument setup for the flow experiments. The instrument setup used here was kept the same as that described in Chapters 2, except the capillary tubes used for packing and detection purposes had a different internal diameter (73.5 μm in this case), and the restrictor (10 μm I.D. column) was 15 cm long. A constant pressure pump system was utilized. A gas cylinder (helium) and regulator were used to pressurize helium gas which was then delivered to a container of dye solution to pressurize the fluid, and liquid flows from the fluid container by a tube located deep within the fluid. A pressure transducer was used to monitor the pressure drop across the device relative to the atmosphere. A frit with a 0.5-micrometre pore was used to support the packed porous bed keeping it stable and stationary inside the capillary. Then, the packed column was coupled with an empty capillary having the same internal diameter

(73.5 µm), which was then again coupled with another empty capillary having a smaller internal diameter (10 µm). This 10 µm internal diameter column was used as a restrictor to avoid forming bubbles within the liquid stream.

Two 488 nm Ar ion lasers and a variety of lenses were used for photobleaching and fluorescence detection. One laser operated at high intensity was focused to photobleach the dye inside the empty capillary. A chopper was used to generate a square wave dye concentration variation by alternately directing the laser beam between the capillary and a photodiode. The second laser was used for laser-induced fluorescence detection.

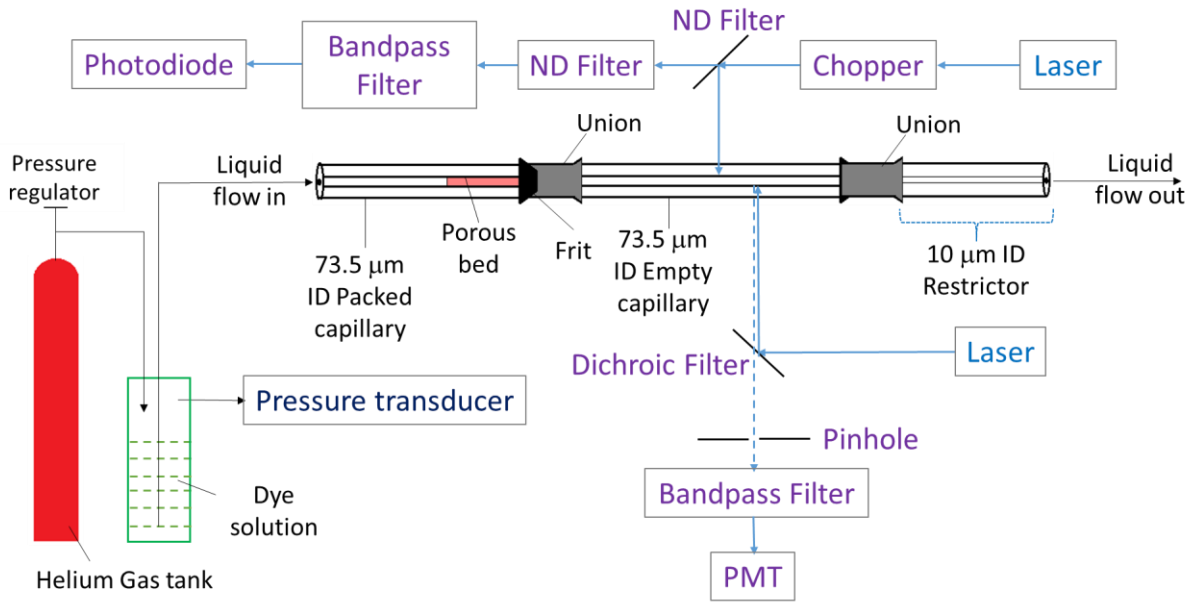

Figure 4.2: A diagram of complete instrument setup used in the time of flight, photobleaching velocity measurements. The fluidic unit consists of constant pressure pumping unit connected to

a porous packed bed and velocity detection column. The optical unit consists of two laser sources, various lenses, and filters for photobleaching and fluorescence detection.

4.2.4 Determination of linear flow velocity

A time-of-flight photo-bleaching velocity measurement technique (described in detail in Chapter 2) was used here. 190 nM fluorescein disodium salt (dissolved in ultrapure water) and 150 nM nile red (dissolved in n-octane) dye solutions were used in the flow measurements with water and n-octane solvents, respectively. A dye solution flowing through the porous bed at constant pressure was photo-bleached downstream by a chopper-modulated high-intensity laser beam to generate a square wave dye concentration variation. The time of flight of the photo-bleached plug was then determined at two different detection zones downstream of the bleaching site. The fluorescence signal was measured first 1-3 mm away from the bleaching point, and the time of flight from the bleached spot was determined for about five pulse periods. The detector was then translated 1 mm away from the first detection point to repeat the time-of-flight measurements. Then, the velocity (v) was determined according to the equation, $v= \frac{L_2-L_1}{t_2-t_1}$. Here, t_1 and t_2 correspond to the times required for the bleached dye plug to reach the first (L_1) and second (L_2) detection zones, respectively. Then, the average linear velocity was calculated.

4.2.5 Characterization of porous media and its flow properties

First, the length of the porous bed was measured using a micrometre translation stage, while viewing under a microscope. Then, the column of the porous bed was attached to the fluidic unit for the pressure-driven flow measurements. A 190 nM aqueous fluorescein solution was

flowed through the packed bed. After the bed was saturated with the fluorescein dye solution, photobleaching and fluorescence detection were started. Once a stable fluorescence signal with constant baselines for both bleached and undamaged dye plugs was observed, the time-of-flight was recorded. Thus, the velocity of water flow at a specific pressure was measured. Then, the subsequent measurements of water flow velocities at higher pressures were performed. The porosity of the silica porous bed was calculated from the slope of pressure vs velocity graph following the Kozeny-Carman equation, where the no-slip boundary condition for water flow through silica porous media was utilized. Then, interstitial flow velocity and Reynold's number in a single pore were calculated.

After characterizing the porous bed, n-octane flow experiments were performed with the same experimental setup. At first, the whole fluidic setup was rinsed with several fluids to make it ready for n-octane flow measurements. Figure 4.3 illustrates the series of rinsing done to condition the fluidic unit for n-octane flow experiments. A stream of ultrapure water was charged to rinse all fluidic channels, including the porous bed, until removing all fluorescein dye (water-soluble) was confirmed with diminishing fluorescence intensity. Then, the liquid container was emptied, and only helium gas was flowed at high pressure (1000-2000 psi), to exclude any bulk water from the fluidic system.

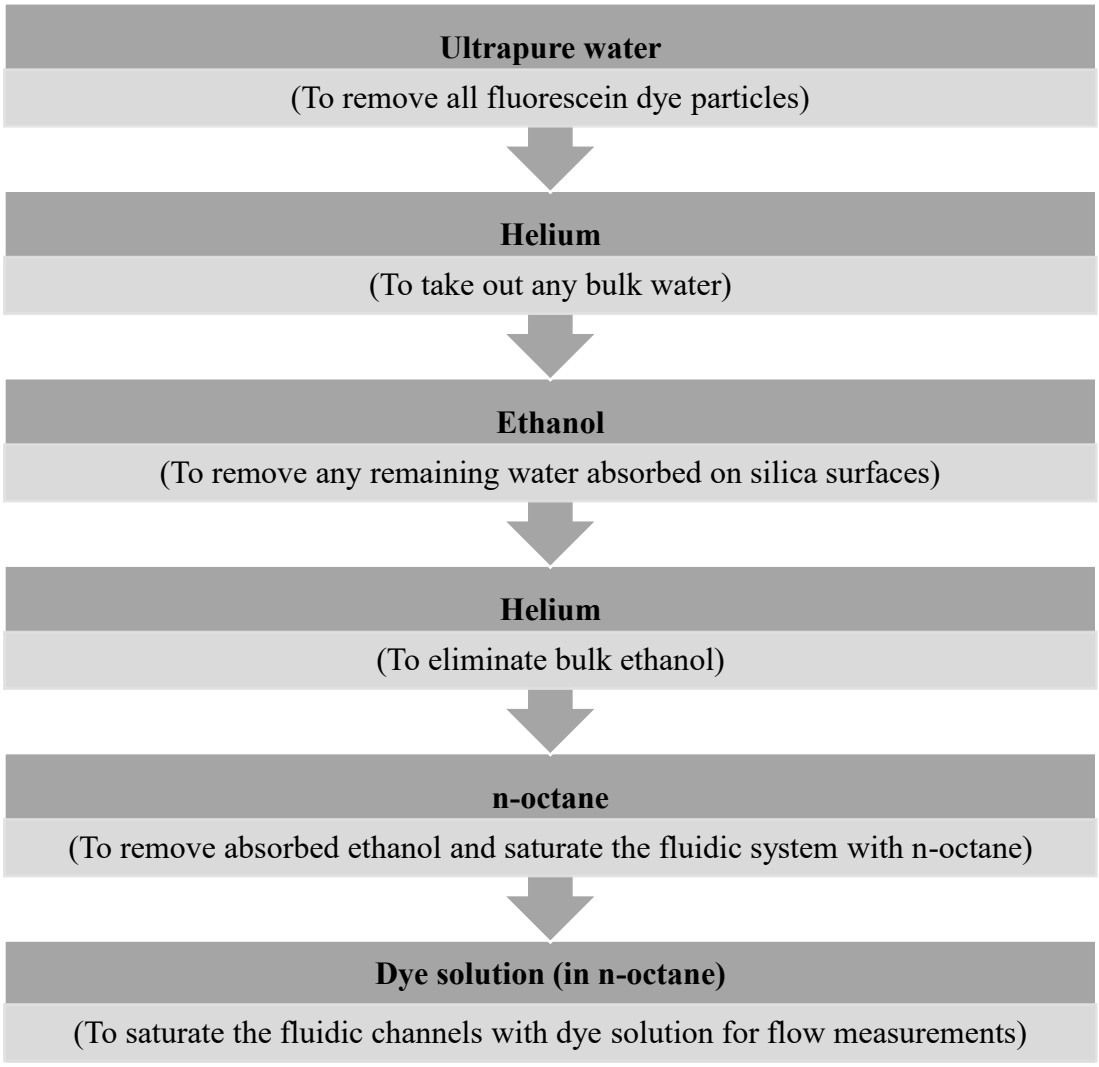

Figure 4.3: The sequence of fluids used for rinsings between water and n-octane flow measurements.

Ethanol was used as the intermediate rinsing fluid between water and n-octane due to its miscibility in both liquids [97, 98]. First, the liquid container was filled with ethanol and then pressurized with helium gas to flow through the fluidic system to take out any absorbed water on silica surfaces of the capillary column and porous bed. Thus, water was removed entirely. Later,

helium gas alone, and then fresh n-octane, were charged to eliminate the ethanol in bulk amount followed by any absorbed ethanol layer, respectively. Then, a 150 nM nile red (in n-octane) solution, saturated with oxygen to assist in dye photobleaching, was loaded into the fluidic channels.

A similar strategy of photobleaching, detection and data collection applied in water flow measurements was utilized for n-octane flow measurements. Temperatures of both water and n-octane were constantly monitored during the flow measurements to decide the value of viscosity of liquids with respect to the instantaneous temperature of the flow experiment. The slope of the theoretical flow-pressure curve was compared with that obtained from the experimental results to determine the existence of slip or no-slip flow and calculate the extent of flow enhancement. Moreover, the absolute permeability of the silica porous bed for n-octane was calculated according to Darcy's equation.

Another trial of water flow measurement was then performed, to verify the stability of the porous bed and the reproducibility in its flow properties. The fluidic system, including the porous bed, was conditioned again for water flow measurements by rinsing with fluids in the order of n-octane, helium, ethanol, helium, water, and aqueous dye solution. Once the second trial of water flow measurements was completed, the fluidic system was flushed thoroughly with ultrapure water to remove dissolved dye molecules and prewet the silica surfaces with water. After filling and wetting the porous bed with water, 150 nM dye solution (in n-octane) was flowed through it. Once the fluorescence signal became stable, confirming the absence of the bulk water in the n-

octane stream, the flow velocities of n-octane were measured. In this case, it was assumed that water molecules were still sticking on the silica surface [99, 100]. Thus, the flow measurement for n-octane was carried out in the presence of an absorbed water layer to determine the effective permeability (available pore spaces) of the porous bed for n-octane.

The efficacy of this approach to creating an adsorbed water layer is well recognized, in that even in a humid environment a substantial water layer is present. Asay et al. [99] have stated, “In low humidity (RH below 30%), the adsorbed water forms an icelike network on the silicon oxide surface that propagates up to ~3 layers from the surface at room temperature. The hydrogen bond network structure competes with the liquid water structure in the RH range of 30-60%, above which the liquid structure dominates.”. Later Umezawa et al. [100] cited Asay et al. [99] stating “In fact, from 0.3 nm to 3 nm of water molecule layers are considered to be adsorbed on silica surfaces at RHs from 7.3% to 99.4%", and also commented in their own work, “The water film thickness for silica nanoparticles becomes larger by this fitting ranging from 0.08 nm to 0.23 nm, which are more realistic for adsorbed water molecular layers.”.

4.3. Theory

4.3.1 Pore size

In a packed bed of spherical particles, the pores are interconnected for fluid flow. However, the fluidic channel made of these interconnected pores does not have a true circular cross-section [101]. For convenience, we assume that pores are cylindrical and the pore size

(r_{pore}, the radius of a pore) can be expressed in terms of porosity of the bed (ε) utilizing the concept of hydraulic radius (r_h), which is the ratio between the cross-sectional area normal to flow and the wetted perimeter [102]. Therefore,

$$r_h = \frac{\text{cross-sectional area perpendicular to the flow direction}}{\text{wetted perimeter}}$$

$$= \frac{\pi r_{pore}^2}{2\pi r_{pore}}$$

$$= \frac{r_{pore}}{2} \text{ ……..……..…….(4.1)}$$

Hydraulic radius for a porous bed can also be expressed as [83, 102] –

$$r_h = \frac{\text{volume open to the flow}}{\text{total wetted surface area}}$$

$$= \frac{(\text{volume of porous bed})(\text{porosity of the bed})}{(\text{number of spherical particles})(\text{surface area of one particle})}$$

$$= \frac{(\text{volume of porous bed})\varepsilon}{(\text{number of spherical particles})(\text{surface area of one particle})} \text{ …....(4.2)}$$

Where,

$$\text{number of spherical particles} = \frac{(\text{volume of porous bed})(\text{fraction of solid in the bed})}{(\text{volume of one particle})}$$

$$= \frac{(\text{volume of porous bed})(1-\varepsilon)}{(\text{volume of one particle})} \text{ ..……...……...…. (4.3)}$$

Substituting equation 4.3 into equation 4.2 gives,

$$r_h = \frac{(\text{volume of one particle})\varepsilon}{(\text{surface area of one particle})(1-\varepsilon)}$$

$$= \frac{(\frac{4\pi r_{particle}^3}{3})\varepsilon}{(4\pi r_{particle}^2)(1-\varepsilon)}$$

$$= \frac{(r_{particle})\varepsilon}{3(1-\varepsilon)}$$

$$= \frac{(d_{particle})\varepsilon}{6(1-\varepsilon)} \quad \text{..... (4.4)}$$

Here, $r_{particle}$ and $d_{particle}$ represent the radius and diameter of a silica microsphere in the porous bed, respectively. Now, the combination of equations 4.1 and 4.4 leads to the following equation for pore radius:

$$r_{pore} = \frac{(d_{particle})\varepsilon}{3(1-\varepsilon)} \quad \text{..... (4.5)}$$

4.3.2 Flow rate and permeability

We assume that individual pores are similar to cylindrical tubes running parallel to the flow direction, with the same length as the porous bed. Then, n number of these pores are put in parallel to calculate the net flow rate, where n is the number of pores in a cross-section of the whole capillary diameter.

According to the Hagen-Pousielle equation [4], the volumetric flow rate (Q_P) through a single pore is –

$$Q_P = \frac{\Delta P \pi r_{pore}^4}{8\eta L} \quad \text{(4.6)}$$

where:

ΔP is the pressure difference between the two ends of porous bed,

L is the length of the porous bed,

η is the dynamic viscosity of the liquid of interest,

Q_P is the volumetric flow rate through a pore,

r_{pore} is the smallest radius of a pore.

If the radius of a packing capillary tube is R, the free cross-sectional area in the packed capillary tube is $\pi R^2 \varepsilon$. Therefore, the number of pores in a cross-section of the packed capillary tube is –

$$n = \frac{\pi R^2 \varepsilon}{\pi r_{pore}^2} = \varepsilon \left(\frac{R}{r_{pore}} \right)^2 \quad \text{(4.7)}$$

The total volumetric flow rate (Q_T) through all the pores in parallel is –

$$Q_T = nQ_P \quad \text{(4.8)}$$

Substituting the values of Q_P and n from equations 4.6 and 4.7, respectively, into equation 4.8 leads to:

$$Q_T = \varepsilon \left(\frac{R}{r_{pore}}\right)^2 \left(\frac{\Delta P \pi r_{pore}^4}{8\eta L}\right)$$

$$= \frac{\Delta P \varepsilon \pi R^2 r_{pore}^2}{8\eta L} \quad \text{..... (4.9)}$$

Therefore, the average linear flow velocity (v_{ave}) measured in the open column downstream of the packed bed is –

$$v_{ave} = \frac{Q_T}{A} = \frac{\frac{\Delta P \varepsilon \pi R^2 r_{pore}^2}{8\eta L}}{\pi R^2} = \frac{\Delta P \varepsilon r_{pore}^2}{8\eta L} \quad \text{..... (4.10)}$$

where A is the cross-sectional area of the capillary column of the porous bed. Now, the substitution of equation 4.5 into equation 4.10 yields,

$$v_{ave} = \frac{\Delta P \varepsilon [\frac{(d_{particle})\varepsilon}{3(1-\varepsilon)}]^2}{8\eta L}$$

$$= \frac{\Delta P d_{particle}^2 \varepsilon^3}{72\eta L(1-\varepsilon)^2} \quad \text{..... (4.11)}$$

However, fluids flow through tortuous fluidic paths (as shown in Figure 4.4) rather than parallel straight channels in the interconnected pore network structure of the porous bed. Hence, it is reasonable to consider effective travel distance (L_e) instead of the length (L) of the porous bed for a more accurate prediction of porous media flow velocity. Therefore, rewriting the equation 4.11 in terms of effective fluidic length (L_e) results in:

$$v_{ave} = \frac{\Delta P d_{particle}^{2} \varepsilon^{3}}{72 \eta L_e (1-\varepsilon)^2} \quad \text{(4.12)}$$

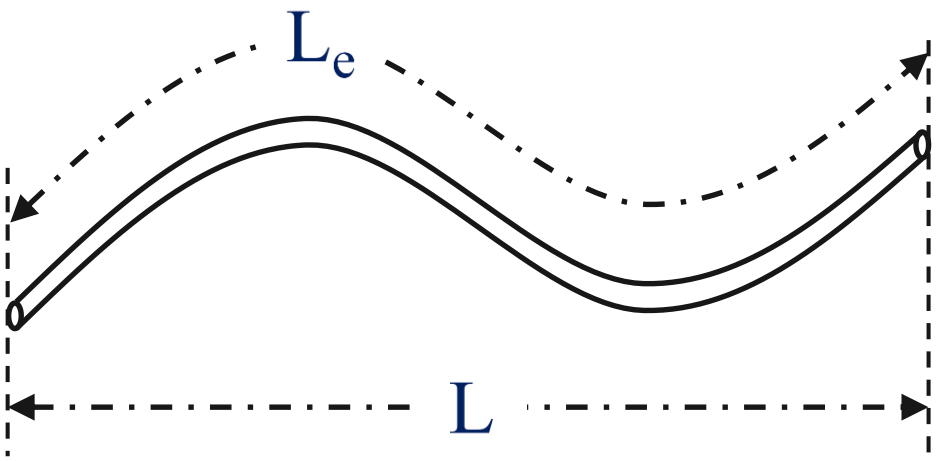

Figure 4.4: Tortuous fluidic channel where Le is the effective length of fluidic path and L is the length of the porous bed.

Since the tortuosity factor, τ (= L_e/L), is the ratio between the effective fluidic length (L_e) to the porous bed length (L), equation 4.12 can be written as:

$$v_{ave} = \frac{\Delta P d_{particle}^{2} \varepsilon^{3}}{72 \eta \tau L (1-\varepsilon)^2} \quad \text{(4.13)}$$

In a packed porous bed, the tortuosity factor varies from 2.0 to 2.5 depending on the packing order [103]. Based on some theoretical and phenomenological studies, 2.5 is the most accepted value for the tortuosity factor in practice [104, 105], which implies:

$$v_{ave} = \frac{Q_T}{A} = \frac{\Delta P d_{particle}^{2} \varepsilon^{3}}{180 \eta L (1-\varepsilon)^2} \quad \text{(4.14)}$$

The above equation is widely known as the Kozeny-Carman equation (3.1), that estimates the flow velocity as a function of pressure in porous media [82, 106].

In the above equation, the diameter of a packing particle and the porosity of a packed bed are fixed. Hence, the combined term $\frac{d_{particle}^2 \varepsilon^3}{180(1-\varepsilon)^2}$ can be considered as a constant (k). Thus, equation 4.14 can be written in the following form, which is also known as Darcy's equation (3.4) [107]:

$$v_{ave} = \frac{k\Delta P}{\eta L} \quad \text{(4.15)}$$

Where, k ($= \frac{d_{particle}^2 \varepsilon^3}{180(1-\varepsilon)^2}$) is termed as the absolute permeability of the porous media.

4.3.3 No-slip and slip flow rates

With a no-slip boundary condition, a liquid flowing in a cylindrical tube of radius R with a laminar flow pattern attains a parabolic velocity profile (shown in Figure 1.6), which is expressed as [41]:

$$v_z(r) = \frac{\Delta P}{4\eta L}(R^2 - r^2) \quad \text{(1.3)}$$

where,

$v_z(r)$ is the velocity of the liquid in the z-direction

ΔP is the applied pressure,

η is the dynamic viscosity of the liquid,

L is the length of the cylindrical tube,

R is the radius of the tube, and

r is the radial distance from the centre of the tube.

The velocity, $v_z(r)$, varies along the radial distance of the tube. It is maximum at the centre (r = 0) of the tube, and zero at the tube wall (r = R). The volumetric flow rate, $Q_{no\text{-}slip}$ can be expressed as:

$$Q_{no\text{-}slip} = \int v_z(r)dA \quad \text{.....} \quad (4.16)$$

where, dA is the differential cross-sectional area of the tube, and in cylindrical coordinate, $dA = 2\pi rdr$.

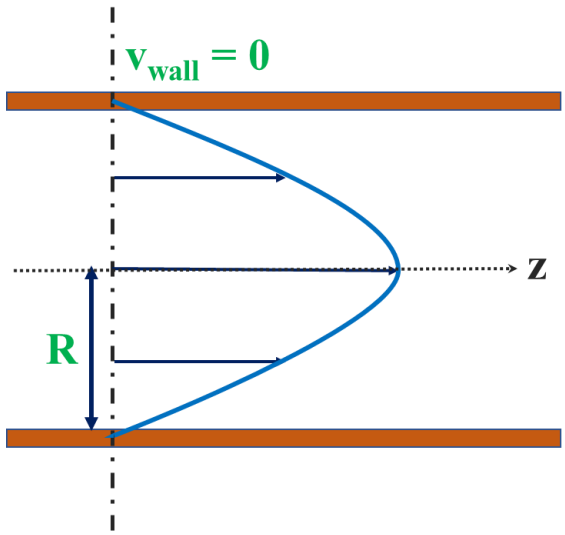

Figure 1.6: Parabolic flow profile at no-slip boundary condition.

Therefore,

$$Q_{no\text{-}slip} = \int v_z(r)\, dA = \int_0^R v_z(r) 2\pi r dr$$

$$= \int_0^R \frac{\Delta P}{4\eta L}(R^2 - r^2) 2\pi r dr$$

$$= \int_0^R \frac{\pi \Delta P}{2\eta L}(rR^2 - r^3) dr$$

$$= \frac{\pi \Delta P}{2\eta L}\left[\frac{r^2 R^2}{2} - \frac{r^4}{4}\right]_0^R$$

$$= \frac{\pi \Delta P}{2\eta L}\left(\frac{R^4}{2} - \frac{R^4}{4}\right)$$

$$= \frac{\Delta P \pi R^4}{8\eta L} \quad \text{..... (4.17)}$$

The above equation is also known as the Hagen-Poiseuille equation [108, 109]. The velocity profile is totally parabolic in shape at the no-slip boundary condition, and the wall velocity is zero. On the other hand, at the slip boundary condition (shown in Figure 4.5), the velocity profile crosses the wall boundary by a certain length, called slip length (L_s). Considering a linear velocity profile after the wall surface, the ratio of slip-wall velocity (v_{wall}) to the radial velocity gradient (dv/dr) at the wall gives the measure of slip length [41, 110]. Therefore,

$$v_{wall} = L_s \frac{dv_z(r)}{dr} \quad \text{..... (4.18)}$$

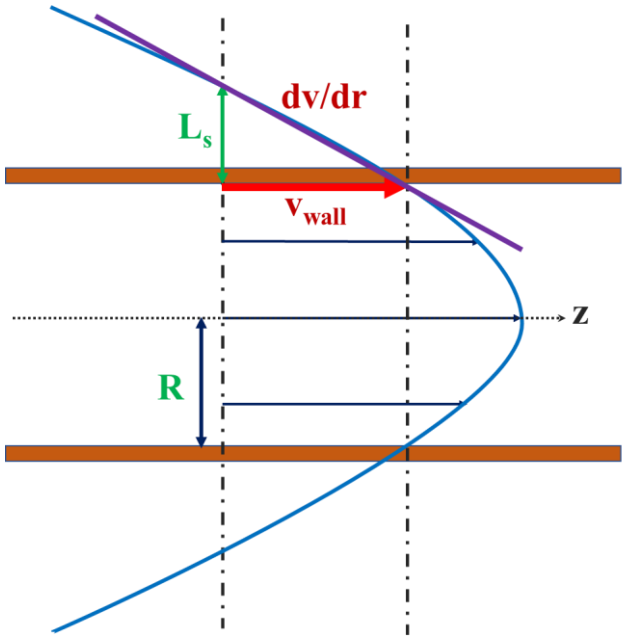

Figure 4.5: Velocity profile at slip boundary condition.

In the presence of slip flow, the cumulative velocity (v_{slip}) in the cylindrical column will be –

$$v_{slip} = v_z(r) + v_{wall} \quad \text{(4.19)}$$

Hence,

$$Q_{slip} = \int v_{slip}\, dA$$

$$= \int v_z(r) dA + v_{wall} dA$$

$$= \frac{\Delta P \pi R^4}{8\eta L} + L_s \frac{dv_z(r)}{dr} dA$$

$$= \frac{\Delta P \pi R^4}{8\eta L} + L_s \frac{dQ_{no\text{-}slip}}{dr}$$

$$= \frac{\Delta P \pi R^4}{8\eta L} + L_s \frac{d}{dr}\left(\frac{\Delta P \pi R^4}{8\eta L}\right)$$

$$= \frac{\Delta P \pi R^4}{8\eta L} + L_s \frac{\Delta P \pi 4R^3}{8\eta L}$$

$$= \frac{\Delta P \pi R^4}{8\eta L}\left(1+\frac{4L_s}{R}\right)$$

$$= Q_{no\text{-}slip}\left(1+\frac{4L_s}{R}\right) \quad \text{(4.20)}$$

However, the ratio between slip and no-slip volumetric flow rate is called the flow enhancement factor (E) [111]. Therefore, E can be expressed as –

$$E = \frac{Q_{slip}}{Q_{no\text{-}slip}} = \frac{v_{slip}}{v_{no\text{-}slip}} \quad \text{(4.21)}$$

The standard deviation in the flow enhancement can be calculated by equation:

$$\Delta E = \left(\frac{E_{average}}{100}\right)\sqrt{(\text{RSD in slope}_{\text{slip curve}})^2 + (\text{RSD in slope}_{\text{no-slip curve}})^2} \quad \text{(4.21a)}$$

Moreover, the slip length can be expressed as –

$$L_s = \frac{R}{4}\left(\frac{Q_{slip}}{Q_{no\text{-}slip}} - 1\right) = \frac{R}{4}(E-1) \quad \text{(4.22)}$$

In the case of porous media, the radius (R) of the fluidic channel is equivalent to the pore radius (r_{pore}) [41]. Hence, the equation of slip length can be modified into –

$$L_s = \frac{r_{pore}}{4}(E\text{-}1)\text{…….……..…….(4.23)}$$

The standard deviation in the slip length can be calculated by equation:

$$\Delta L_s = \left(\frac{L_s}{100}\right)\sqrt{(\text{RSD in } r_{pore})^2 + (\text{RSD in } E)^2}\text{……..(4.23a)}$$

4.3.4 Flow properties within pores

Reynolds number (R_e), a ratio between inertial forces to viscous forces within a fluid [112, 113], is usually used as a tool to determine the flow pattern (laminar or turbulent) in a fluidic channel. The Reynolds number for fluid flow in a pipe, $(R_e)_{tube}$, is quantified according to the following equation [113]:

$$(R_e)_{tube} = \frac{\rho.v_{ave}.D_{tube}}{\eta}\text{……..…….…….…….…….…….} \quad (4.24)$$

Where,

ρ is the density of fluid;

v is the average velocity of fluid;

D_{tube} is the hydrodynamic diameter of the pipe;

η is the dynamic viscosity of the fluid.

However, to predict the flow pattern within pores, interstitial pore velocity (v_{pore}) and hydrodynamic diameter (d_{pore}) of a pore must be considered. In that case, for flow within a cylindrical pore, porous media Reynolds number can be written as [114]:

$$(R_e)_{pore} = \frac{\rho . v_{pore} . d_{pore}}{\eta} \quad \text{(4.25)}$$

Since the hydrodynamic pore diameter is much smaller than the porous bed diameter, fluid moves a lot faster through small pores to maintain a uniform volumetric flow rate at the inlet and outlet of the porous media, i.e., the actual pore or interstitial velocity (v_{pore}) is higher compared to the empty tower or average flow velocity (v_{ave}) having the following relationship [114] –

$$v_{pore} = \frac{v_{ave}}{\varepsilon} \quad \text{(4.26)}$$

Here the empty tower velocity means the average linear flow velocity, which is the ratio of the volumetric flow rate of the liquid to the cross-sectional area of the empty capillary column. On the other hand, the interstitial velocity means the fluid velocity (convective) between the interparticle pores of a packed porous bed [115]. It was shown in equation 4.5 that pore size in a porous media depends on particle diameter and overall bed porosity with the following relationship –

$$r_{pore} = \frac{(d_{particle})\varepsilon}{3(1-\varepsilon)} \quad \text{(4.5)}$$

Since the hydrodynamic pore diameter is twice of the pore radius –

$$d_{pore} = \frac{2(d_{particle})\varepsilon}{3(1-\varepsilon)} \quad \text{(3.5)}$$

Then, substituting equations 4.26 and 3.5 into equation 4.25 yields –

$$(R_e)_{pore} = \frac{\rho\left(\frac{v_{ave}}{\varepsilon}\right)\left[\frac{2(d_{particle})\varepsilon}{3(1-\varepsilon)}\right]}{\eta} = \frac{2\rho v_{ave} d_{particle}}{3\eta(1-\varepsilon)} \quad \text{.....(4.27)}$$

However, the numerical factor, 2/3, is usually omitted, and the porous media Reynolds number is expressed in the following modified form [114, 116, 117] –

$$(R_e)_{pore} = \frac{\rho v_{ave} d_{particle}}{\eta(1-\varepsilon)} \quad \text{.....(4.28)}$$

4.4 Results and discussion

The same fluidic and optical setup was employed for the flow measurements of both n-octane and water. Figure 4.6 shows the fluorescence spectra of nile red dye solution in n-octane and aqueous fluorescein disodium salt dye solution. The excitation maxima for nile red dye solution in n-octane and aqueous fluorescein disodium salt dye solution were found to be 491 and 492 nm, respectively. Hence, 488 nm argon-ion laser was energetic enough to excite both dye molecules. On the other hand, the emission maxima for nile red dye solution in n-octane and aqueous fluorescein disodium salt dye solution were found to be 530 and 514 nm, respectively. Hence, the 505 nm dichroic mirror was found suitable for reflecting the laser excitation beam (488nm) and transmitting fluorescence signals.

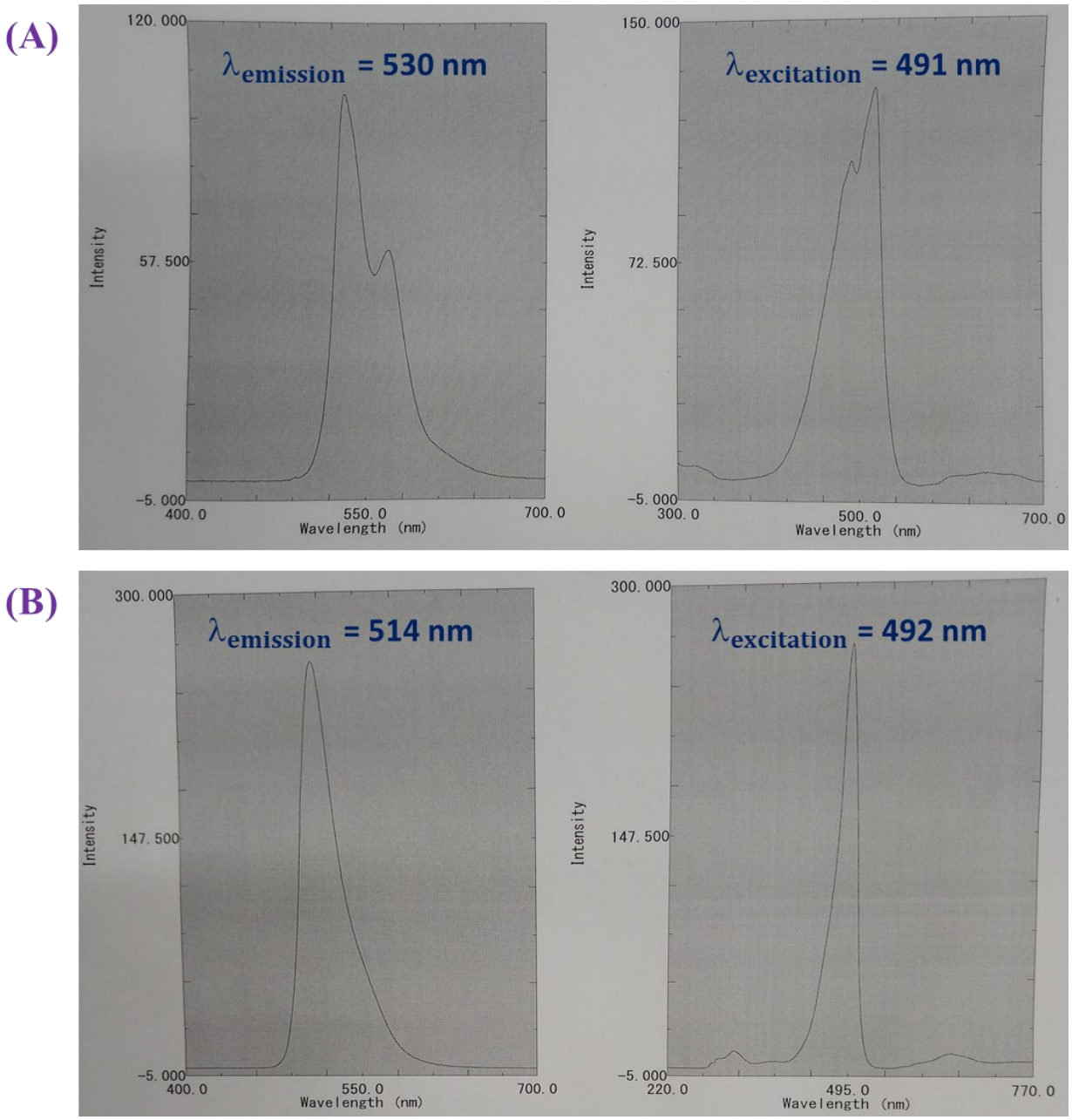

Figure 4.6: Fluorescence spectrum of (A) nile red dye solution in n-octane and (B) aqueous fluorescein disodium salt dye solution.

4.4.1 Porous media flow measurements

Water was flowed through a 7.5 mm long porous bed packed in a 73.5 µm ID capillary column at 23°C. The pressure for fluid delivery was varied from 400-2100 psi from a constant pressure pumping source, and the corresponding volumetric flow rates of water were measured. Figure 4.7 represents the observed flow rate versus pressure data. An increase in the applied pressure produced a higher volumetric flow rate of water. The flow rate versus pressure drop follows a linear relationship.

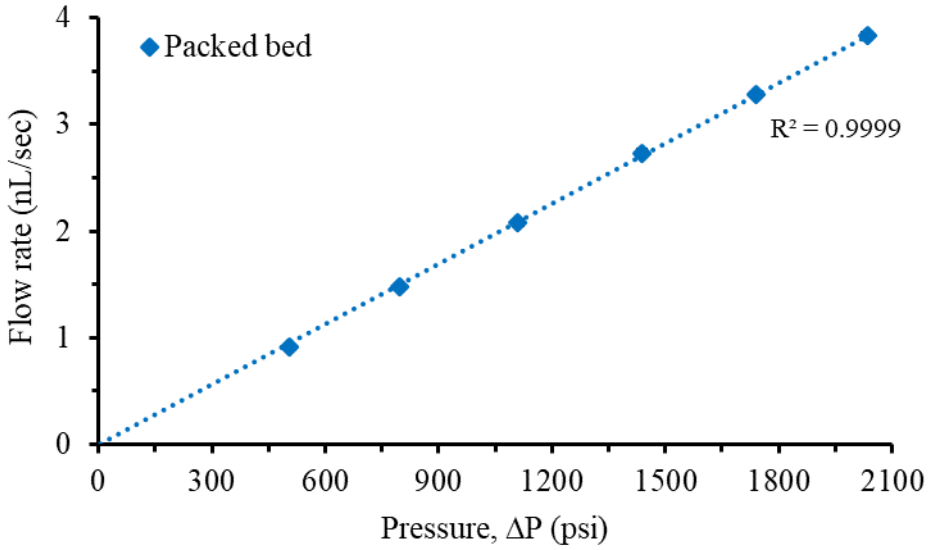

Figure 4.7: Pressure vs volumetric flow rate for water through a 7.5 mm long porous bed packed in 73.5 µm ID capillary column. Error bars represent standard deviations (in nL/sec unit). However, bars are not visible here since these are smaller than the symbols used for the average values. RSD values for these data points are less than 1.7%.

However, there are some additional pressure drops involved for these volumetric flow rates. In addition to the porous bed, the fluidic assembly consists of frit, detection column, restrictor, unions, and stainless-steel tubes. Therefore, we needed to estimate the additional pressure drops that arise from these units. The frit, detection column (empty capillary) and restrictor are the significant additional sources of pressure drops. Figure 4.8 summarizes the expected pressure drop in those elements at the average water flow rates observed within the overall fluidic setup.

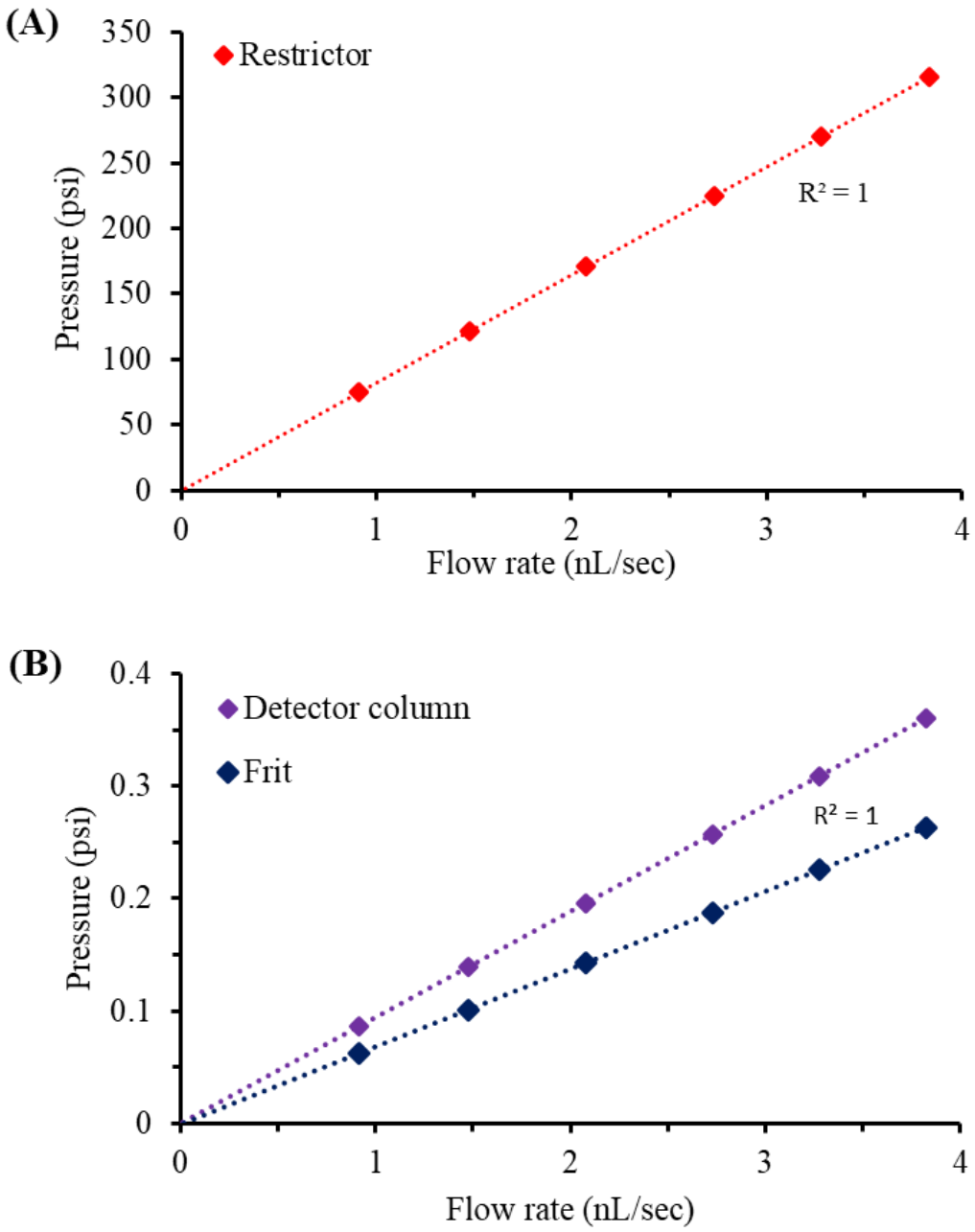

Figure 4.8: Pressure vs volumetric flow rate for water flow through (A) 15 cm long 10 µm ID restrictor, (B) frit and 50 cm long 73.5 µm ID detector column.

As a restrictor, a 15 cm long, 10 μm ID capillary column was used, while a 50 cm long and 73.5 μm ID capillary tube was used as the detection column. As both columns are cylindrical, the Hagen-Pousielle equation (shown below) was used to calculate the expected pressure drops for water flow in the restrictor and detection column as a function of certain volumetric flow rates observed for the porous bed.

$$\Delta P = \frac{8Q\eta L}{\pi R^4} \quad \text{(1.4)}$$

where:

ΔP is the pressure difference between the two ends of the capillary tube,

L is the length of the tube,

η is the dynamic viscosity of the liquid of interest,

Q is the volumetric flow rate through the tube,

R is the radius of the tube.

Moreover, the pressure drops in a frit (0.5 μm diameter pore, 1.6 mm width, 1.6 mm thickness, 0.2 porosity) for the same volumetric flow rates were calculated using equation 3.1 (Kozeny-Carman equation). Finally, the combined pressure drop that arose in the restrictor, frit and detection column for a particular flow rate was subtracted from the applied pressure, to determine the actual pressure required to maintain that flow rate in the porous bed. The value of dynamic viscosity of water used in these calculations was 0.931 mPa.sec at 23°C (the temperature recorded during velocity measurement). For example, for 1.47 nL/sec volumetric flow rate through the porous bed, the required pressure is:

$$\Delta P_{actual} = \Delta P_{applied} - (\Delta P_{restrictor} + \Delta P_{detector\ column} + \Delta P_{frit})$$

$$= 798 - (121.673 + 0.139 + 0.101) \text{ or, } 676.086 \text{ psi}$$

Figure 4.9 shows the dependence of average linear flow (empty tower) velocity on actual applied pressure for water flow through a 7.5 mm long porous packed bed. It was assumed that water flow in silica porous bed follows no-slip boundary condition. The water flow velocity data obtained were best fit by equation 3.1 (Kozeny-Carman equation) to determine the bed porosity, which was found to be 0.345 ± 0.001. Therefore, the average pore radius would be 175.6 ± 0.5 nm, calculated based on equation 4.5. Error propagation on eq 4.5 provides an estimate of error (Δr_{pore}) in the pore radius given by $\Delta r_{pore} = \left(\frac{\Delta\varepsilon}{\varepsilon} \times 1.4\right) \times r_{pore}$, where $\Delta\varepsilon$ is the standard deviation in porosity.

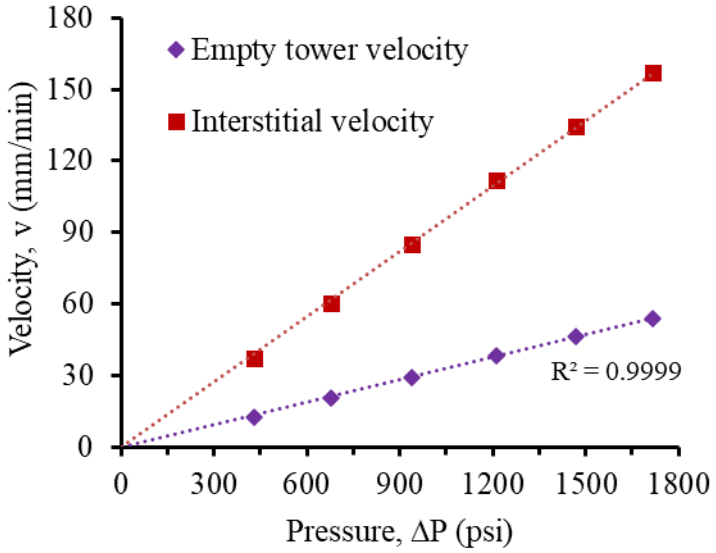

Figure 4.9: Variation of empty tower (linear flow) velocity and interstitial pore velocity through a packed porous bed having 7.5 mm length and 0.345 ± 0.001 porosity at 23°C. Error bars express

the standard deviation (in mm/min unit). However, bars are smaller than the symbols used for the average values.

The porous bed comprises smaller flow channels compared to the empty column. Consequently, water flows 2.9 times faster through the pores of the porous bed in comparison to the empty column to maintain the same volumetric flow rate. The flow velocity within pores of the bed calculated using equation 4.26 is shown in Figure 4.9. Both interstitial velocity and empty tower velocity were used to calculate the Reynolds number for fluid flow within pores and the empty column following equations 4.28 and 4.24, respectively. Table 4.1 shows the variation of Reynolds numbers within the applied pressure range. Here, the Reynolds numbers within pores and empty capillary section are much below 1, which indicates that the fluid flow through the porous media follows the steady-state laminar flow pattern. A linear relationship between flow rate and pressure gradient in combination with a laminar flow pattern (R_e <1) validates the applicability of Darcy's law for any porous system [118, 119]. The results obtained in this study meet both criteria, implying that the application of Darcy's and the Kozeny-Carman equations to describe the porous media flow characteristics is appropriate.

Table 4.1: Reynolds number within the porous structure and in an empty section of capillary.

Pressure (psi)	Empty tower velocity (mm/min)	R_e (in pore)*	R_e (in empty capillary)*
430	12.9 ± 0.1	0.0004	0.017
676	20.8 ± 0.1	0.0006	0.028
938	29.4 ± 0.5	0.0008	0.039
1211	38.6 ± 0.5	0.0011	0.051
1470	46.4 ± 0.2	0.0013	0.061
1717	54.1 ± 0.4	0.0015	0.071

*Here the relative standard deviation (%) values for R_e (in pore) and R_e (in empty capillary) are less than 1.7%.

4.4.2 Assessment of flow measurement technique

In the velocity measurement technique used in this study, photobleaching followed by fluorescence detection was done downstream of the porous bed. The frit used to keep the porous bed immobile at the end of the column also acts as a secondary porous bed. The fluid travelling through the small fluidic channels leaves the porous system as several tiny segments of fluid, which then coalesce together to form bulk fluid again near the entry point of the detection column. Viscous forces spreading from the column wall induce the formation of a fully developed flow velocity profile at a certain distance (entrance length) from the entry area of the column. A fully developed steady-state laminar flow velocity profile develops at an entrance length (E_L) of –

$$E_L = 0.06(R_e)_{tube} D \quad (4.29)$$

Where D is the hydrodynamic diameter of the detection column and $(R_e)_{tube}$ is the Reynolds number in the column, calculated according to equation 4.24. The entrance length values for different flow velocities obtained at different pressure settings calculated according to equation 4.29 are summarized in Figure 4.10.

It was found that flow attains a fully developed velocity profile within less than 1 μm entrance length. In this study, velocity measurements were done at least 20 cm downstream of the porous bed and 20 cm upstream of the restrictor within a 50 cm long detection column. Thus, the flow was unaffected by any entrance effects, even at very high flow rates. In addition, the backpressure drop created at the restrictor ensures a uniform flow profile throughout the detection column after the entrance length.

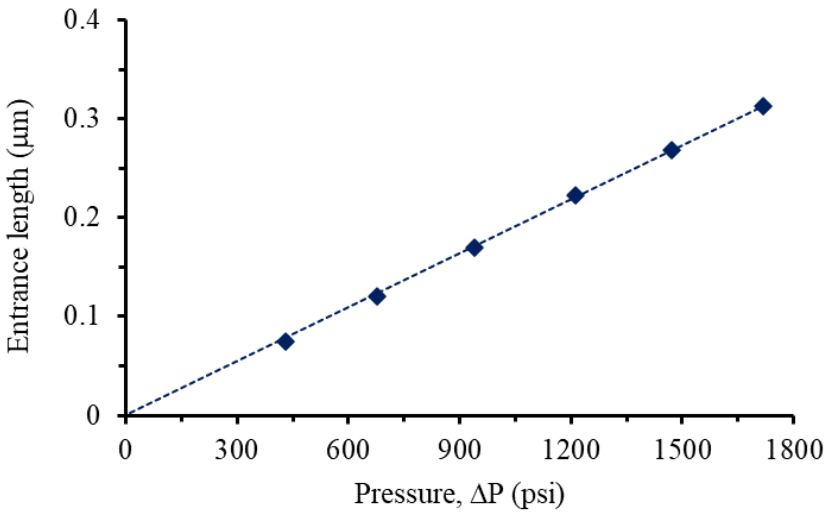

Figure 4.10: The variation of entrance length.

The photobleaching of dye molecules creates a local concentration gradient in the dye solution giving rise to the diffusion process, which is accentuated by the Taylor-Aeris dispersion process. Dispersion in the flow direction decreases the intensity of the bleaching-induced fluorescence signal change. If the linear flow velocity is too low, the shape of the square wave concentration of bleached and undamaged dye solution plugs is distorted by diffusion, as discussed in detail in Chapter 2. As long as the centre peak of the bleached plug flow is not yet depleted, the approximation that the time of travel of the 50% point reflects the average flow profile remains accurate to 0.1 to 2 % depending on the velocities involved. That is why the detection locations (L_1 and L_2) were occasionally adjusted to keep that approximation valid.

4.4.3 The flow of a non-wetting fluid

After determining the porosity of the porous bed by pressure-driven water flow measurement, the same porous bed was used again for n-octane flow. For the same length of the porous bed, the theoretical velocity of n-octane and the experimental (no-slip) water velocity coincide with each other, provided the velocities were normalized with the respective fluids' viscosities (shown in Figure 4.11). However, n-octane flow exhibits higher velocity experimentally than the theoretical prediction, i.e., slip flow exists in the case of n-octane through a silica porous system. The extent of flow enhancement was 1.36 ± 0.03, with a slip length of 16.0 ± 0.3 nm in this case. The flow enhancement and its standard deviation were calculated according to equations 4.21 and 4.21a, respectively, whereas the slip length and its standard deviation were calculated based on equations 4.23 and 4.23a, respectively. Packed beds prepared with the same particle size may have slight differences in porosity values, as observed in Chapter 3. However, the resulting differences among the slip length values measured for multiple columns were found not larger than 10 % RSD. The slope (0.2245) of the pressure-velocity curve obtained from the second trial of water flow measurement is close to that (0.2198) obtained in the first trial, which confirmed the stability of the packed bed during the flow measurements.

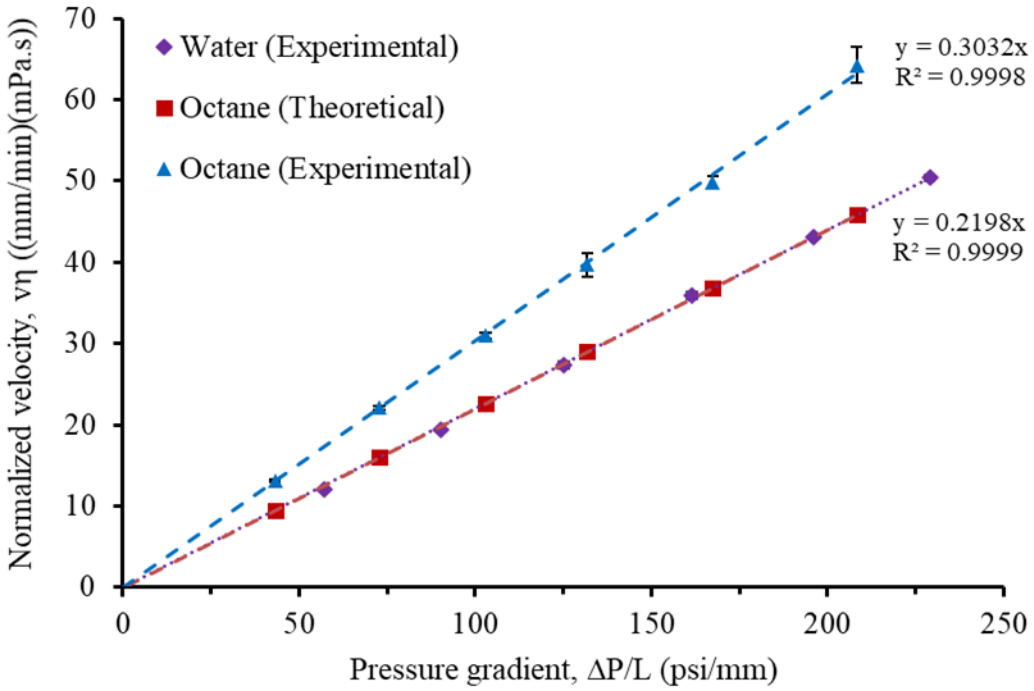

Figure 4.11: Variation of linear velocity with pressure gradient for water and n-octane flow in a 7.5 mm long packed bed of 1000 nm silica microspheres. Velocities were normalized for viscosities of water (0.931 mPa.s) and n-octane (0.556 mPa.s) at 23°C. Error bars express the standard deviation in (mm/min)(mPa.sec) unit. However, in some cases, bars are smaller than the symbols used for the average values.

The surface of silica microspheres is covered mainly by silanol (Si-OH) groups [120]. In the pH range of 2 to 12, the following acid-base equilibrium is one of the predominate reactions on a silica surface, involving silanol groups [121-124]:

$$SiOH \leftrightarrow SiO^{-} + H^{+}$$

The difference between the pK_a value of silanol groups on a silica surface and the pH of the surrounding environment determines the charge density on the silica surface, according to the Henderson-Hasselbalch equation:

$$pH = pK_a + \frac{[SiO^-]}{[SiOH]}$$

About 15-19% of silanol groups on the silica surface have a pK_a value of 4.5-5.5, whereas 81-85% of silanol groups carry a pK_a value of 8.5-9.9 [125]. These differences arise from the varying functional groups attached to each SiOH moiety [121-125]. In neutral condition (pH = 7), a part of the silica surface becomes deprotonated and negatively charged. The remaining part stays in neutral protonated form. Water is a polar molecule in nature, with acid and base characteristics. It wets the silica surface by forming hydrogen bonds with both protonated and deprotonated forms of the silanol group. Therefore, water forms a sticky layer on the silica surface and develops a no-slip boundary condition [99, 100].

On the other hand, n-octane is neutral and nonpolar in nature, since the electronegativity difference between carbon and hydrogen is very small. As a result, n-octane cannot form any strong dipole-dipole or hydrogen bond with the silica surface. Instead, weak Van der Waals interactions exist between n-octane and silica. As a result, n-octane does not bind on the silica surface, giving rise to nonzero flow velocity at the silica wall. Thus, surface interaction of fluids with silica plays a significant role in slip or no-slip flow phenomena. Our result is the mirror image of flow behaviour of water through an RPLC column, having a non-polar hydrocarbon

chain coated porous bed, where water does not wet the surface and has a non-zero slip condition, as demonstrated by the Wirth group [14, 15]. They observed water flow enhancement in the C4 hydrocarbon coated porous media with a slip length of 63 ± 3 nm [26], which is about 4 times higher than our slip length result (16.0 ± 0.3 nm), obtained for n-octane flow in silica porous bed.

4.4.4 Absolute vs effective permeability of n-octane in silica porous bed

When the porous bed is well dried and free of any solvent, all the pore spaces are available for a single fluid flow. Hence, it is termed the absolute permeability of the porous media for that fluid. However, if the silica porous bed is kept wetted with water, the overall available pore volume for fluid flow becomes reduced. In that case, the permeability of the silica porous bed for any other fluid except water is termed as the effective permeability [126, 127]. Figure 4.12 illustrates the scenario of available void spaces in a silica porous bed in the presence or absence of an adsorbed water layer. The difference in absolute and effective permeability of octane through silica porous bed is discussed below.

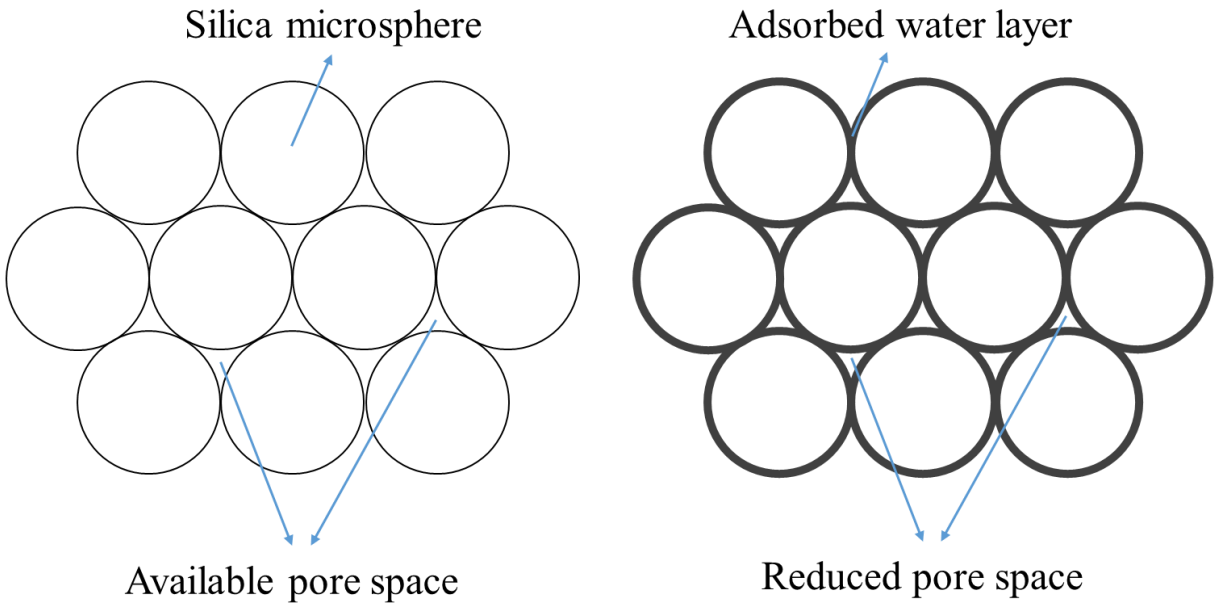

Figure 4.12: Interparticle void spaces in a silica porous bed in the presence or absence of an aqueous layer.

In the presence of an aqueous film on the silica porous bed, the effective permeability for n-octane is lower than the absolute permeability and the theoretical (no-slip) permeability of octane (shown in Figure 4.13). Since a fraction of void volume in the silica porous bed was preoccupied with the wetting fluid (water), the porosity of the bed was reduced, resulting in lower permeability for the other liquid. At no-slip condition, the estimated pore diameter is 351 nm. However, in the presence of water layer, the pore diameter reduces to 281 nm, which is 70 nm lower than its initial value in the dry state. Literature shows that up to 3 nm of water molecule layers are considered to be adsorbed on silica surfaces at 99.4% relative humidity [99, 100]. Hence, along with 1-3 layers of water molecules being adsorbed on the surface of the particles, some bulk waters are trapped at the interstices among the particles. Therefore, even though n-

octane was expected to slip on the aqueous layer, the reduced porosity dominates over the weak surface interaction as a reason for getting lower effective permeability.

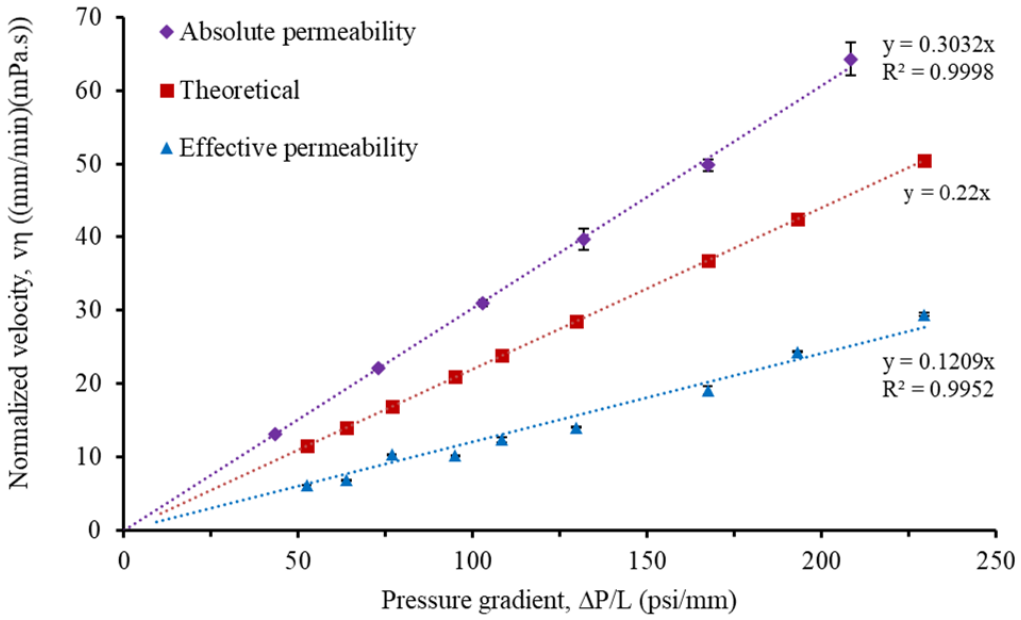

Figure 4.13: Comparison between absolute and effective permeability for n-octane flow silica porous bed.

4.5. Conclusion

The porous media flow equations, e.g., Darcy and Kozeny-Carman equations, derived based on the no-slip boundary condition, were valid in the silica microporous system (175.6 ± 0.5 nm average pore radius), especially for the wetting fluid, water. However, slip flow with a flow enhancement of 1.36 ± 0.03 and slip length of 16.0 ± 0.3 nm was observed for n-octane in this silica microporous system. Thus, this study sheds insight into how surface chemistry can modify the flow behaviour in an NPLC column having a sub-micrometre porous bed system.

However, the dependence of the extent of slip flow on pore sizes has been discussed in the next chapter, along with a comparative analysis with other theoretical and experimental works found in the literature.

Chapter 5: Effect of Pore Size on Slip Flow in Micro- and Nano Porous Media

5.1. Introduction

Slip flow phenomenon is now evident in microfluidics [128] and nanofluidics [28, 32, 55]. The previous chapter showed that the pressure-driven flow experiment for n-octane through a silica porous bed confirms the existence of slip flow [129]. The weak surface interaction between silica and n-octane caused a higher flow rate than its theoretical no-slip flow. Keeping this environment of weak fluid-wall surface interaction in effect, we have explored how the fluidic channel dimension affects the extent of flow rate enhancement.

The slip flow of water in a hydrophobic porous media system having varying pore size was reported by Rogers et al. [26]. Literature shows that an opposite fluid-wall combination, i.e. flow behaviour of n-octane (hydrophobic liquid) through dolomite and quartz slits (hydrophilic surface), was investigated by molecular dynamics (MD) simulation [20, 130], but experimentally still unexplored. Therefore, here we aimed to evaluate the effect of pore size on the variation of flow rate enhancement for a non-wetting fluid (n-octane) through silica porous media.

5.2. Experimental

5.2.1 Materials

An aqueous colloidal suspension (10 % w/v) of non-porous silica microsphere particles was used for fabricating the packed column. Different sizes (diameter) of silica particles were used for packing. 300, 500 and 690 nm diameter silica microspheres were purchased from Poly Sciences Inc. 1000 and 2000 nm diameter silica particles were bought from Bangs Laboratories Inc. Particles were packed without any chemical treatment or modification inside a fused silica capillary tube (97.5 μm ID × 360 μm OD; TSP100375, Polymicro Technologies, Molex). As fluorescence tracing dyes, nile red (Millipore Sigma) and fluorescein disodium salt (Sigma, St. Louis, MO) were used to prepare their dye solutions in n-octane (Millipore Sigma) and ultrapure water solvents, respectively. Helium gas (>99.998% purity, Praxair Canada Inc., Mississauga) was used for pressurizing dye solutions to get a constant pressure liquid flow. O_2 gas (Praxair, Mississauga, ON, Canada) was used to prepare a photo-bleachable oxygen-saturated dye solution.

5.2.2 Instrumentation and determination of linear flow velocity

The same instrumental setup (Figure 2.1 and 2.2) discussed in Chapter 2 was utilized to determine the linear flow velocity. A capillary tube with 97.5 μm inner diameter was employed as the detection column so that its diameter matches that of the porous bed column. A time-of-flight photo-bleaching velocity measurement technique, described in detail in Chapter 2, was used with no modifications. A constant pressure pump system was utilized. A gas cylinder

(helium) and regulator were used to pressurize helium gas, which was then delivered to a container of dye solution to pressurize the fluid, driving liquid flow from the fluid container by a tube located deep within the fluid. A pressure transducer was used to monitor the pressure drop across the device relative to the atmosphere. A frit with a 0.5-micrometre pore was used to support the packed porous bed, keeping it stable and stationary inside the capillary. Then, the packed column was coupled with an empty capillary having the same ID (97.5 μm), which was then again coupled with another empty capillary having a smaller ID. This 10 μm internal diameter column was used as a restrictor to avoid forming bubbles within the liquid stream.

Two 488 nm Ar ion lasers and a variety of lenses were used for photobleaching and fluorescence detection. One laser operated at high intensity was focused to photobleach the dye inside the empty capillary. A chopper was used to generate a square wave dye concentration variation by alternately directing the laser beam between the capillary and a photodiode. The second laser was used for laser-induced fluorescence detection. A dye solution flowing through the porous bed at constant pressure was photo-bleached downstream by a chopper-modulated high-intensity laser beam to generate a square wave dye concentration variation. The time of flight of the photo-bleached plug was then determined at two different detection zones downstream of the bleaching site. The fluorescence signal was measured first 1-5 mm away from the bleaching point, and the time of flight from the bleached spot was determined for about five pulse periods. The detector was then translated 0.4-2.5 mm away from the first detection point to repeat the time-of-flight measurements. The second detection spot distance was selected in order to ensure the velocity measured was equivalent to the average flow velocity, as discussed in

Chapter 2. Then, the velocity (v) was determined according to the equation, $v= \frac{L_2-L_1}{t_2-t_1}$. Here, t_1 and t_2 correspond to the times required for the bleached dye plug to reach the first (L_1) and second (L_2) detection zones, respectively. Then, the average linear velocity was calculated.

5.2.3 Fabrication of packed porous bed

The process of fabricating a packed column of porous beds (Figure 4.1) discussed in Chapter 4 was followed to make porous beds of 1000 and 2000 nm silica particles. First, the colloidal solution (10 % w/v) was wicked into an empty fused silica capillary tube (97.5 μm internal diameter, 360 μm outer diameter) by capillary action. Then, an evaporation-induced colloidal self-assembly mechanism was used for forming a packed bed of silica microspheres. Once the silica colloidal crystal is formed inside the capillary tube, sonication and high-pressure water flow were simultaneously applied for more compaction of the bed of silica particles. Then, the column was dried with a slow evaporation process by keeping the column in a humid condition to get a densely packed and crack-free porous media.

A commercial frit having 0.5 μm pore diameter was used during the compaction step of packing to keep the porous bed intact in the column by placing it at the end of the packed column. It was also used during velocity determination by coupling it in between the packed bed and the detection column. However, the 0.5-micron pore frit was sufficient to stabilize the porous beds of larger particles (e.g., 1000 and 2000 nm dia silica particles). Therefore, for taking flow measurements from packed beds of smaller particles (300, 500 and 690 nm), we had to develop a porous bed of larger particles in the column to use as the frit. The expected mean pore diameters

of the frits (packed porous bed) made with different particles estimated according to the equation: $d_{pore} = 2\varepsilon d_{particle}/3(1-\varepsilon)$, are summarized in Table 5.1.

Table 5.1: Expected pore diameter in frits made with different sized particles assuming porosity of 0.35 for packed frit beds.

Particle diameter (nm)*	**Pore diameter (nm)**
2000	718
1000	359
690	248
500	179
300	108

*The particle sizes (diameters) are manufacturer-defined values.

Following the above estimation, the frits for packing 690 and 500 nm particles were made with 1000 nm particles (d_{pore} = 359 nm). For packing 300 nm particles, the frit was made with packed bed segments of 500 (d_{pore} = 179 nm) and 1000 nm particles. Table 5.2 shows the combination of frits used in fabricating the porous beds of different particle sizes.

Table 5.2: Frits used in fabricating the porous beds of different particle sizes.

Particle diameter (nm)	Frits used for packing
2000	Commercial frit (0.5 μm dia pore)
1000	Commercial frit (0.5 μm dia pore)
690	Commercial frit (0.5 μm dia pore)
	+ Packed bed of 1000 nm particles
500	Commercial frit (0.5 μm dia pore)
	+ Packed bed of 1000 nm particles
300	Commercial frit (0.5 μm dia pore)
	+ Packed bed of 1000 nm particles
	+ Packed bed of 500 nm particles

Figure 5.1 illustrates a packed bed of smaller particles (300, 500 and 690 nm). 1-micron particles were used for fabricating the starting frit bed for packing these smaller particles. Once the porous bed of 1000 nm particles is formed, 0.5-micron porous frit was connected at the end of the porous bed column. Then, methanol was flowed through it to remove any bulk and absorbed water molecules from the silica surface. After that, nitrogen gas was flowed at high pressure (1000-1500 psi) to expel the methanol content from the column. Thus, the packed column was made dry enough to be readily wet by the water solvent of silica colloidal solution. Then, the empty end of the packed column was immersed into the silica colloidal solution of smaller particles.

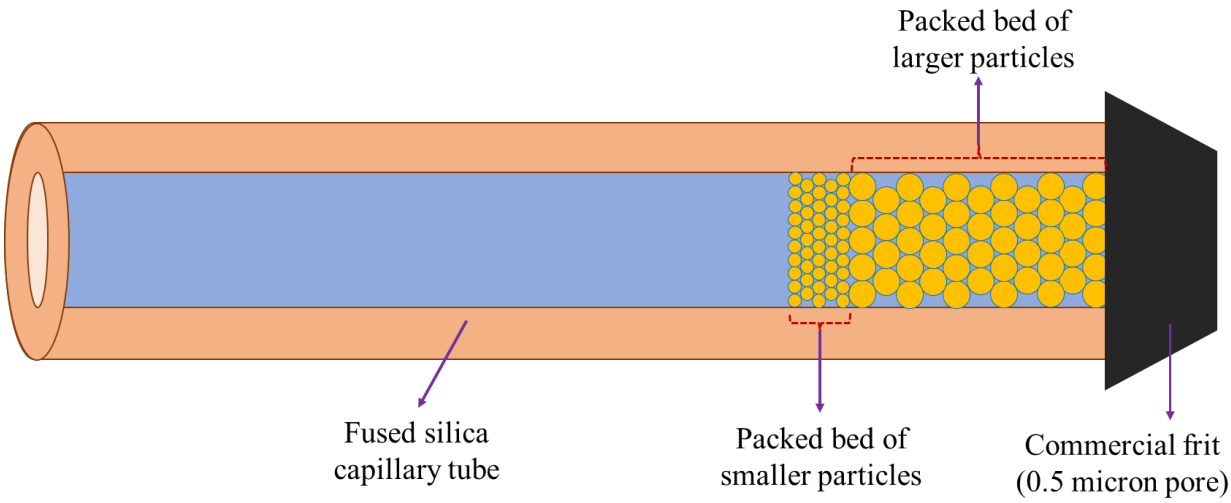

Figure 5.1: An illustration of the packed bed made with smaller particles (300, 500 and 690 nm).

A small volume of silica solution was wicked into the column by capillary action. Then, this end of the column, partly filled with the silica solution, was immersed into ultra-pure water to enter the column by capillary force and push the silica solution further inside the column. After that, ultra-pure water was flowed through the column to assemble smaller silica particles into a colloidal crystal form on the surface of 1000 nm particles' packed bed. The water flow pressure was constantly raised with an increased level of compaction of smaller packing particles. Once two packed bed segments merged into a single-phase porous bed, the pump was disengaged, and the pressure was let to decrease overnight to atmospheric pressure. Then, the column's water-filled end was sealed to let the water evaporate through the combined porous bed and silica particles to assemble into a dry colloidal crystal form.

5.2.4 Characterization of porous media and its flow properties

The porous media flow properties of the packed bed of smaller particles were determined in several steps of flow measurements, rinsing and fabrication (shown in Figure 5.2). For example, the flow properties of n-octane in a packed bed of 500 nm particles were measured with the following steps discussed below. First, the pressure-driven flow measurements for both water and n-octane were performed in the fluidic unit, excluding any porous bed to determine the pressure drops expected from the fluidic unit, including frit, restrictor, empty capillary columns stainless steel tubes. Then, the length of the pre-prepared porous bed of 1000 nm was measured using a micrometre. Then, the column of the porous bed was attached to the fluidic unit for the pressure-driven water flow measurements. A 190 nM aqueous fluorescein solution was flowed through the packed bed. After the bed was saturated with the fluorescein dye solution, photobleaching and fluorescence detection were started. The time-of-flight velocity measurements for water flow were performed at different pressure settings. Then, the porosity of the silica porous bed (1000 nm) was calculated from the slope of pressure vs velocity graph following the Kozeny-Carman equation.

After characterizing the porous bed, n-octane flow experiments were performed with the same experimental setup. At first, the whole fluidic setup was rinsed with several fluids to condition the fluidic unit for n-octane flow experiments. Next, a stream of ultrapure water was charged to rinse all fluidic channels, including the porous bed (1000 nm), to remove fluorescein dye particles (water-soluble). Then, helium gas was flowed at high pressure (1000-2000 psi) to exclude any bulk water from the fluidic system.

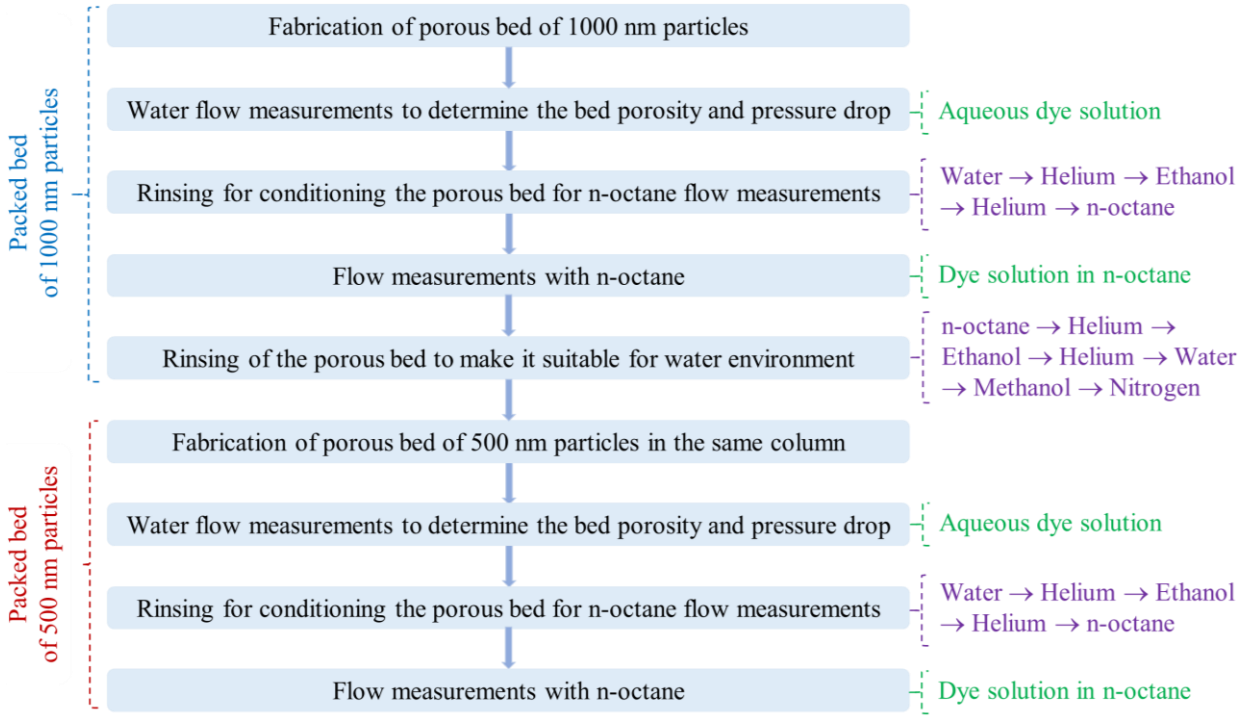

Figure 5.2: Sequential steps of porous bed fabrication, rinsing and flow measurements.

Ethanol, the intermediate rinsing fluid between water and n-octane, was pressurized with helium gas to flow through the fluidic system to remove any absorbed water on silica surfaces of the capillary column and porous bed. Thus, water was removed entirely. Later, helium gas (alone) and then fresh n-octane were charged to eliminate the ethanol in bulk amount followed by absorbed ethanol layer, respectively. Then, a 150 nM nile red (in n-octane) solution, saturated with oxygen to assist in dye photobleaching, was loaded into the fluidic channels.

A similar strategy of photobleaching, detection and data collection applied in water flow measurements was utilized for n-octane flow measurements. Temperatures of both water and n-octane were constantly monitored during the flow measurements to decide the value of viscosity

of liquids with respect to the instantaneous temperature of the flow experiment. Thus, the expected pressure drop for n-octane flow in 1000 nm particles' porous bed was determined. Then, the whole fluidic unit, including the porous bed (1000 nm), was rinsed with several fluids in the order of n-octane, helium gas, ethanol, helium gas, water, methanol, and nitrogen gas to recondition for the water environment.

After the above measurements and procedures, 500 nm particles were packed into this porous bed of 1000 nm particles, following the method mentioned above (section 5.2.3). Once the packed bed of 500 nm particles was formed, the third set of flow measurements with water and n-octane was performed. Finally, the combined pressure drop that arose in the fluidic unit (having restrictor, frit and detection column) and packed bed of 1000 nm for a particular flow rate was subtracted from the applied pressure. Thus, the actual pressure required to maintain that flow rate in the porous bed of 500 nm particles was determined according to the following equation:

$$(\Delta P_{actual})_{500nm} = (\Delta P_{applied})_{500nm} - \left(\Delta P_{1000nm} + \Delta P_{\text{fluidic unit excluding any porous bed}}\right) \text{.....(5.1)}$$

Water flow experiments give the measure of the porosity of the porous bed of 500 nm particles. First, the total length of the combined porous bed was measured by a micrometre. Then, this length was subtracted from the initial length of the porous bed (with 1000 nm particles) to determine the actual length of the porous bed of 500 nm. Next, with the known porosity value and length of the porous bed, the theoretical (Kozeny-Carman) velocities versus pressures for n-octane flow in a packed bed of 500 nm particles were determined. Then, it was compared to the

experimentally obtained result to determine the existence of slip or no-slip flow and the extent of flow enhancement. The same procedures were followed for studying the flow properties of the packed beds made of other particles.

5.3. Theory

In this chapter, the following four equations were used for the calculations. Equation 3.1 was used to determine the porosity (ε) of the packed bed with water flow measurements and the theoretical estimation of n-octane flow rates at no-slip boundary conditions for both fluids. Equation 4.5 was used in the determination of the average pore radius (r_{pore}) for a particular packed bed. Equation 4.21 was used for the determination of flow enhancement factor (E) from the ratio of the slopes obtained from the experimental (slip flow) and theoretical velocity (no-slip flow) curves. Equation 4.23 was used for the determination slip length (L_s).

$$v\eta = \frac{d_{particle}{}^2 \varepsilon^3}{180(1-\varepsilon)^2}\left(\frac{\Delta P}{L}\right) \quad \text{(3.1)}$$

$$r_{pore} = \frac{(d_{particle})\varepsilon}{3(1-\varepsilon)} \quad \text{(4.5)}$$

$$E = \frac{Q_{slip}}{Q_{no\text{-}slip}} = \frac{v_{slip}}{v_{no\text{-}slip}} \quad \text{(4.21)}$$

$$L_s = \frac{r_{pore}}{4}(E-1) \quad \text{(4.23)}$$

5.4. Results and discussion

The linear flow rates of water through the porous beds were measured at first. The temperature of water measured during velocity measurements was utilized to select the viscosity of bulk water [131]. The viscosity of water is constant within the applied pressure range of our experiments [132]. Therefore, water is a Newtonian fluid. Moreover, the contact angle of water on silica surface is 11° [133]. Hence, water can be considered a wetting fluid for the silica surface, and it can be assumed that the flow of water through the silica porous beds follows the no-slip boundary condition. Then, the pressure-driven flow measurements of water through silica porous beds give the measure of bed porosities according to equation 5.2. The value of porosity (ε) and average pore radius of porous beds for each particle diameter are listed in Table 5.3.

Table 5.3: Summary of porosity and pore size for each particle diameter.

Particle size (nm)*	Porosity, ε	Pore radius (nm)**
300	0.284 ± 0.003	39.7 ± 0.5
500	0.297 ± 0.002	70.4 ± 0.7
690	0.325 ± 0.004	110.7 ± 2.1
1000	0.329 ± 0.003	163.4 ± 2.0
2000	0.337 ± 0.001	338.9 ± 0.9

*The particle sizes (diameters) are manufacturer-defined values.

**The standard deviation (Δr_{pore}) in the pore radius was calculated by equation: $\Delta r_{pore} = \left(\frac{\Delta\varepsilon}{\varepsilon} \times 1.4\right) \times r_{pore}$, where $\Delta\varepsilon$ is the standard deviation in porosity.

The porosity value ranges from 0.284 (± 0.003), for the smallest particles (300 nm), to 0.337 (± 0.001) for the largest particles (2000 nm). For mono-sized sphere packing in the same bed diameter range, the smaller particles make the porous bed densely packed with low porosity [83]. The value of bed porosity usually varies from 0.26 (for the smallest particles with face-centred cubic or hexagonal closed packing structure) to about 0.4 (for larger particles with random packing density). Theoretically, the porosity of the body-centred cubic closed packing (BCC) is 32%, and that of the hexagonal (HCP) or face-centred cubic (FCP) closed packing is 26% [26]. The porosity of packed beds of 690 and 1000 nm particles is close to 32%. Therefore, the packing order in these particles' beds resembles mostly body-centred cubic closed packing. On the other hand, the packed beds of smaller particles (300 and 500 nm) have porosity a little above 26%. Therefore, the packing order in the packed beds of smaller particles (300 and 500 nm) resembles mostly HCP or FCP, although they may also be a mixture that includes some BCC. Columns can show different values of porosity, indicating some differences in packing structure or possible defects. Each data set for the organic solvent was normalized relative to the behaviour for water for that specific column. If there are minor column differences, they should affect solvents the same way. By normalizing, the impact of minor differences on interpretation of observed flow rates is minimized.

Figures 5.3 to 5.7 show the linear flow velocity data for porous beds of five different particle sizes. The y-axis represents the linear flow velocities normalized for the viscosity of liquids so that water and n-octane flow can be compared, and the x-axis represents the pressure gradient, i.e., the pressure applied for the flow divided by the length of the porous bed. The

temperature of liquids was monitored during the flow measurements to allow ready determination of viscosity values for water [131] and n-octane [134-136]. The flow versus pressure plot for each particle size was found linear. A higher flow velocity was observed for the n-octane flow through all silica porous beds compared to its theoretical velocity.

The porous bed having the largest pore radius (338.9 ± 0.9 nm) shows negligible slip flow, where the flow enhancement is only 1.19 ± 0.03. The porous beds of intermediate-sized particles (690 and 1000 nm) with body-centred cubic packing order show a greater extent of slip flow. The porous bed of the smallest particles (300 nm) with a pore radius of 39.7 ± 0.5 nm shows the maximum extent of slip flow.

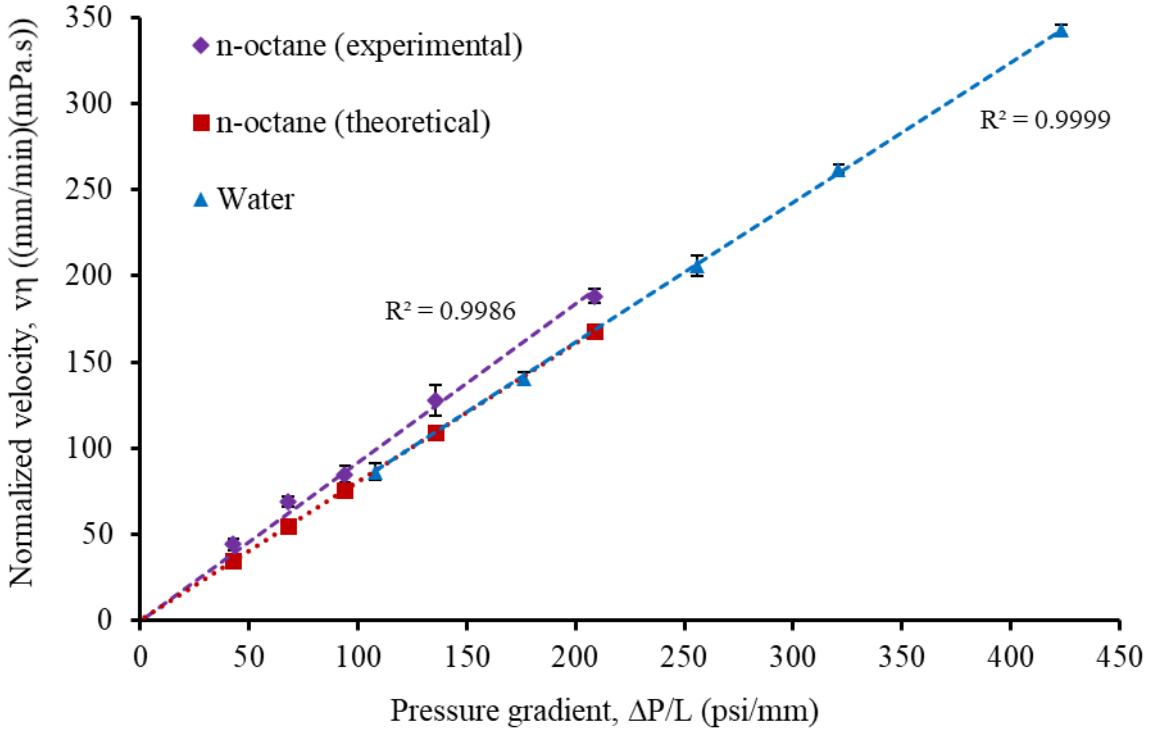

Figure 5.3: Variation of linear velocity with pressure gradient for water and n-octane flow in a porous bed (L = 2.24 mm , ε = 0.337) of 2000 nm silica microspheres. Velocities were normalized for viscosities of water (0.931 mPa.s) and n-octane (0.556 mPa.s) at 23°C.

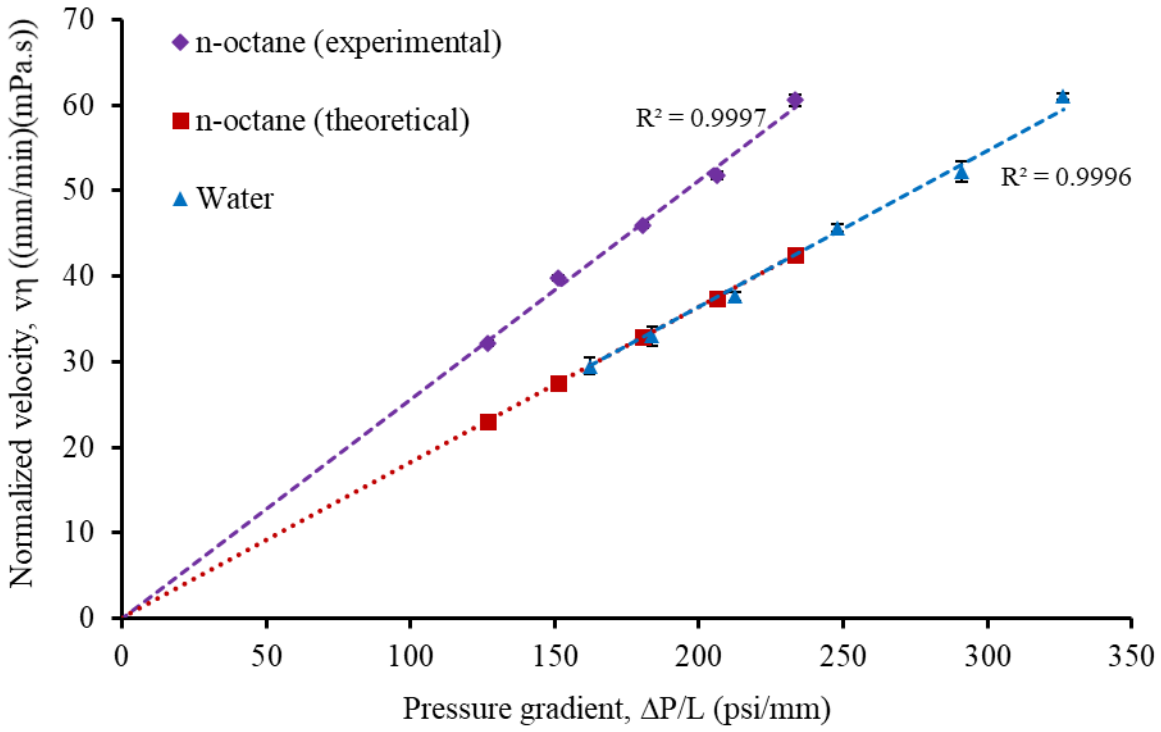

Figure 5.4: Variation of linear velocity with pressure gradient for water and n-octane flow in a porous bed (L = 4.25 mm, ε = 0.329) of 1000 nm silica microspheres. Velocities were normalized for viscosities of water (0.9266 mPa.s) and n-octane (0.555 mPa.s) at 23.2°C.

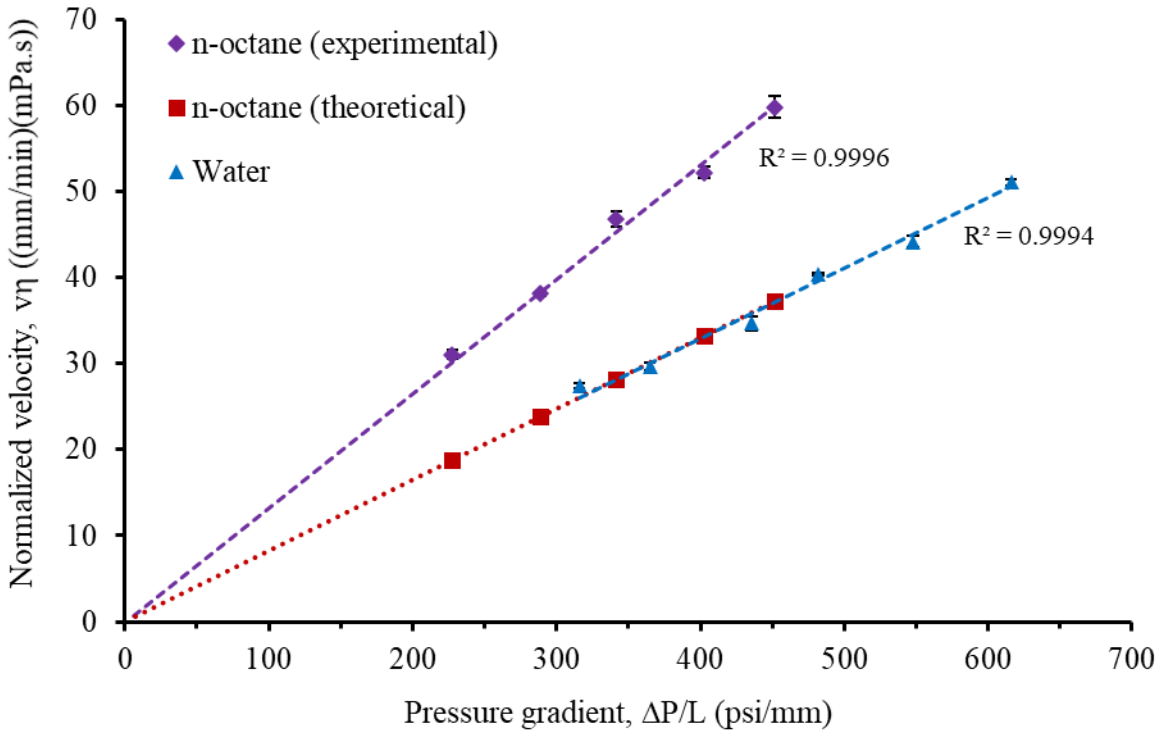

Figure 5.5: Variation of linear velocity with pressure gradient for water and n-octane flow in a porous bed (L = 3.2 mm, ε = 0.325) of 690 nm silica microspheres. Velocities were normalized for viscosities of water (0.9266 mPa.s) at 23.2°C and n-octane (0.553 mPa.s) at 23.5°C.

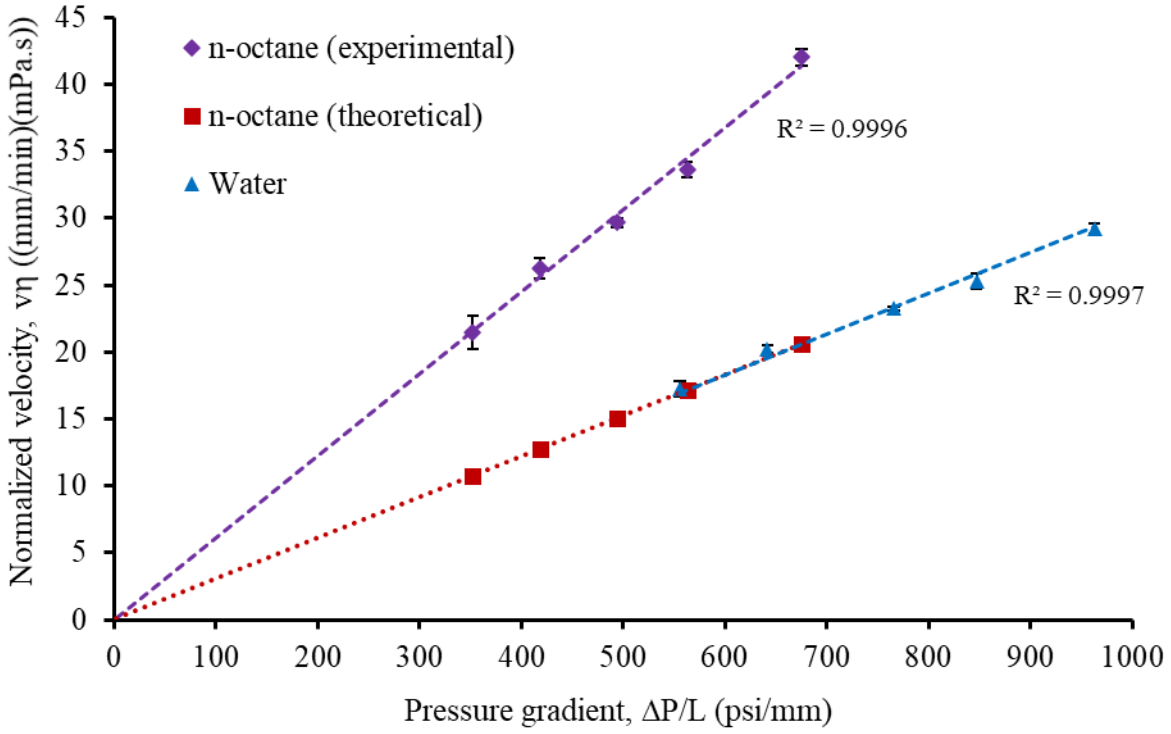

Figure 5.6: Variation of linear velocity with pressure gradient for water and n-octane flow in a porous bed (L = 1.82 mm, ε = 0.297) of 500 nm silica microspheres. Velocities were normalized for viscosities of water (0.9266 mPa.s) at 23.2°C and n-octane (0.557 mPa.s) at 22.9°C.

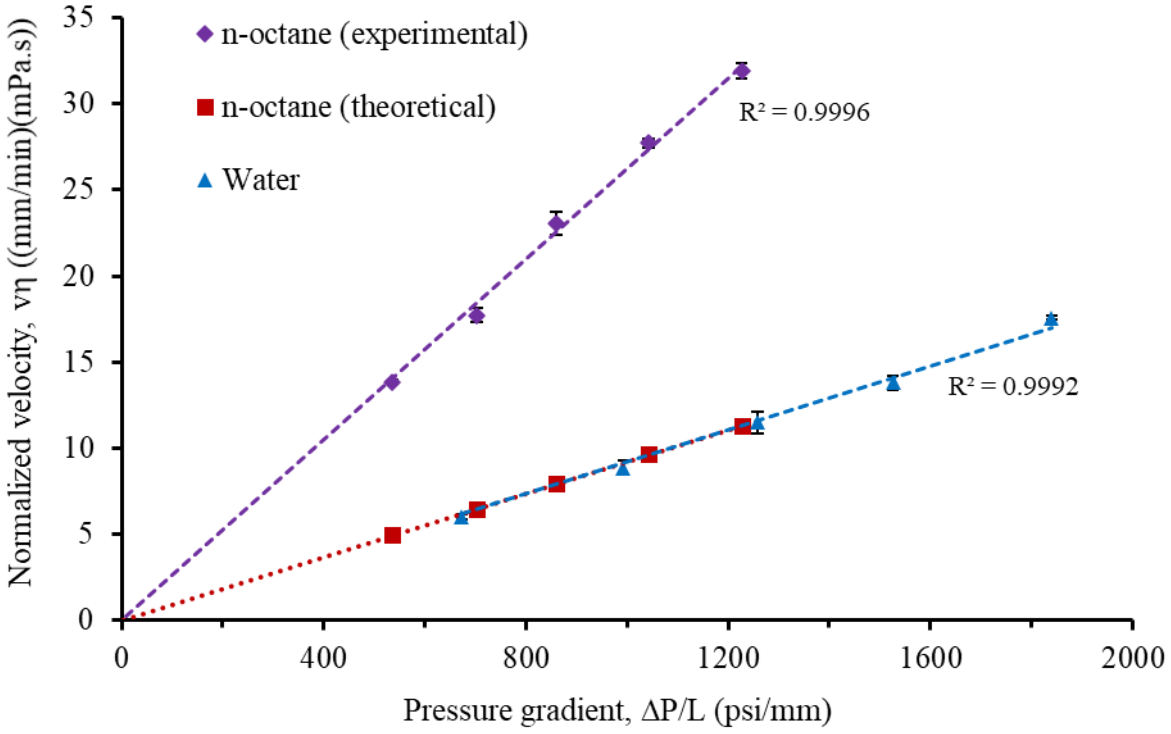

Figure 5.7: Variation of linear velocity with pressure gradient for water and n-octane flow in a porous bed (L = 0.91 mm, ε = 0.284) of 300 nm silica microspheres. Velocities were normalized for viscosities of water (0.9266 mPa.s) at 23.2°C and n-octane (0.554 mPa.s) at 23.4°C.

Figure 5.8 shows a plot of the variation of flow rate enhancements for n-octane with the pore size of the silica porous bed. The flow enhancement factor for n-octane flow was calculated by taking the ratio of slopes obtained from the experimental and theoretical pressure vs velocity graphs. The highest flow rate enhancement (2.82 ± 0.15) was observed from the porous bed with the smallest pore radius of 39.7 ± 0.5 nm. The porous bed prepared from the smallest particles

(300 nm diameter) gives 2.37 times higher flow enhancement than that prepared from 2000 nm diameter particles.

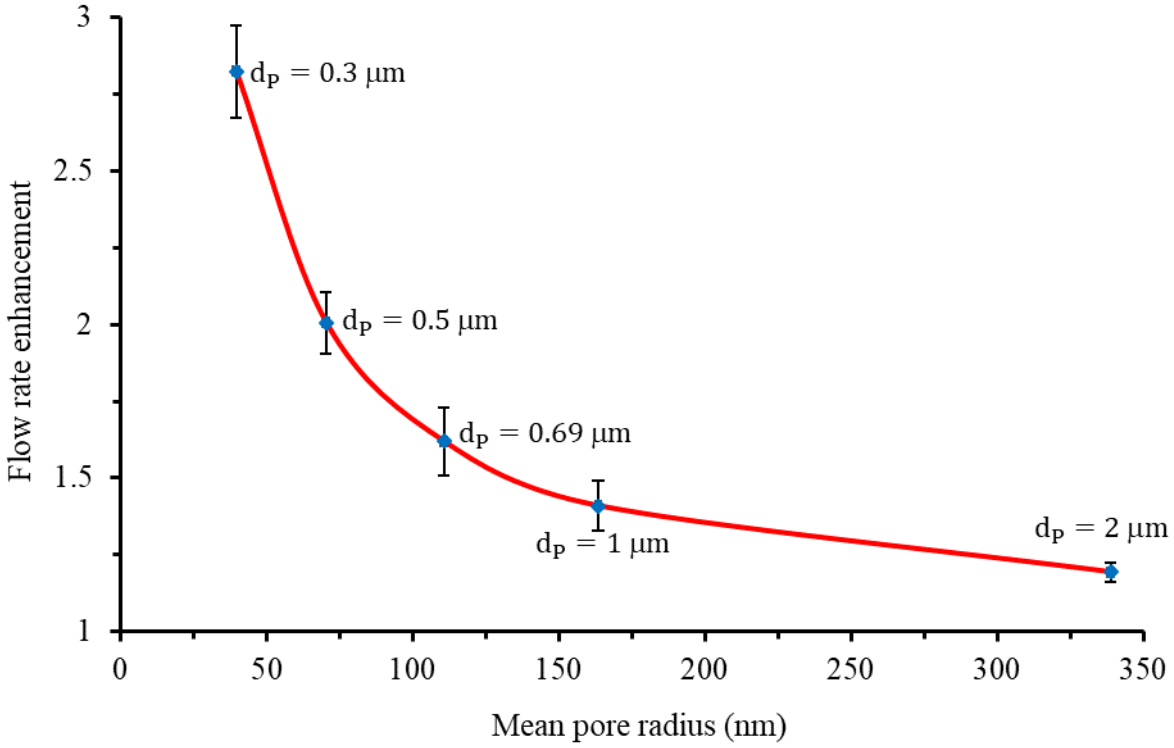

Figure 5.8: Variation of flow rate enhancements for n-octane with the pore size of the silica porous bed. At each pressure, flow enhancement was calculated, and then the average and standard deviation of flow rate enhancement for a particular porous bed were calculated. The error bars represent the standard deviations.

The slip length, which is a measure of the extent of flow rate enhancement, was calculated from the values of pore radius and flow enhancement factor. The slip length ranges from 16.4 (± 0.4) to 18.1 (± 1.0) nm, having an incrementally increasing trend with decreasing pore sizes

(shown in Table 5.4). The silica porous bed having the smallest pore radius (39.7 ± 0.5 nm) gives the maximum extent of slip or flow rate enhancement, where the slip length is 18.1 ± 1.0 nm for the n-octane flow.

Table 5.4: Summary of flow rate enhancement and slip length with respect to pore radius.

Particle size (nm)*	Pore radius (nm)	Flow enhancement**	Slip Length (nm)***
300	39.7 ± 0.5	2.82 ± 0.15	18.1 ± 1.0
500	70.4 ± 0.7	2.01 ± 0.10	17.7 ± 0.9
690	110.7 ± 2.1	1.62 ± 0.11	17.1 ± 1.3
1000	163.4 ± 2.0	1.41 ± 0.08	16.8 ± 0.9
2000	338.9 ± 0.9	1.19 ± 0.03	16.4 ± 0.4

*The particle sizes (diameters) are manufacturer-defined values.

**The standard deviation in the flow enhancement was calculated by equation: $\Delta E = \left(\frac{E_{average}}{100}\right)\sqrt{(\text{RSD in slope}_{\text{slip curve}})^2 + (\text{RSD in slope}_{\text{no-slip curve}})^2}$

***The standard deviation in the slip length was calculated by equation: $\Delta L_s = \left(\frac{L_s}{100}\right)\sqrt{(\text{RSD in r}_{\text{pore}})^2 + (\text{RSD in E})^2}$

Packed beds prepared with the same particle size may have slight differences in porosity values, as observed in Chapter 3. In addition, if the organic solvent does not wet all the interstitial silica surfaces, we expect that there would be variable slip lengths between columns. However, when we compare the slip flow results between columns packed with the identical particles, the differences were less than 10 % RSD. Moreover, air pockets or gas trapped within the porous bed would give us a measure of the lower limit of slip length; thus, this possibility does not invalidate the flow enhancements that we observed. However, there are chances that the silica surface may become contaminated by the dye molecules through surface adsorption, but that is not enough to change the surface into a hydrophobic state. Some trace levels of water molecules may still be present in the interstitial spaces, even after following thorough rinsing procedures. Still, the overall silica surface would remain hydrophilic.

The value of slip length depends on both pore radius and flow enhancement. The slip length increases even though pore radius decreases, which suggests that both nanochannel effect and weak fluid-wall surface interaction contribute to higher flow rate enhancement. Literature shows that increasing the shear rate can cause a linear increment of slip length [137]. Since the non-zero velocity at the wall increases the overall shear rate, the effective viscosity (ratio of shear stress to shear rate) of bulk n-octane reduces in the porous media resulting in a higher flow rate.

The increasing trend of flow enhancement and slip length with the decreasing pore radius resembles the theoretical predictions mentioned in the literature [138, 139]. However, a molecular dynamics study of n-octane flow through quartz nano slits (1.7 to 11.2 nm) predicted

a slip length of ~0.9 nm [20], which is about 20 times smaller than our experimentally obtained slip length value (for the smallest pore size). Moreover, a Lattice Boltzmann simulation of octane flow in a quartz nanoporous media showed that the flow enhancement factor achievable through a 5.24 nm quartz nano-slit is 2.366 [140]. However, we obtained a greater extent of slip flow (E = 2.82 ± 0.15) even for a larger pore dimension (39.7 ± 0.5 nm pore radius).

In both of the above theoretical studies, quartz was used as the solid surface of the pore structure. Quartz is a mineral containing mainly silica, with other minerals. It consists of a crystalline structure of silicon tetrahedrons with helix chains having less –OH group on its surface than amorphous silica [141, 142]. Therefore, n-octane is expected to wet quartz more than a pure silica surface, resulting in minor flow enhancement with lower slip length when compared to the amorphous silica used in our study. Moreover, a nano-slit was used as the model in the theoretical studies instead of a porous media. It may also be clear that the porous packed bed is a more suitable model for transport in fractured geological materials than a single nano-slit will be.

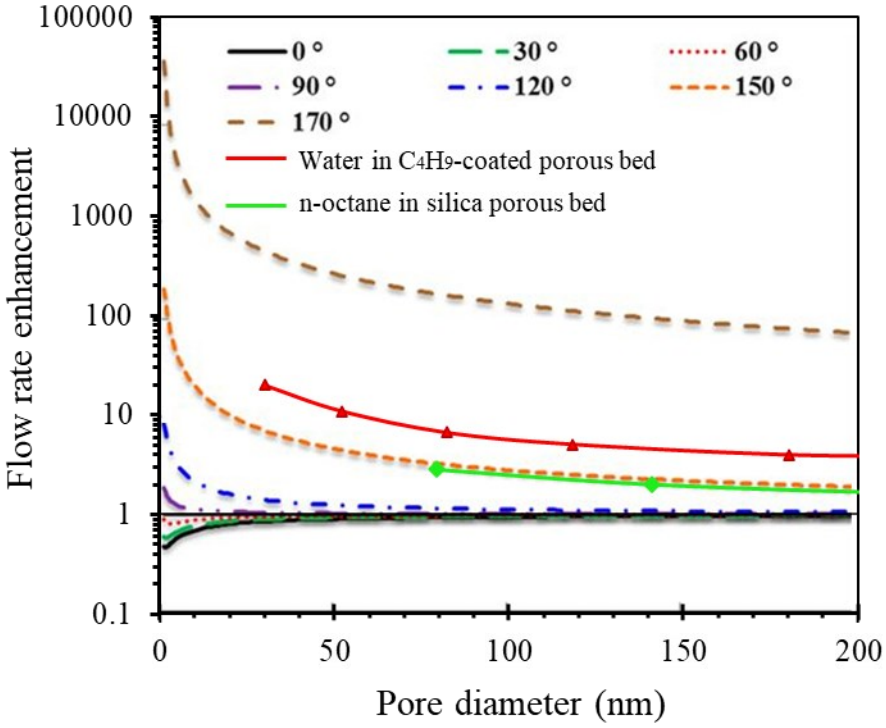

Figure 5.9: Variation of flow rate enhancements with the pore size in different wettability conditions (reprinted from the literature with permission [85]). The solid green and red trendlines represent the flow enhancement results obtained from this study and the literature article published by Rogers et al. [26], respectively, within 0-200 nm pore diameter range.

Keliu Wu et al. [84, 85] drew a summary of the dependence of water flow enhancement on pore size for different values (contact angle) of wettability (as shown in Figure 5.9), based on the combination of theoretical analysis and experimental and MD simulations data found in the literature. For a comparative analysis, the flow enhancement results obtained experimentally in this study and from the article of Rogers et al. [26] have been merged into the plot mentioned above (Figure 5.9) as a function of pore diameter. The solid green trendline represents the flow

enhancement of n-octane in a silica porous bed (our study), whereas the solid red trendline represents the flow enhancement of water in C_4H_9-coated porous bed (drawn based on the data available in the literature [26]). We do not have a measured contact angle value for n-octane on a porous silica surface. However, based on the hydrophobic character of n-octane on a silica surface, we are assuming the contact angle, in this case, is between 90 to 120°, while water on the C_4H_9-coated surface had an angle of 83° [26].

The graphical comparison shows that the flow enhancement trendline (obtained from our study) closely follows the one that was predicted for a superhydrophobic liquid (150° contact angle). The flow enhancement of water observed in the C_4H_9-coated porous bed was about 2 times higher (for ~80 nm pore diameter) than our result, and even higher than the predicted results for a 150° contact angle liquid, despite a low water contact angle (83°) [26]. The overall comparison indicates that theory is predicting a lower extent of slip flow than the experimental results. The comparison of experiment to Wu et al is in agreement with the comparison discussed above for the difference between our experimental results and the molecular dynamics and Lattice Boltzmann simulation results for n-octane flow in silica based pore systems.

McBride et al. [143] experimentally studied the slip behavior of n-octane (along with other hydrocarbons and alcohols) on a molecularly smooth n-hexadecyltrichlorosilane (hydrophobic) coated surface using colloidal probe atomic force microscopy (AFM) technique and reported a slip length value of ~10 nm for n-octane. In contrast, the slip length of n-octane flow in silica porous beds obtained in this study ranges from 16.4 to 18.1 nm. n-octane is more

non-wetting in nature on a hydrophilic silica surface compared to a hydrophobic n-hexadecyltrichlorosilane coated surface. Therefore, this ~2 times higher slip length difference between our results and that obtained from the colloidal probe AFM study is in reasonably good agreement, in contrast to the theoretical predictions discussed above. We also note an experimental study by Majumder et al in 2005 [28] showing about four to five orders of magnitude higher flow rate enhancements were achieved for water, hexane, decane and ethanol flows through membranes of aligned multiwall carbon nanotubes (MWCNTs) having 7.0 nm pore diameter.

In summary, most experimental results in the sub-micron pore size range are in disagreement with theoretical predictions, in terms of magnitudes, although the trend with pore size appears consistent between experiment and theory. Clearly, experimental data will be useful for the future refinements of theory.

5.5. Conclusion

The increase of flow enhancement with respect to decreasing pore size, as observed in this study, agrees with both theoretical and experimental observations in direction. Though the magnitude of flow enhancement obtained in this study disagrees with the theoretical predictions, there is reasonable agreement with other experimental results, even though the systems are not identical [143]. The presence of slip flow in the packed bed of smaller particles can be advantageous for the UHPLC system by reducing the high-pressure requirement for fluid flow. In addition, the measurement approach provides high-quality data sets for a variety of conditions

of pore radius, providing a strong basis set for future refinement of theoretical models. It should also be a useful method to evaluate multi-phase flow in nano-porous media.

Chapter 6: Transport of Highly Viscous Fluid (1-Octanol) through Porous Media

6.1. Introduction

In our previous studies (shown in chapters 4 and 5), we have found that slip flow occurs for n-octane flow through silica micro- or nanoporous media, and the porous bed having the smaller pore size shows the maximum extent of flow rate enhancement. On the other hand, water, a wetting fluid for silica porous-bed, shows no-slip flow, even in the small nanopore system. However, the flow characteristics of a much more viscous liquid like 1-octanol through low permeable porous media have not been reported yet. 1-octanol is about 14 times more viscous than n-octane, although 1-octanol has the same length of straight alkyl chain (C_8H_{17}-) in its structure as n-octane. In addition to the non-polar octyl group, 1-octanol has a polar hydroxyl moiety. Here, we report how the flow characteristics of 1-octanol, which has both wetting (hydroxyl group) and non-wetting (octyl group) parts for silica surface, change with the varying pore sizes in silica micro- and nanoporous media.

6.2. Experimental

6.2.1 Materials

Different sizes (300, 500, 690, 1000 and 2000 nm diameter) of silica particles were used for packing inside a fused silica capillary tube (TSP100375, Polymicro Technologies, Molex).

As fluorescence tracing dyes, nile red (Millipore Sigma) and fluorescein disodium salt (Sigma, St. Louis, MO) were used. Helium gas (>99.998% purity, Praxair Canada Inc., Mississauga) was used for pressurizing dye solutions to get a constant pressure liquid flow. O_2 gas (Praxair, Mississauga, ON, Canada) was used to prepare a photo-bleachable oxygen-saturated dye solution. Ultrapure water and 1-octanol (Sigma-Aldrich) were used as solvents.

6.2.2 Fabrication of packed porous bed

The packed porous beds were fabricated from silica particles (different sizes) using the same process discussed in Chapter 5. Details are mentioned in section 5.2.2.

6.2.3 Instrumentation and determination of linear flow velocity

A time-of-flight photo-bleaching velocity measurement technique (described in detail in Chapter 2) was used here. Figure 6.1 illustrates the fluidic and optical setup for velocity measurement. First, 1-octanol kept in a liquid reservoir was flowed through the porous bed by a constant pressure pump system. A gas cylinder (helium) and regulator were used to deliver the 1-octanol at constant pressure. A pressure transducer was used to monitor the pressure drop across the device relative to the atmosphere. 1-octanol flowing out from the porous bed was then carried through a sample injection valve to the detection column followed by an empty capillary having the same ID (97.5 μm) as the porous bed column. The sample injection valve (NanoPeak 10-Port Valve; V-472-1; Upchurch Scientific, Oak Harbor, WA, USA) consisted of ten ports with two injection loops. However, we utilized only six ports (1 to 6), engaging only one sample loop. The

sample loop was custom-built by connecting a fused silica capillary tube (10 cm × 252 μm ID × 360 μm OD) between port positions 2 and 5.

During the load mode in the injection valve, an aqueous fluorescein disodium salt dye solution was loaded through a capillary tube (97.5 μm i.d. × 360 μm o.d.) on port-4 by a syringe pump (Harvard Apparatus PHD 2000, Massachusetts, U.S.A.), and then carried through the sample loop (2→5) to the waste port-3. At the same time, 1-octanol flowing out from the porous bed travelled through ports 1 to 6 and then entered the detection column. During the load mode in the injection valve, the whole fluidic channel was thus filled with 1-octanol. At the inject mode of the valve, a stream of 1-octanol carried the dye plug (contained in the sample loop) through ports in the sequence of 1→2→5→6 to the dual-point velocity detection column. The dye solution plug volume in the detection column was sufficient to complete several velocity measurements with a single sample injection. Moreover, during the detection, both upstream and downstream of the aqueous dye solution plug the column contained 1-octanol (as shown in Figure 6.1B), which ensured a constant pressure drop in the detection column.

The dye solution plug flowing with the average velocity of 1-octanol flow through the porous bed was photo-bleached downstream by a chopper-modulated high-intensity laser beam to generate a square wave dye concentration variation. The time of flight of the photo-bleached plug was then determined at two different detection zones downstream of the bleaching site by laser-induced fluorescence detection.

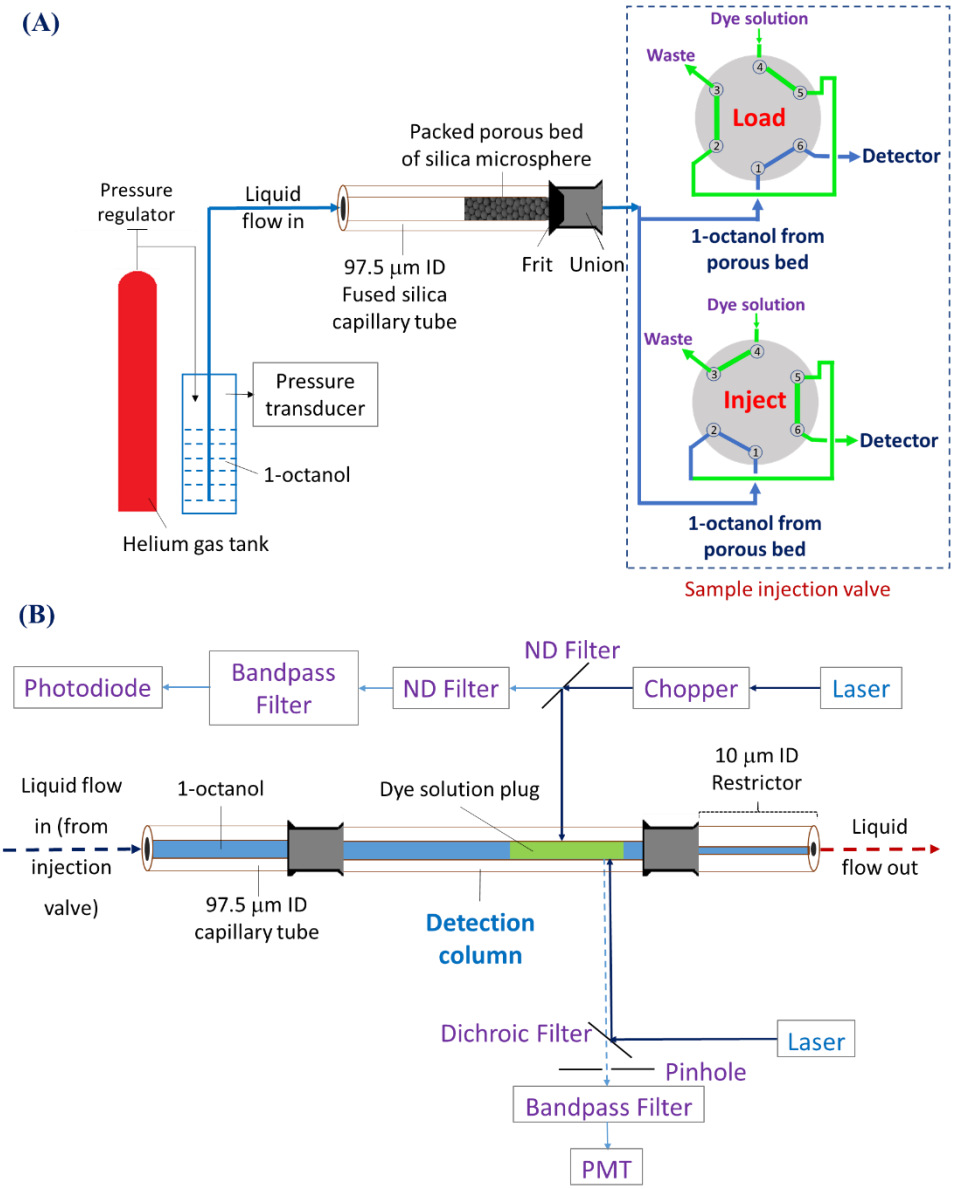

Figure 6.1: Instrumental setup for the determination of linear flow velocity (A) A constant pressure pumping unit connected to silica packed bed column coupled with a dye solution injection (6-port valve) unit (B) An optical detector unit for dual point flow velocity measurement by following the equation: $v = \frac{L_2 - L_1}{t_2 - t_1}$. Here, t_1 and t_2 correspond to the times required for the bleached zone to reach the first and second detection zones, respectively.

6.2.4 Characterization of porous media and its flow properties

The same strategy and steps discussed in Chapter 5 (section 5.2.4) for characterizing the porous bed and determining the flow properties were followed here. The only exception is that the porous media flow properties were determined with 1-octanol instead of using n-octane. The rinsing procedures and pressure drop corrections were the same as well, with 1-octanol substituting for n-octane.

A 190 nM aqueous fluorescein solution, saturated with oxygen, was flowed through the packed bed. The time-of-flight velocity measurements for water flow were performed at different pressure settings. Then, the porosity of the silica porous bed was calculated from the slope of pressure vs velocity graph following the Kozeny-Carman equation.

After characterizing the porous bed, 1-octanol flow experiments were performed. Temperatures of both water and 1-octanol were constantly monitored during the flow measurements to decide the value of viscosity of liquids with respect to the instantaneous temperature of the flow experiment. With the known porosity value and length of the porous bed and the viscosity of the 1-octanol, the theoretical (Kozeny-Carman) velocities versus pressures for 1-octanol flow in the porous bed were determined. Then, the experimentally obtained results were compared with the theoretical ones to determine the extent of flow enhancement.

6.3. Results and discussion

The same optical arrangement was utilized for both water and 1-octanol flow measurements. Figure 6.2 shows the fluorescence spectrums of nile red and fluorescein disodium salt dyes dissolved in 1-octanol. Since the excitation maxima for nile red dye solution in 1-octanol was found to be 562 nm, the 488 nm argon-ion laser we used would not be absorbed strongly enough to excite nile red dye molecules in 1-octanol. Moreover, the fluorescence signals (emission maxima = 614 nm) would be mostly blocked by the 530 ± 30 nm bandpass filter used in our system. That is why nile red dye, though soluble in 1-octanol, was not used for the flow measurements.

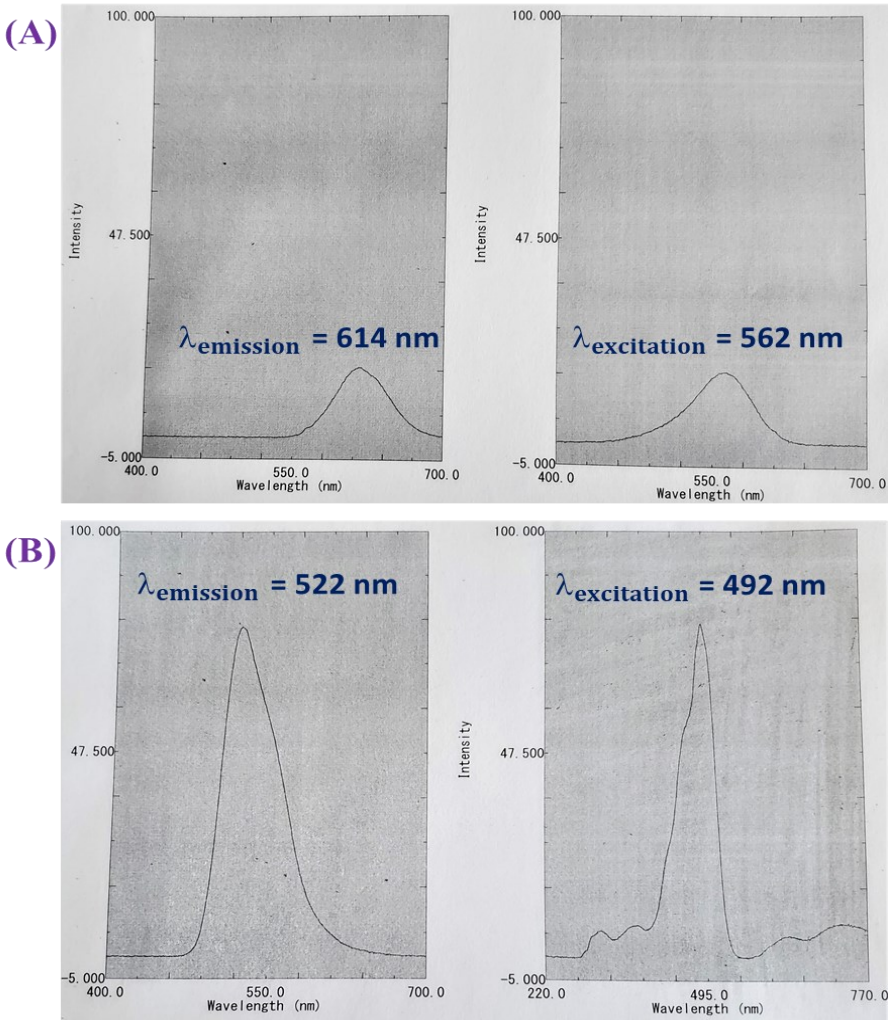

Figure 6.2: Fluorescence spectrum of (A) nile red and (B) fluorescein disodium salt dyes dissolved in 1-octanol solvent.

On the other hand, both excitation and emission maxima for fluorescein disodium salt dye dissolved in 1-octanol were found to be almost similar to an aqueous dye solution. Therefore, fluorescein disodium salt dye, soluble in water and 1-octanol, would be ideal for the flow measurements with both solvents. However, poor oxygen saturation in 1-octanol solvent made the photobleaching of dye molecules ineffective to get the square-wave dye concentration. In

these circumstances, we decided to use only aqueous fluorescein disodium salt dye solution. Similar to the chromatographic technique, a pure 1-octanol solvent was used as the mobile phase to carry a dye plug (aqueous fluorescein disodium salt dye solution as the sample) through the velocity detection column. The aqueous dye solution plug moved to the detection column with the same velocity of 1-octanol flowing out from the porous system. However, the packed bed was not exposed to the aqueous dye plug since the valve injector was downstream of the packed bed. Figure 6.3 shows a typical image of fluorescence signal obtained from an aqueous dye solution plug during 1-octanol velocity measurement. Before injecting the aqueous dye plug, the detection column was loaded with 1-octanol. Hence, once the aqueous dye solution plug was injected, both upstream and downstream of the aqueous dye plug were filled with 1-octanol during the detection. A small length of aqueous dye solution plug caused a very negligible pressure drop in the detection capillary column due to its lower viscosity than 1-octanol. Therefore, the whole liquid stream moved with a constant velocity across the detection column.

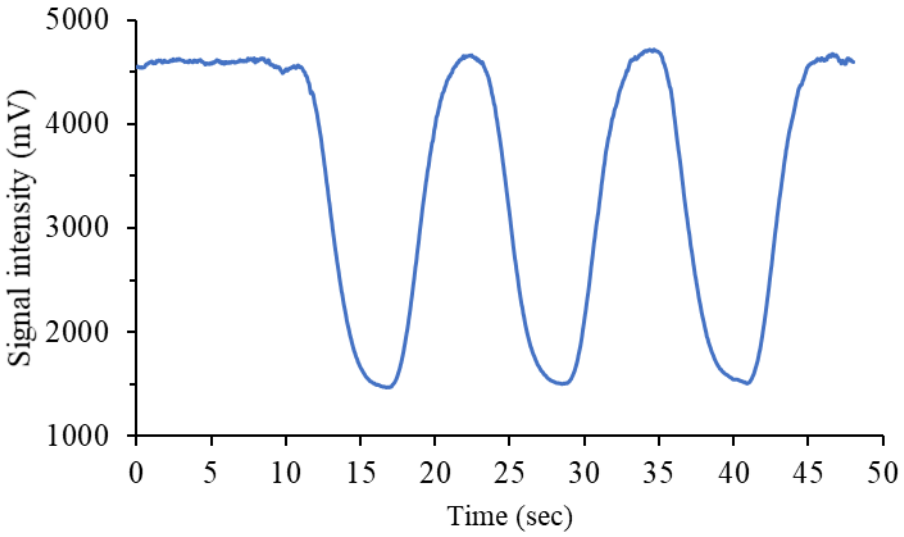

Figure 6.3: Fluorescence signal obtained from an aqueous dye solution plug during 1-octanol velocity measurement.

Varying sizes (300 to 2000 nm) of silica particles were used to develop the porous beds packed in the capillary tube. First, the water flow velocities through the porous beds at different pressures were measured (shown in Figure 6.4), and then the bed porosity (ε) was determined according to following equation:

$$v\eta = \frac{d_{particle}^{2}\varepsilon^{3}}{180(1-\varepsilon)^{2}}\left(\frac{\Delta P}{L}\right) \quad \text{.....(3.1)}$$

The velocity normalized with water viscosity (vη) and pressure gradient ($\frac{\Delta P}{L}$) are presented in x- and y-axes, respectively. With the known particle diameter ($d_{particle}$), the slope of the linear curve gives the measure of the bed porosity (ε). Then, the average pore radius (r_{pore}) of porous beds for each particle diameter was calculated according to the following equation:

$$r_{pore} = \frac{(d_{particle})\varepsilon}{3(1-\varepsilon)} \quad \text{.....(4.5)}$$

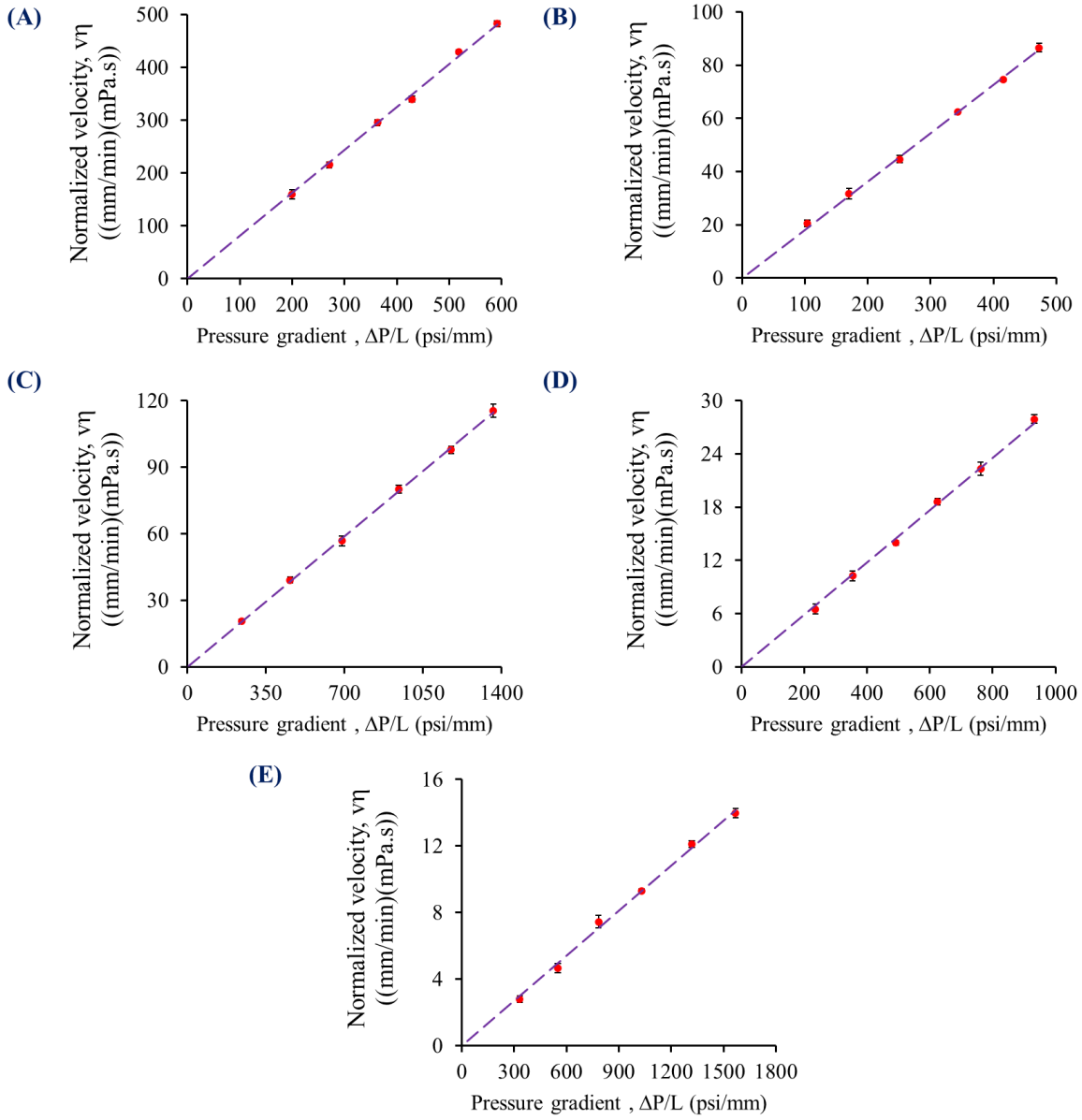

Figure 6.4: Linear flow velocity (normalized with viscosity) versus pressure gradient for water flow in the porous beds packed with (A) 2000 nm (L = 1.21 mm), (B) 1000 nm (L = 2.34 mm), (A) 690 nm (L = 0.76 mm), (A) 500 nm (L = 0.98 mm), and (E) 300 nm (L = 0.61 mm) silica microspheres.

Table 6.1 lists the length, porosity and pore size (radius) of the porous beds used in this study. The porosity value ranges from 0.283 ± 0.001, for the smallest particles (300 nm), to 0.338 ± 0.002 for the largest particles (2000 nm). Theoretically, the porosity of the body-centred cubic closed packing (BCC) is 32%, and that of the hexagonal (HCP) or face-centred cubic (FCP) closed packing is 26% [26]. The porosity of packed beds of 690 and 1000 nm particles is close to 32%. Therefore, the packing order in these particles' beds resembles mostly body-centred cubic closed packing.

Table 6.1: Summary of the length, porosity and pore size of packed beds for each particle diameter. These porous beds were used in this study for flow measurements.

Particle size (nm)*	Length of porous bed (mm)	Porosity	Pore radius (nm)**
300	0.61	0.283 ± 0.001	39.5 ± 0.2
500	0.98	0.295 ± 0.001	69.7 ± 0.4
690	0.76	0.327 ± 0.001	111.8 ± 0.5
1000	2.34	0.329 ± 0.002	163.4 ± 1.0
2000	1.21	0.338 ± 0.002	340.4 ± 2.6

*The particle sizes (diameters) are manufacturer-defined values.

**The standard deviation (Δr_{pore}) in the pore radius was calculated by equation: $\Delta r_{pore} = \left(\frac{\Delta\varepsilon}{\varepsilon} \times 1.4\right) \times r_{pore}$, where $\Delta\varepsilon$ is the standard deviation in porosity.

On the other hand, the packed beds of smaller particles (300 and 500 nm) have porosity a little above 26%. Therefore, the packing order in these columns is the mixture of BCC with HCP or FCP configurations. The pore diameter of the silica porous bed prepared from 300 nm particles is 79 nm. Hence, this bed can be considered as a nanoporous media. On the other hand, the pore diameter of other porous beds ranges from 139 to 681 nm. Therefore, a porous bed prepared from larger particles can be considered microporous media.

Figures 6.5 (A to E) show the linear flow velocity data at different pressure settings for 1-octanol flow in the porous beds of five different particle sizes. The y-axis represents the linear flow velocity, and the x-axis represents the actual pressure applied for the flow. The temperature of liquids was monitored during the flow measurements to allow ready determination of the viscosity of 1-octanol. The dynamic viscosity of 7.7517 mPa.sec for 1-octanol at the experimental condition (23.2°C) was used for the theoretical velocity calculation [144]. The flow versus pressure plot for each particle size was found to be linear. Using the known value of bed porosity and length, 1-octanol viscosity and particle diameter, the theoretical velocity was calculated according to following equation, and presented in the same graph for comparison:

$$v\eta = \frac{d_{particle}{}^2 \varepsilon^3}{180(1-\varepsilon)^2}\left(\frac{\Delta P}{L}\right) \quad \text{.....(3.1)}$$

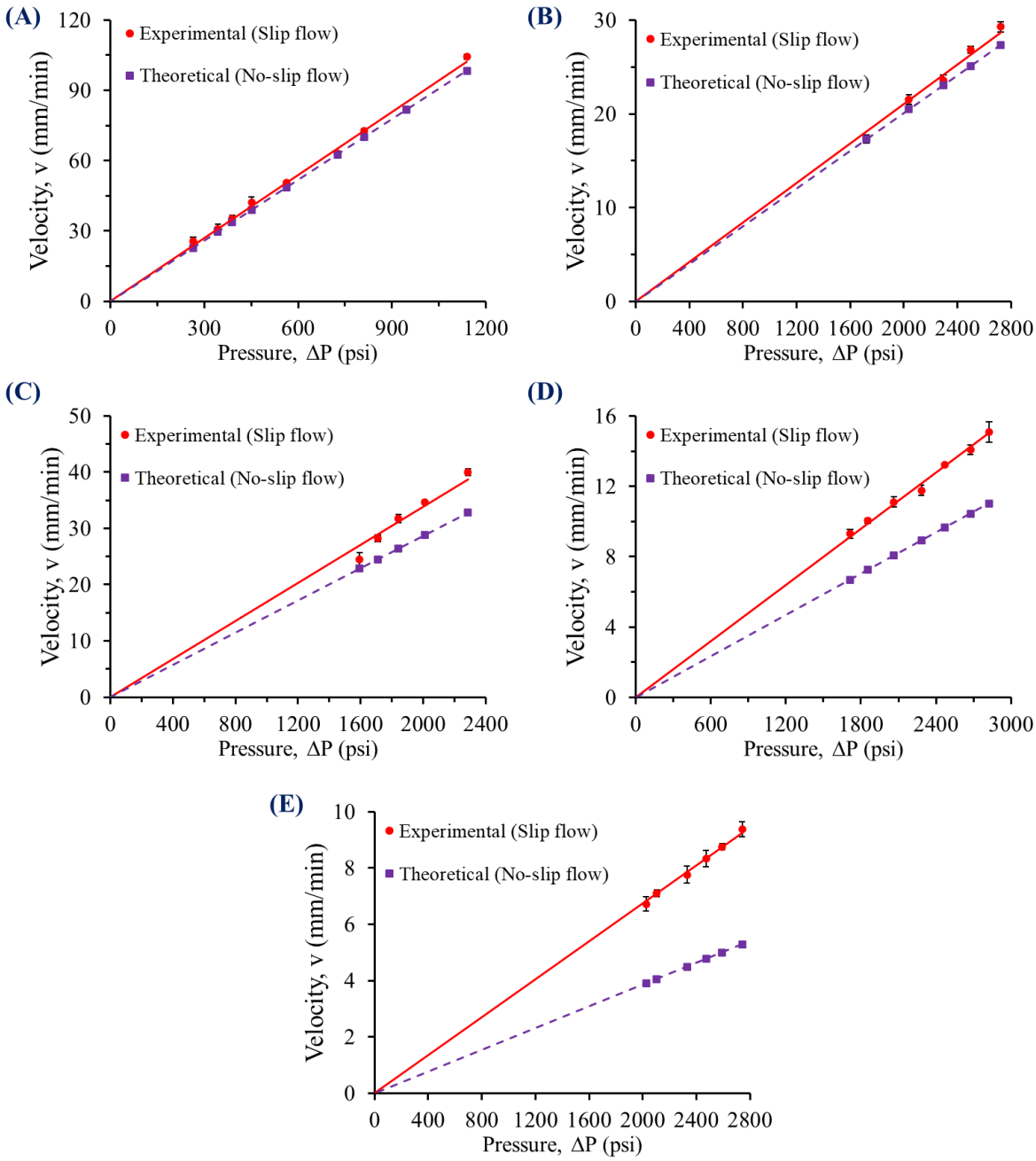

Figure 6.5: Variation of linear flow velocity with pressure for 1-octanol flow in the porous beds packed with (A) 2000 nm, (B) 1000 nm, (A) 690 nm, (A) 500 nm, and (E) 300 nm silica microspheres.

A higher flow velocity was observed for the 1-octanol flow through all silica porous beds than its theoretical velocity. However, the porous bed with the largest pore radius (340.4 ± 2.6 nm) shows minor slip or almost no-slip flow, where the flow enhancement is only 1.04 (± 0.03). The porous beds of intermediate-sized particles (690 and 1000 nm) with body-centred cubic packing order show a greater extent of slip flow, although not in a significant amount (only 12.5 to 20% flow enhancement). The porous bed of the smallest particles (300 nm) with a pore radius of 39.5 ± 0.2 nm shows the maximum extent of slip flow.

The flow enhancement factor (E) was calculated from the ratio of the slopes obtained from the experimental and theoretical velocity curves according to following equation:

$$E = \frac{v_{slip}}{v_{no\text{-}slip}} \quad \text{(4.21)}$$

Figure 6.6 shows a plot of the variation of flow rate enhancements for 1-octanol with the pore size of the silica porous beds. The flow enhancement factor for 1-octanol flow was calculated by taking the ratio of slopes obtained from the experimental and theoretical pressure vs velocity graphs. The amount of flow rate enhancement increases with the decreasing pore sizes of porous media. The highest flow rate enhancement (1.75 ± 0.07) was observed from the porous bed with the smallest pore radius of 39.5 ± 0.2 nm.

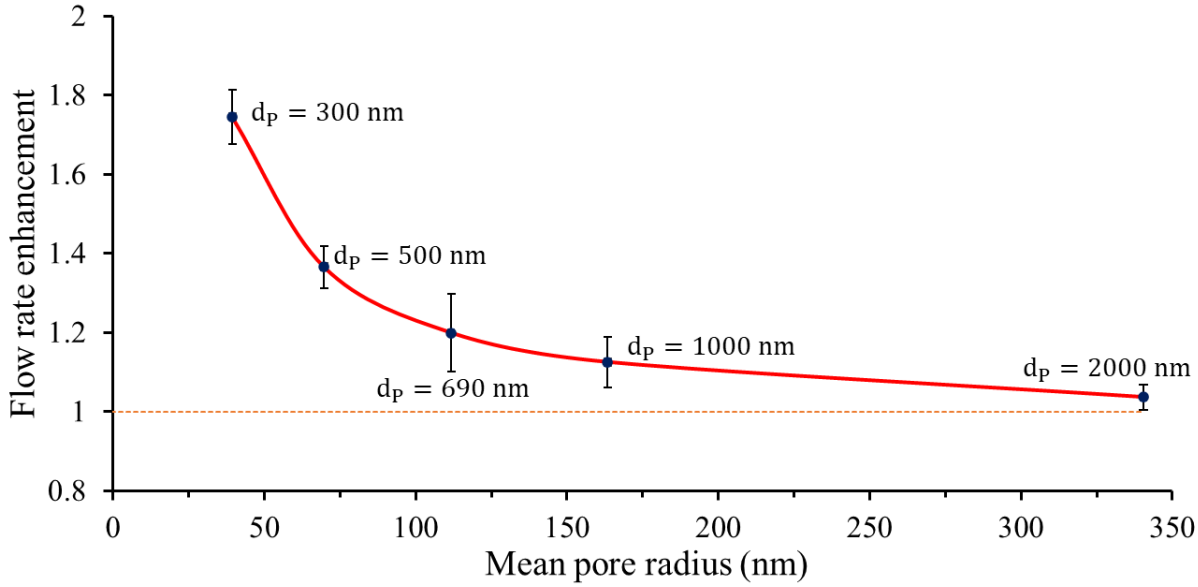

Figure 6.6: Variation of flow rate enhancement to the pore size of the porous bed.

The nanoporous media prepared from the smallest particles (300 nm diameter) gives 1.68 times higher flow enhancement than the microporous media (prepared from 2000 nm diameter particles). Therefore, the extent of slip flow for 1-octanol through silica porous media was more pronounced in the nanofluidic porous media than microfluidic porous media. The slip length, which is a measure of the extent of flow rate enhancement, was calculated from the values of pore radius and flow enhancement factor according to the following equation: $L_s = \frac{r_{pore}}{4}$ (E-1). Slip length for 1-octanol flow in these silica porous beds also increases with the decreasing pore size (shown in Table 6.2). The slip length ranges from 3.1 to 7.4 nm. Packed beds prepared with the same particle size showed a slight difference in porosity values. However, normalizing the columns' flow with porosity measured at no-slip conditions kept the effect of packing defects, gas pockets, etc. same for all solvents as indicated by <10 % RSD variation in slip flow.

Table 6.2: Summary of flow rate enhancement and slip length with respect to pore radius.

Particle size (nm)*	Pore radius (nm)	Flow enhancement**	Slip Length (nm)***
300	39.5 ± 0.2	1.75 ± 0.07	7.4 ± 0.3
500	69.7 ± 0.4	1.37 ± 0.05	6.4 ± 0.3
690	111.8 ± 0.5	1.20 ± 0.10	5.6 ± 0.5
1000	163.4 ± 1.0	1.12 ± 0.06	5.1 ± 0.3
2000	340.4 ± 2.6	1.04 ± 0.03	3.1 ± 0.1

*The particle sizes (diameters) are manufacturer-defined values.

**The standard deviation in the flow enhancement was calculated by equation: $\Delta E = \left(\frac{E_{average}}{100}\right)\sqrt{(\text{RSD in slope}_{\text{slip curve}})^2 + (\text{RSD in slope}_{\text{no-slip curve}})^2}$

***The standard deviation in the slip length was calculated by equation: $\Delta L_s = \left(\frac{L_s}{100}\right)\sqrt{(\text{RSD in } r_{pore})^2 + (\text{RSD in E})^2}$

Both 1-octanol and n-octane have the same length of alkyl chains in their structure. However, 1-octanol showed a lower extent of flow rate enhancement, with varying pore sizes (shown in Figure 6.7) in silica porous beds, in comparison to n-octane. An experimental study [143] of the slip flow behavior of 1-octanol and n-octane performed on a molecularly smooth n-hexadecyltrichlorosilane (hydrophobic) coated surface using colloidal probe AFM technique reported slip length values of ~10 and 25 nm for n-octane and 1-octanol, respectively. Therefore, on a hydrophobic surface, the extent of flow enhancement for n-octane was lower than 1-octanol.

In contrast, on a hydrophilic (e.g., silica in our case) surface, n-octane should experience higher extent of flow enhancement in comparison to 1-octanol. Our study found the expected trend of flow enhancement for these two liquids with a hydrophilic silica surface. We have obtained slip length values of about 18.4 and 7.4 nm for n-octane and 1-octanol, respectively, in silica porous beds having the lowest pore radius (~39.5 nm). A dipole-induced dipole type of interaction between the surface silanol groups of silica particles and non-polar octyl chains is present in the case of both liquids. However, the polar hydroxyl functional group present in 1-octanol can form a hydrogen bond with the surface silanol groups. Due to this additional dipole-dipole (hydrogen bonding) interaction, 1-octanol experiences a lesser extent of flow enhancement in silica porous media than n-octane. Therefore, the slip length differences for these two liquids between our results and that obtained from the colloidal probe AFM study is in reasonably good agreement from both qualitative and quantitative perspectives.

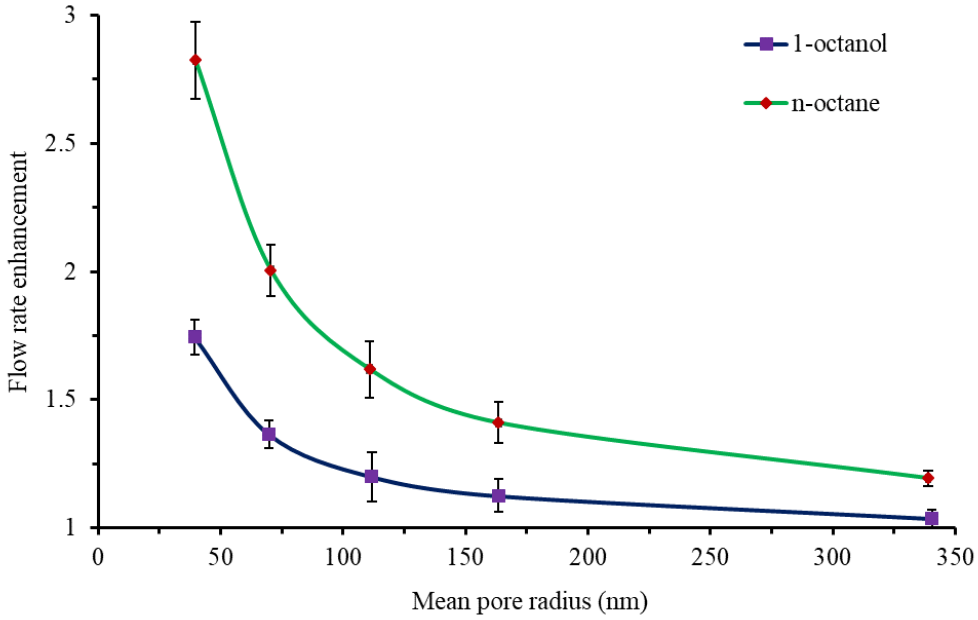

Figure 6.7: Comparison of flow rate enhancement as a function of pore size for 1-octanol and n-octane. The data for n-octane shown here was presented in chapter 5.

In the liquid state of 1-octanol, hydroxyl groups aggregate together to form a spherical polar cluster while the non-polar octyl chains stay in extended form, pointing outwards. Then, the neighbouring clusters interact through the van der Waals forces acting among hydrocarbon chains, giving rise to a high amount of friction [145]. In contrast, n-octane molecules stay linear and interact with each other with only van der Waals forces. Due to having strong intermolecular forces, 1-octanol is more (14 times) viscous than n-octane. The silanol groups present in the silica surface interact with the hydroxyl cluster of self-aggregated 1-octanol molecules slightly through new hydrogen bonding, but not to a great extent [145]. Still, mostly the extended hydrocarbon chains pointing outwards interact with the hydrophilic silica surface, resulting in slip flow, but with a lower flow enhancement than n-octane.

In Figure 6.8, the flow enhancement results obtained experimentally in this thesis (for 1-octanol and n-octane) and from the article of Rogers et al. (for water) [26] were merged into the plot of the dependence of water flow enhancement on pore size for different values (contact angle) of wettability, predicted by Keliu Wu et al. [84, 85], as a function of pore diameter. The published plot [84, 85] was formulated based on the combination of theoretical analysis and experimental and MD simulations data found in the literature. The solid pink and green trendlines represent the flow enhancement of 1-octanol and n-octane, respectively, in a silica porous bed (our study), whereas the solid red trendline represents the flow enhancement of water in C_4H_9-coated porous bed (drawn based on the data available in the literature [26]).

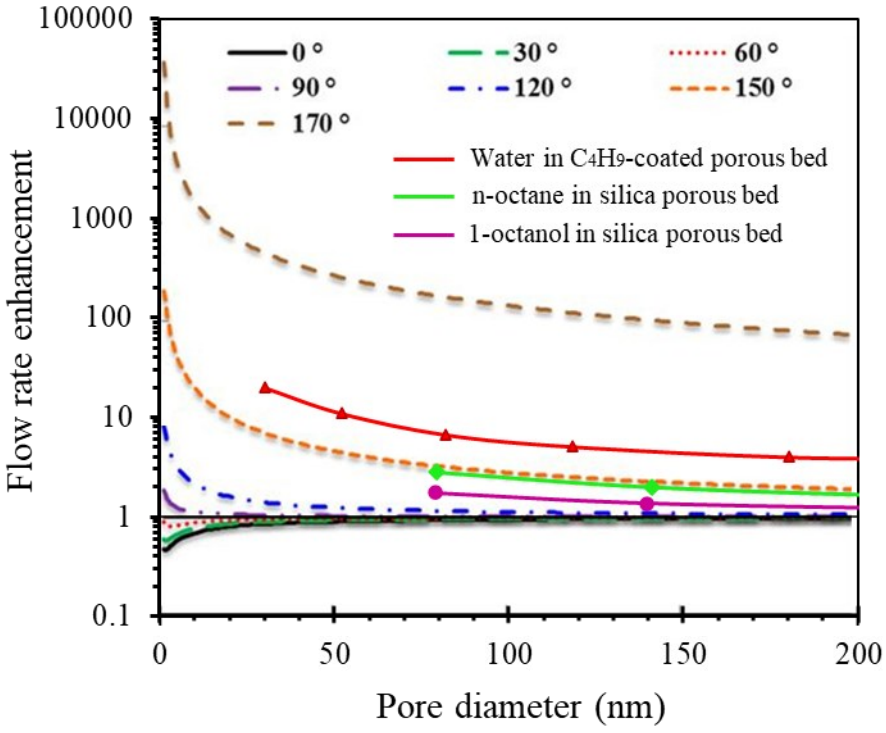

Figure 6.8: Variation of flow rate enhancements with the pore size in different wettability conditions (reprinted from the literature with permission [85]). The solid pink and green

trendlines represent the flow enhancement results for 1-octanol and n-octane, respectively, obtained from this study, and the red trendline represents the flow enhancement results for water obtained from the literature article published by Rogers et al. [26], within 0-200 nm pore diameter range.

Here we are assuming (as the experimentally measured data is unavailable) that the contact angle of 1-octanol on a silica surface is between 60 to 90° since 1-octanol has both polar hydroxyl (wetting) and non-polar octyl (non-wetting) groups. Moreover, we do not have a measured contact angle value for n-octane on a porous silica surface. However, based on the hydrophobic character of n-octane on a silica surface, we are assuming the contact angle, in this case, is between 90 to 120°, while water on the C_4H_9-coated surface had an angle of 83° [26]. The graphical comparison (Figure 6.8) shows that the flow enhancement trendline for 1-octanol (obtained from our study) lies in between the predictions made for 120 to 150° contact angle (hydrophobic) liquids. Higher flow enhancements compared to the theoretical predictions were also observed in case of n-octane flow in silica porous bed (our study) and water flow in C_4H_9-coated porous bed (Rogers et al. [26]). The overall scenario suggests that the theory is predicting a lower extent of slip flow than the experimental results, even for more interacting fluid-solid combinations (1-octanol to silica).

6.4. Conclusion

The extent of slip flow for 1-octanol through silica porous media was found more pronounced in the nanoporous media in comparison to microporous media. Slip length increases

with the decreasing pore diameter of the porous media. Though the magnitude of flow enhancement obtained in this study disagrees with the theoretical predictions, there is reasonable agreement with the other experimental result, even though the systems are not identical [143]. The enhancement in flow has major implications in normal phase chromatography, and in underground hydrocarbon transport and extraction.

Chapter 7: Summary and future outlook

7.1. Summary

This research aimed to study the flow behaviour of viscous fluids through micro and nanoporous structures with the fundamental concern of whether the no-slip boundary condition, a macroscale assumption, can correctly describe the micro and nanoscale flow properties for various combinations of fluid-solid surface interaction. To accomplish the above goal, first, we fabricated micro and nanoporous media suitable for studying micro and nano-scale fluid dynamics at different (100-6000 psi) pressure settings. Evaporation-induced colloidal self-assembly of silica particles (300-2000 nm particle diameter) in a humid condition was found as an effective method in forming porous bed structures having a closed packed arrangement of the silica microspheres. The pore diameter of the porous beds ranges from 79 (for 300 nm particles bed) to 681 nm (for 2000 nm particles bed), which thus allowed us to study flow properties in the platform of micro and nanofluidic channels.

To characterize the porous beds and their flow behaviour, we needed to measure the flow rate through the porous beds. Therefore, a new instrumental setup was built and optimized to measure the linear flow velocity accurately. The flow velocities were measured in porous beds with variable pore sizes at different pressure settings using a dual-point, time of flight velocity measurement technique. The results demonstrate that the porosity and permeability of a porous bed follow a power-law relationship, which is consistent with Archie's power-law model. The

porosity values were determined based on the assumption of no-slip boundary condition for water flow in silica porous beds. These porosity results closely matched the independently measured ones by the water evaporation method, i.e., water, a wetting fluid for silica porous-bed, showed no-slip flow.

In contrast to studies of water in silica beds, a pressure-driven flow experiment for n-octane (a non-wetting hydrophobic liquid) through silica micro or nanoporous media confirmed the existence of slip flow. The silica porous bed having the smallest pore radius (39.7 ± 0.5 nm) showed the maximum extent of slip or flow rate enhancement with a slip length of 18.1 ± 1.0 nm. The flow enhancement in the nanoporous bed (packed with 300 nm particles) was 2.37 times higher than that prepared from 2000 nm diameter particles, i.e., slip flow was more pronounced in the nanofluidic porous media than the microporous ones. However, in the presence of an aqueous film on the silica porous bed, the effective permeability for n-octane was lower than its absolute permeability values determined in both slip and no-slip conditions. The Newtonian fluids, irrespective of their wetting property, exhibited a laminar flow pattern with a Reynolds number less than 1, which thus validated the applicability of Darcy's and Kozeny-Carman equations for the porous systems. 1-octanol having wetting (hydroxyl group) and non-wetting (octyl group) parts for the silica surface also showed slip flow in silica porous media. Like n-octane, flow rate enhancement for 1-octanol was more evident in nanoporous beds (39.5 ± 0.2 nm pore radius) with a slip length of 7.4 ± 0.3 nm. However, 1-octanol experienced a lesser flow enhancement than n-octane since 1-octanol forms hydrogen bonds with the surface silanol groups with its polar hydroxyl functional groups. For both n-octane and 1-octanol, the trend of increasing

flow enhancement with respect to decreasing pore size agrees with both theoretical and experimental observations. The magnitude of n-octane flow enhancement in silica based pore systems observed in this study differed with the molecular dynamics and Lattice Boltzmann simulation results. Most experimental results for both n-octane and 1 octanol in the sub-micron pore size range are in disagreement with theoretical predictions, in terms of magnitudes, although the trend with pore size appears consistent between experiment and theory. However, a reasonable agreement with the other experimental result (colloidal probe AFM study) was observed for these two liquids, even though the systems were not identical.

If we look back at the previous studies (shown in Table 1.1) done in nanofluidic channels, most of these flow studies were done experimentally in straight fluidic channels having well structured, smooth surfaces (graphite, CNT, carbon nanopipe), which do not represent the actual porous media structures found in the oil and gas reservoirs. On the other hand, theoretical studies like molecular dynamics and Lattice Boltzmann simulation studies predict flow properties with two-dimensional slit aperture surfaces, which do not represent three-dimensional porous structures. The AFM study explored the slip flow behaviour of normal alkanes and alcohols on smooth hydrophobic surface, which also do not represent a three dimensional porous structure. Rogers et al. evaluated the variation of slip flow enhancement for water in porous hydrophobic structures as a function of pore size and looked into the surface interaction of water with hydrophobic surface. However, in actual oil and gas reservoirs, inorganic materials (e.g., silicates, calcites, etc) are the major constituents, whereas fluids are mainly hydrophobic in character, which is the combination (hydrophobic liquid and hydrophilic surface) that we used in

our study. Moreover, we explored the effect the micro and nanoscale pore sizes on slip flow. Therefore, this research fill a large gap in the literature involved for the flow of organic fluids through hydrophilic nanoporous media. The enhancement in flow rate has major implications in multiple fields of science and technology, e.g., in normal phase chromatography and underground hydrocarbon transport and extraction. In addition, the measurement approach provides high-quality data sets for various conditions of pore size, providing a strong basis set for future refinement of theoretical models of porous media flow.

7.2. Future perspectives

We have studied the micro and nanoporous media flow properties, focusing mainly on oil recovery applications from unconventional (shale) reservoirs, but it involves several variable factors. A typical oil and gas reservoir contains gas, oil and water. So, in addition to one-phase flow, two or three-phase flow often exists during oil production. The size of the pores ranges from micrometre to nanometers. Some porous rock surfaces are rich in polar inorganic materials such as silicates, carbonates, sulphates, sulphides, phosphates, and some others are rich in nonpolar organic materials such as bitumen [22]. Some fluids are hydrophilic or hydrophobic in character as well as less or highly viscous. This research has explored the single-phase flow through silica porous structures having pore diameters from 79 to 681 nm. Still, there is considerable scope available to explore experimentally. Instead of silica, other inorganic and organic materials can be tried as porous bed material. The surface chemistry effect of other viscous fluids having different wettability can be explored as well. As the size of the pore throats in shale varies from 2 to 100 nm, it will be useful to explore flow properties in smaller pore

systems than we have investigated here so far. In the presence of an adsorbed fluid layer on the solid surface, the permeability of other liquids or multiphase fluid systems can be investigated as well. Experimental work done on the areas mentioned above are very limited in the literature, and more data would be very useful to help theorists for the refinement of theoretical predictive models. Therefore, the above gaps in information can be filled to get better insight into oil production from unconventional resources. In addition, it will add more information in fundamental fluid mechanics for nanoscale porous media flow.

References:

1. Bear, J., *Dynamics of fluids in porous media*. 2013: Courier Corporation.
2. Berejnov, V., N. Djilali, and D. Sinton, *Lab-on-chip methodologies for the study of transport in porous media: energy applications.* Lab on a Chip, 2008. **8**(5): p. 689-693.
3. Karanassios, V., *Microfluidics and nanofluidics: Science, fabrication technology (from cleanrooms to 3D printing) and their application to chemical analysis by battery-operated microplasmas-on-chips.* InTech Publishing, 2018. **1**: p. 1-34.
4. Kirby, B.J., *Micro-and nanoscale fluid mechanics: transport in microfluidic devices*. 2010: Cambridge university press.
5. Eijkel, J., et al. *Nanofluidics: Fundamentals and applications*. in *TRANSDUCERS 2009-2009 International Solid-State Sensors, Actuators and Microsystems Conference*. 2009. IEEE.
6. Liu, C. and Z. Li, *On the validity of the Navier-Stokes equations for nanoscale liquid flows: The role of channel size.* AIP advances, 2011. **1**(3): p. 032108.
7. Chen, Y.-R., *Chapter 2: Advances in LC separations for proteomics*. Advanced LC-MS applications for proteomics, ed. S.R. Pennington. 2016: Bioanalysis Zone. [https://www.bioanalysis-zone.com/chapter-2-advances-in-lc-separations-for-proteomics/]
8. Harris, D.C., *Quantitative chemical analysis. New York*. 2010, WH Freeman and Company.
9. Mazzeo, J.R., et al., *Advancing LC performance with smaller particles and higher pressure.* Anal. Chem, 2005. **77**(23): p. 460 A-467 A.

10. Kennedy, R.T. and J.W. Jorgenson, *Preparation and evaluation of packed capillary liquid chromatography columns with inner diameters from 20 to 50 micrometers.* Analytical chemistry, 1989. **61**(10): p. 1128-1135.

11. Siouffi, A.-M., *About the C term in the van Deemter's equation of plate height in monoliths.* Journal of Chromatography A, 2006. **1126**(1-2): p. 86-94.

12. Swartz, M.E., *UPLC™: an introduction and review.* Journal of Liquid Chromatography & Related Technologies, 2005. **28**(7-8): p. 1253-1263.

13. Nováková, L., L. Matysová, and P. Solich, *Advantages of application of UPLC in pharmaceutical analysis.* Talanta, 2006. **68**(3): p. 908-918.

14. Rogers, B.J., B. Wei, and M.J. Wirth, *Ultra high efficiency protein separations with submicrometer silica using slip flow.* LC GC North America, 2012. **30**(10): p. 890.

15. Wu, Z., et al., *Efficient separations of intact proteins using slip-flow with nano-liquid chromatography–mass spectrometry.* Analytical chemistry, 2014. **86**(3): p. 1592-1598.

16. Todd, D.K. and L.W. Mays, *Groundwater hydrology*. 2004: John Wiley & Sons.

17. Lei, Y., et al., *Nanofluidic diode in a suspended nanoparticle crystal.* Applied Physics Letters, 2010. **96**(26): p. 263102.

18. Meng, D.D. and J.S. Allen, *Micro-and nanofluidics for energy conversion.* IEEE Nanotechnology Magazine, 2008. **2**(4): p. 19-23.

19. Lee, J.W. and E. Kjeang, *Nanofluidic fuel cell.* Journal of power sources, 2013. **242**: p. 472-477.

20. Wang, S., F. Javadpour, and Q. Feng, *Molecular dynamics simulations of oil transport through inorganic nanopores in shale.* Fuel, 2016. **171**: p. 74-86.

21. Salama, A., et al., *Flow and transport in tight and shale formations: a review.* Geofluids, 2017. **2017**.

22. Goral, J., et al., *Pore system characterization of organic-rich shales using nanoscale-resolution 3D imaging.* Fuel, 2019. **258**: p. 116049.

23. Tunio, S.Q., et al., *Comparison of different enhanced oil recovery techniques for better oil productivity.* International Journal of Applied Science and Technology, 2011. **1**(5).

24. Anbari, A., et al., *Microfluidic model porous media: fabrication and applications.* Small, 2018. **14**(18): p. 1703575.

25. Cheng, J.-T. and N. Giordano, *Fluid flow through nanometer-scale channels.* Physical review E, 2002. **65**(3): p. 031206.

26. Rogers, B.J. and M.J. Wirth, *Slip flow through colloidal crystals of varying particle diameter.* ACS nano, 2013. **7**(1): p. 725-731.

27. Zhong, J., et al., *Exploring anomalous fluid behavior at the nanoscale: Direct visualization and quantification via nanofluidic devices.* Accounts of chemical research, 2020. **53**(2): p. 347-357.

28. Majumder, M., et al., *Enhanced flow in carbon nanotubes.* Nature, 2005. **438**(7064): p. 44-44.

29. Vinogradova, O.I., *Slippage of water over hydrophobic surfaces.* International journal of mineral processing, 1999. **56**(1-4): p. 31-60.

30. Lauga, E., M. Brenner, and H. Stone, *Microfluidics: The no-slip boundary condition*, in *Springer Handbooks*. 2007, Springer. p. 1219-1240.

31. Herschy, R.W. and R.W. Fairbridge, *Encyclopedia of hydrology and water resources*. 1998: Springer Science & Business Media.

32. Whitby, M., et al., *Enhanced fluid flow through nanoscale carbon pipes.* Nano letters, 2008. **8**(9): p. 2632-2637.

33. Falk, K., et al., *Ultralow liquid/solid friction in carbon nanotubes: Comprehensive theory for alcohols, alkanes, OMCTS, and water.* Langmuir, 2012. **28**(40): p. 14261-14272.

34. Wang, S., F. Javadpour, and Q. Feng, *Fast mass transport of oil and supercritical carbon dioxide through organic nanopores in shale.* Fuel, 2016. **181**: p. 741-758.

35. McLean, D., *Understanding aerodynamics: arguing from the real physics*. 2012: John Wiley & Sons.

36. Houghton, E.L. and P.W. Carpenter, *Aerodynamics for engineering students*. 2003: Elsevier.

37. Hayes, R., A. Afacan, and B. Boulanger, *An equation of motion for an incompressible Newtonian fluid in a packed bed.* Transport in porous media, 1995. **18**(2): p. 185-198.

38. Constantin, P. and C. Foias, *Navier-stokes equations*. 1988: University of Chicago Press.

39. Sheng, W., *A revisit of Navier–Stokes equation.* European Journal of Mechanics-B/Fluids, 2020. **80**: p. 60-71.

40. Nauenberg, M., *A paradox with the Hagen-Poiseuille relation for viscous fluid flow.* American Journal of Physics, 2014. **82**(1): p. 82-85.

41. Skrdla, P.J., *Modelling sub-micron particle slip flow in liquid chromatography.* Talanta, 2020. **208**: p. 120400.

42. Loudon, C. and K. McCulloh, *Application of the Hagen—Poiseuille equation to fluid feeding through short tubes.* Annals of the Entomological Society of America, 1999. **92**(1): p. 153-158.

43. Scherer, G.W., *Measurement of permeability I. Theory.* Journal of non-crystalline solids, 1989. **113**(2-3): p. 107-118.

44. Neuman, S.P., *Theoretical derivation of Darcy's law.* Acta mechanica, 1977. **25**(3): p. 153-170.

45. Srisutthiyakorn, N. and G.M. Mavko, *What is the role of tortuosity in the Kozeny-Carman equation?* Interpretation, 2017. **5**(1): p. SB57-SB67.

46. Kemblowski, Z. and M. Michniewicz, *A new look at the laminar flow of power law fluids through granular beds.* Rheologica Acta, 1979. **18**(6): p. 730-739.

47. Costa, A., *Permeability-porosity relationship: A reexamination of the Kozeny-Carman equation based on a fractal pore-space geometry assumption.* Geophysical research letters, 2006. **33**(2).

48. Tien, C. and B.V. Ramarao, *Can filter cake porosity be estimated based on the Kozeny–Carman equation?* Powder technology, 2013. **237**: p. 233-240.

49. Jorgensen, S.E. and B.D. Fath, *Encyclopedia of ecology*. 2014: Newnes.

50. Weber, K. and M. Osborn, *The reliability of molecular weight determinations by dodecyl sulfate-polyacrylamide gel electrophoresis.* Journal of Biological Chemistry, 1969. **244**(16): p. 4406-4412.

51. Rodbard, D. and A. Chrambach, *Estimation of molecular radius, free mobility, and valence using polyacrylamide gel electrophoresis.* Analytical biochemistry, 1971. **40**(1): p. 95-134.

52. Plieva, F., et al., *Macroporous elastic polyacrylamide gels prepared at subzero temperatures: control of porous structure.* Journal of Materials Chemistry, 2006. **16**(41): p. 4065-4073.

53. He, M., et al., *Confinement effects on the morphology of photopatterned porous polymer monoliths for capillary and microchip electrophoresis of proteins.* Electrophoresis, 2008. **29**(14): p. 2980-2986.

54. He, M., et al., *Parameters governing reproducibility of flow properties of porous monoliths photopatterned within microfluidic channels.* Electrophoresis, 2010. **31**(14): p. 2422-2428.

55. Holt, J.K., et al., *Fast mass transport through sub-2-nanometer carbon nanotubes.* Science, 2006. **312**(5776): p. 1034-1037.

56. Whitby, M. and N. Quirke, *Fluid flow in carbon nanotubes and nanopipes.* Nature Nanotechnology, 2007. **2**(2): p. 87-94.

57. Hasham, A.A., et al., *Visualization of fracturing fluid dynamics in a nanofluidic chip.* Journal of Petroleum Science and Engineering, 2018. **165**: p. 181-186.

58. Song, W., et al., *Chip-off-the-old-rock: the study of reservoir-relevant geological processes with real-rock micromodels.* Lab on a Chip, 2014. **14**(22): p. 4382-4390.

59. Nguyen, P., H. Fadaei, and D. Sinton, *Pore-scale assessment of nanoparticle-stabilized CO2 foam for enhanced oil recovery.* Energy & Fuels, 2014. **28**(10): p. 6221-6227.

60. Syed, A.H., et al., *A combined method for pore-scale optical and thermal characterization of SAGD.* Journal of Petroleum Science and Engineering, 2016. **146**: p. 866-873.

61. Harrison, A., et al., *Changes in mineral reactivity driven by pore fluid mobility in partially wetted porous media.* Chemical Geology, 2017. **463**: p. 1-11.

62. Datta, S.S., et al., *Spatial fluctuations of fluid velocities in flow through a three-dimensional porous medium.* Physical review letters, 2013. **111**(6): p. 064501.

63. Zeng, Y. and D.J. Harrison, *Self-assembled colloidal arrays as three-dimensional nanofluidic sieves for separation of biomolecules on microchips.* Analytical chemistry, 2007. **79**(6): p. 2289-2295.

64. Azim, M., et al., *Evaluation of protein separation mechanism and pore size distribution in colloidal self-assembled nanoparticle sieves for on-chip protein sizing.* Electrophoresis, 2017. **38**(2): p. 342-349.

65. Shaabani, N., A.B. Jemere, and D.J. Harrison, *Size-based proteins separation using polymer-entrapped colloidal self-assembled nanoparticles on-chip.* Electrophoresis, 2016. **37**(20): p. 2602-2609.

66. Carroll, N.J., et al., *Measurement of flow velocity and inference of liquid viscosity in a microfluidic channel by fluorescence photobleaching.* Langmuir, 2014. **30**(16): p. 4868-4874.

67. Voigt, A., et al., *Laser doppler field sensor for two dimensional flow measurements in three velocity components*, in *Imaging Measurement Methods for Flow Analysis*. 2009, Springer. p. 21-30.

68. Lindken, R., et al., *Micro-particle image velocimetry (μPIV): recent developments, applications, and guidelines.* Lab on a Chip, 2009. **9**(17): p. 2551-2567.

69. Van Dinther, A., et al., *Suspension flow in microfluidic devices—A review of experimental techniques focussing on concentration and velocity gradients.* Advances in colloid and interface science, 2012. **173**: p. 23-34.

70. Meinhart, C.D., S.T. Wereley, and J.G. Santiago, *PIV measurements of a microchannel flow.* Experiments in fluids, 1999. **27**(5): p. 414-419.

71. Bao, J.B. and D. Jed Harrison, *Measurement of flow in microfluidic networks with micrometer-sized flow restrictors.* AIChE journal, 2006. **52**(1): p. 75-85.

72. Gregor Ocvirk, T.T.a.D.J.H., *Optimization of confocal epifluorescence microscopy for microchip-based miniaturized total analysis systems.* Analyst, 1998. **123**(7): p. 1429-1434.

73. Neckers, D.C. and O.M. Valdes-Aguilera, *Photochemistry of the Xanthine Dyes.* Advances in photochemistry, 1993. **18**: p. 315-394.

74. Lindquist, L., *A flash photolysis study of fluorescein*. 1960.

75. Kasche, V. and L. Lindqvist, *Reactions between the triplet state of fluorescein and oxygen1.* The Journal of Physical Chemistry, 1964. **68**(4): p. 817-823.

76. Gevantman, L., *Solubility of selected gases in water.* Nitric oxide (NO), 2000. **308**(3.348): p. 10-4.

77. Liñán, A., et al., *Taylor-diffusion-controlled combustion in ducts.* Combustion Theory and Modelling, 2020. **24**(6): p. 1054-1069.

78. Aris, R., *On the dispersion of a solute in a fluid flowing through a tube.* Proceedings of the Royal Society of London. Series A. Mathematical and Physical Sciences, 1956. **235**(1200): p. 67-77.

79. Casalini, T., et al., *Diffusion and aggregation of sodium fluorescein in aqueous solutions.* The Journal of Physical Chemistry B, 2011. **115**(44): p. 12896-12904.

80. Petrášek, Z. and P. Schwille, *Precise measurement of diffusion coefficients using scanning fluorescence correlation spectroscopy.* Biophysical journal, 2008. **94**(4): p. 1437-1448.

81. Crank, J., *The mathematics of diffusion*. 1979: Oxford university press.

82. Wei, B., B.J. Rogers, and M.J. Wirth, *Slip flow in colloidal crystals for ultraefficient chromatography.* Journal of the American Chemical Society, 2012. **134**(26): p. 10780-10782.

83. Abbas, M.N., *Modeling of porosity equation for water flow through packed bed of monosize spherical packing.* Journal of engineering and development, 2011. **15**(4): p. 205-226.

84. Wu, K., et al., *Wettability effect on nanoconfined water flow.* Proceedings of the National Academy of Sciences, 2017. **114**(13): p. 3358-3363.

85. Wu, K., et al. *A universal model of water flow through nanopores in unconventional reservoirs: relationships between slip, wettability and viscosity*. in *SPE Annual Technical Conference and Exhibition*. 2016. OnePetro.

86. Dufresne, E.R., et al., *Dynamics of fracture in drying suspensions.* Langmuir, 2006. **22**(17): p. 7144-7147.

87. Dufresne, E.R., et al., *Flow and fracture in drying nanoparticle suspensions.* Physical review letters, 2003. **91**(22): p. 224501.

88. Wong, S., V. Kitaev, and G.A. Ozin, *Colloidal crystal films: Advances in universality and perfection.* Journal of the American Chemical Society, 2003. **125**(50): p. 15589-15598.

89. Azim, M.A., *Protein Separation with Self-Assembled Nanoparticle Beds: Mechanism and Separation Performance*, in *Chemistry*. 2016, University of Alberta.

90. Gensterblum, Y., et al., *Gas transport and storage capacity in shale gas reservoirs–A review. Part A: Transport processes.* Journal of Unconventional Oil and Gas Resources, 2015. **12**: p. 87-122.

91. Archie, G.E., *Introduction to petrophysics of reservoir rocks.* AAPG bulletin, 1950. **34**(5): p. 943-961.

92. Siddiqui, A.A., D. Ilk, and T.A. Blasingame. *Towards a characteristic equation for permeability*. in *SPE Eastern Regional/AAPG Eastern Section Joint Meeting*. 2008. OnePetro.

93. Berg, R.R., *Method for determining permeability from reservoir rock properties.* 1970.

94. Siddiqui, A.A., *Towards a characteristic equation for permeability*. 2008, Texas A&M University.

95. Nguyen, D.T.T., et al., *Fast analysis in liquid chromatography using small particle size and high pressure.* Journal of separation science, 2006. **29**(12): p. 1836-1848.

96. Abbott, S.R., *Practical aspects of normal-phase chromatography.* Journal of chromatographic science, 1980. **18**(10): p. 540-550.

97. Diekmann, S., et al., *Revisiting the liquid–liquid phase behavior of n-alkanes and ethanol.* The Journal of Physical Chemistry B, 2019. **124**(1): p. 156-172.

98. Mužíková, Z., M. Pospíšil, and G. Šebor, *Volatility and phase stability of petrol blends with ethanol.* Fuel, 2009. **88**(8): p. 1351-1356.

99. Asay, D.B. and S.H. Kim, *Evolution of the adsorbed water layer structure on silicon oxide at room temperature.* The Journal of Physical Chemistry B, 2005. **109**(35): p. 16760-16763.

100. Umezawa, R., M. Katsura, and S. Nakashima, *Electrical conductivity at surfaces of silica nanoparticles with adsorbed water at various relative humidities.* e-Journal of Surface Science and Nanotechnology, 2018. **16**: p. 376-381.

101. Kern, D.Q. and D.Q. Kern, *Process heat transfer*. Vol. 5. 1950: McGraw-Hill New York.

102. Richardson, J.F., J.H. Harker, and J.R. Backhurst, *Coulson and Richardson's chemical engineering: Particle technology and separation processes*. 2002: Butterworth-Heinemann.

103. Kruczek, B., *Carman–kozeny equation*. 2014, Berlin, Germany: Springer. p. 11-17.

104. Álvarez-Quintana, S., et al., *Water viscosity in confined nanoporous media and flow through nanofiltration membranes.* Microporous and Mesoporous Materials, 2020. **303**: p. 110289.

105. Middleman, S., *An introduction to fluid dynamics.* 1998.

106. Cabooter, D., et al., *Detailed characterisation of the flow resistance of commercial sub-2 μm reversed-phase columns.* Journal of Chromatography A, 2008. **1178**(1-2): p. 108-117.

107. Kundu, P., V. Kumar, and I.M. Mishra, *Experimental and numerical investigation of fluid flow hydrodynamics in porous media: Characterization of pre-Darcy, Darcy and non-Darcy flow regimes.* Powder Technology, 2016. **303**: p. 278-291.

108. Ho, T.A. and Y. Wang, *Enhancement of oil flow in shale nanopores by manipulating friction and viscosity.* Physical Chemistry Chemical Physics, 2019. **21**(24): p. 12777-12786.

109. Hitzer, E., *Early works on the Hagen-Poiseuille flow.* Memoirs-faculty of Engineering Fukui University, 2001. **49**(1): p. 45-54.

110. Mallin, D.J., *Measurements of water flow rate and slip length in single nanopipes*. 2016: University of California, Irvine.

111. Lee, K.P., H. Leese, and D. Mattia, *Water flow enhancement in hydrophilic nanochannels.* Nanoscale, 2012. **4**(8): p. 2621-2627.

112. Gudmundsson, S., *General aviation aircraft design: Applied Methods and Procedures*. 2013: Butterworth-Heinemann.

113. Morrison, F.A., *An introduction to fluid mechanics*. 2013: Cambridge University Press.

114. Shamey, R. and X. Zhao, *Modelling, simulation and control of the dyeing process*. 2014: Elsevier.

115. Quinn, H.M., *A reconciliation of packed column permeability data: Column permeability as a function of particle porosity.* Journal of Materials, 2014. **2014**: p. 1-22.

116. Zeng, Z. and R. Grigg, *A criterion for non-Darcy flow in porous media.* Transport in porous media, 2006. **63**(1): p. 57-69.

117. Hellström, G. and S. Lundström. *Flow through porous media at moderate Reynolds number*. in *International Scientific Colloquium Modelling for Material Processing: 08/06/2006-09/06/2006*. 2006.

118. Tek, M., *Development of a generalized Darcy equation.* Journal of Petroleum Technology, 1957. **9**(06): p. 45-47.

119. Bear, J. and C. Braester, *On the flow of two immscible fluids in fractured porous media*, in *Developments in Soil Science*. 1972, Elsevier. p. 177-202.

120. Iler, R.K., *The surface chemistry of silica.* The chemistry of silica, 1979.

121. Sonnefeld, J., M. Löbbus, and W. Vogelsberger, *Determination of electric double layer parameters for spherical silica particles under application of the triple layer model using surface charge density data and results of electrokinetic sonic amplitude measurements.* Colloids and Surfaces A: Physicochemical and Engineering Aspects, 2001. **195**(1-3): p. 215-225.

122. Duval, Y., et al., *Evidence of the existence of three types of species at the quartz− aqueous solution interface at pH 0− 10: XPS surface group quantification and surface complexation modeling.* The Journal of Physical Chemistry B, 2002. **106**(11): p. 2937-2945.

123. Leroy, P., et al., *Influence of surface conductivity on the apparent zeta potential of amorphous silica nanoparticles.* Journal of colloid and interface science, 2013. **410**: p. 81-93.

124. Sverjensky, D.A., *Prediction of surface charge on oxides in salt solutions: Revisions for 1: 1 (M+ L−) electrolytes.* Geochimica et Cosmochimica Acta, 2005. **69**(2): p. 225-257.

125. Sögaard, C., J. Funehag, and Z. Abbas, *Silica sol as grouting material: a physio-chemical analysis.* Nano convergence, 2018. **5**(1): p. 1-15.

126. Glover, P.W., *Petrophysics.* University of Aberdeen, UK, 2000.

127. Honarpour, M. and S. Mahmood, *Relative-permeability measurements: An overview.* Journal of petroleum technology, 1988. **40**(08): p. 963-966.

128. Choi, C.-H., K.J.A. Westin, and K.S. Breuer, *Apparent slip flows in hydrophilic and hydrophobic microchannels.* Physics of fluids, 2003. **15**(10): p. 2897-2902.

129. Islam, M.M. and D.J. Harrison, *Slip and No-Slip Flow in Micro-and Nano-Porous Media.* Bulletin of the American Physical Society, 2018. **63**.

130. Sui, H., et al., *Molecular simulations of oil adsorption and transport behavior in inorganic shale.* Journal of Molecular Liquids, 2020. **305**: p. 112745.

131. Korson, L., W. Drost-Hansen, and F.J. Millero, *Viscosity of water at various temperatures.* The Journal of Physical Chemistry, 1969. **73**(1): p. 34-39.

132. Thompson, J.W., T.J. Kaiser, and J.W. Jorgenson, *Viscosity measurements of methanol–water and acetonitrile–water mixtures at pressures up to 3500 bar using a novel capillary time-of-flight viscometer.* Journal of Chromatography A, 2006. **1134**(1-2): p. 201-209.

133. Pietak, A., et al., *Atomic force microscopy characterization of the surface wettability of natural fibres.* Applied surface science, 2007. **253**(7): p. 3627-3635.

134. Dymond, J. and H. O/ye, *Viscosity of selected liquid n-alkanes.* Journal of physical and chemical reference data, 1994. **23**(1): p. 41-53.

135. Andrade, E.d.C., *The viscosity of liquids.* Nature, 1930. **125**(3148): p. 309-310.

136. Klein, T., et al., *Liquid viscosity and surface tension of n-hexane, n-octane, n-decane, and n-hexadecane up to 573 K by surface light scattering.* Journal of Chemical & Engineering Data, 2019. **64**(9): p. 4116-4131.

137. Li, L., J. Mo, and Z. Li, *Flow and slip transition in nanochannels.* Physical Review E, 2014. **90**(3): p. 033003.

138. Li, L., et al., *A New Slip Length Model for Enhanced Water Flow Coupling Molecular Interaction, Pore Dimension, Wall Roughness, and Temperature.* Advances in Polymer Technology, 2019. **2019**.

139. Zhang, T., et al., *The transport behaviors of oil in nanopores and nanoporous media of shale.* Fuel, 2019. **242**: p. 305-315.

140. Zhao, J., et al., *Lattice Boltzmann simulation of liquid flow in nanoporous media.* International Journal of Heat and Mass Transfer, 2018. **125**: p. 1131-1143.

141. Monger, H.C. and E.F. Kelly, *Silica minerals.* Soil mineralogy with environmental applications, 2002. **7**: p. 611-636.

142. Görlich, E., *The structure of SiO2—Current views.* Ceramics International, 1982. **8**(1): p. 3-16.

143. McBride, S.P. and B.M. Law, *Viscosity-dependent liquid slip at molecularly smooth hydrophobic surfaces.* Physical Review E, 2009. **80**(6): p. 060601.

144. Matsuo, S. and T. Makita, *Viscosities of six 1-alkanols at temperatures in the range 298–348 K and pressures up to 200 MPa.* International journal of thermophysics, 1989. **10**(4): p. 833-843.

145. Franks, N., M. Abraham, and W. Lieb, *Molecular organization of liquid n-octanol: An X-ray diffraction analysis.* Journal of pharmaceutical sciences, 1993. **82**(5): p. 466-470.